MODELLING OF LOW-PRESSURE DISCHARGES FOR PLASMA PROCESSING

A Thesis for the Degree of

PHILOSOPHIAE DOCTOR

Presented to

Dublin City University

By

Zhenning Su, B.Eng
School of Physical Sciences,
Dublin City University

Research Supervisor

Prof. Miles M. Turner

June 2015

Declaration

I hereby certify that this material, which I now submit for assessment on the programme of study leading to the award of PhD is entirely my own work, and that I have exercised reasonable care to ensure that the work is original, and does not to the best of my knowledge breach any law of copyright, and has not been taken from the work of others save and to the extent that such work has been cited and acknowledged within the text of my work.

Signed: ______________________________
Zhenning Su, ID No.: 55130208
08 May 2015

Acknowledgements

I would like to thank Prof. Miles Turner and Dr. Stephen Daniels for leading me into this field. Without their trust and support, this work could never be done. I would like to thank all my colleagues who helped me when I needed them; it's always a pleasure to work with you guys. I would also like to thank my family for their support, especially my wife Wei Song and our parents, thank them for accompanying and supporting me in the long journey of life.

I would like to thank the examiners of this thesis, Prof. Vasco Guerra and Dr. Stephen Daniels, for their comments and suggestions in, and the time they spent on preparing for, the viva exam. I would like to give special thanks to Prof. Vasco Guerra, for coming all the way from Lisbon, Portugal to Dublin for my viva.

I would like to thank SFI for funding my work; this work is funded by Science Foundation Ireland under grant No. 08/SRC/I1411.

Table of Contents

List of Figures

List of Tables

List of Symbols

In this work, a bold letter represents a vector. For example, **B** is the vector of a magnetic field, and B is the scalar of **B**.

Symbols

< >	average operator, <A> means take the average of A
[A]	density of A
*	an empty surface site
α	the electronegativity; or the factor proportional to the gradient in $B(z)$ near the resonance zone
α_0	$\alpha_0 = n_0^-/n_{e,0}$: the electronegativity at the centre of the plasma
β	equals to $1/k_B T$
Γ	the adsorbate's flux at the surface
γ	$\gamma = T_e / T_i$
γ_A	the sticking coefficient of neutral species A in a surface reaction
ε	electron energy
$\varepsilon_{e,w}$	$\varepsilon_{e,w} = 2e\mathrm{T}_e$, the mean kinetic energy loss per electron due to electron lost to the wall
$\varepsilon_{\mathrm{loss},j}$	the electron energy loss due to collision j
ε_w	the energy loss due to an electron-ion pair lost to the wall
θ	an adsorbate's surface coverage
θ_*	the fraction of free surface sites
$\theta_\#$	surface coverage of the immobilized transition state particles
θ_s	the empty to total surface adsorption sites ratio
ξ	the fractional uncertainty of a certain reaction's cross section measurement
Λ	thermal wavelength
Λ_n	the effective diffusion length of neutral species
λ_i	the ion-neutral mean free path

λ_{n}	the neutral-neutral mean free path
μ	chemical potential; or the reduced mass
σ	cross section; or symmetry factor for rotational partition function
$\sigma_{\mathrm{i},\,j}$	ion-neutral scattering cross section of the jth neutral gas species
$\sigma_{\mathrm{n},\,j}$	neutral-neutral scattering cross section of the jth neutral gas species
τ	a particle's average time of stay in the vicinity of a surface
τ_{res}	the residence time for neutral species
Φ	plasma sheath potential
ϕ	angular velocity
ω	microwave frequency of an ECR plasma
ω_{ce}	electron gyration frequency in an ECR plasma
A	$A = A_{\mathrm{R}} + A_{\mathrm{L}}$, the total cylindrical plasma chamber surface area
A_{eff}	$A_{\mathrm{eff}} = A_{\mathrm{R}}h_{\mathrm{R}} + A_{\mathrm{L}}h_{\mathrm{L}}$, the effective area for particle loss
A_{L}	$A_{\mathrm{L}} = 2\pi R^2$, the area of the two circular faces of a cylindrical plasma chamber whose distance defines L
A_{R}	$A_{\mathrm{R}} = 2\pi RL$, the area of a cylindrical plasma chamber facing the radial direction
a^2	the area of each unit cell that contains one surface site
B	magnetic flux density
$\mathbf{B}_0$	time-independent uniform magnetic filed
D_{A}	the neutral diffusion coefficient of neutral species A
d_{eff}	$d_{\mathrm{eff}} = V/A_{\mathrm{eff}}$ is the effective plasma size for particle loss
E	the energy density of electrons
E_a or ΔE	activation energy
E_{r} and E_{l}	the amplitudes of the RHP and LHP components of the linearly polarized microwave
$E_x(\mathbf{r})$	electric field of the linearly polarized microwave with x polarization
e	the electron charge (1.602×10^{-19} C)
F_{A}	the input rate of the plasma feedstock gas A in particles per second
f_{m}	electron momentum transfer frequency

h_L or h_R	the axial or radial plasma sheath edge to centre density ratio for positive ions
K, $K^{\#}$, $K^{\ddagger}$	the equilibrium constant
k	rate coefficient of a reaction
k_θ	the rate coefficient for the surface coverage change
k_B	the Boltzmann constant, which equals to 1.3807×10^{-23} J/K
$K_\mathrm{i,\,rec}$	positive-negative ion recombination coefficient
$k_{\mathrm{e},j}$	the rate coefficient of the electron impact reaction j
k_s	the rate coefficient of a surface reaction
$k_{\mathrm{s,i},l}$	the rate coefficient of the surface reaction where a positive ion l is lost to the chamber wall
k_TST	rate coefficient derived from the transition state theory
L	the length of the cylindrical plasma reactor chamber (see Figure 2)
l_p	half length of the system, where $l_\mathrm{p} = L/2$
M	the total number of adsorption surface sites
M'	number of free adsorption surface sites
m_+	the mass of a positive ion in kg
m_e or m	mass of an electron in kg, $m_\mathrm{e} = 9.1 \times 10^{-31}$ kg
m_i	the mass of a positive ion in kg; or the density-weighted positive ion mass defined in Eq (23)
m_n or M_n	the mass of a neutral species in kg
$\tilde{N}$	number of duplicated systems in a Canonical ensemble
$N^{\#}$	number of atoms in the precursor transition state
N_0	surface site density
$N_{\mathrm{A}*}$	number of species A's atoms adsorbed on the surface
$N_\mathrm{e,gas}$	the number of all electron ionization, excitation and elastic collisions
N_g	number of gaseous atoms in the system
N_i	number of positive ion species
N_j	total number of neutral gas species
n_+	total positive ion density
n_-	total negative ion density
n_0^-	the total negative ion density at the centre of the plasma

n_A	the density of species A
n_e	electron density
$n_{\mathrm{g},j}$	the density of the jth neutral gas species
$n_{\mathrm{i},0}^{+}$	the total positive ion density at the centre of the plasma
$\tilde{n}_i$	the number of systems of the canonical ensemble having energy E_i
n_j	the density of the neutral species involved in reaction j
P_ads	the input power
P_s	the initial sticking coefficient for surface chemisorptions or the reaction probability for other surface processes
p_A	partial pressure of A
p_i	fraction of molecules in the energy state i
Q	canonical partition function
q	partition function of a single particle
R	the radius of the cylindrical plasma reactor chamber (see Figure 2); or the random fractional factor that describes how much a reported cross section deviates from the accurate value
r	the distance from the point mass μ to the axis of rotation
S_ecr	absorbed power per area or energy flux in an ECR plasma
$S(\theta)$	sticking coefficient
$S_0(T)$	initial sticking coefficient or zero-coverage sticking coefficient
s	an empty surface site
sccm	unit of plasma feedstock gas input rate, 1 sccm = 4.477962×10^{17} (particles/s)
T	gas temperature in kelvin; or the time interval between the electron's initial and final time when it travels near the resonance zone in an ECR plasma
$T_\pm$	positive/negative ion temperature in kelvin
T_e	electron temperature in kelvin
T_e	electron temperature in volts
T_g	gas temperature in kelvin
T_i	ion temperature in kelvin, $T_\mathrm{i} \equiv T_\pm = T_\mathrm{g}$
Δt_res	electron's effective time in the resonance zone in an ECR plasma

U_{th}	ionization or excitation energy threshold in volts
$\bar{u}_{\mathrm{B}}$	the density-weighted average Bohm speed (see Eq. (23))
u_{B}	Bohm speed
V	plasma chamber volume
v	the frequency of the transition from the activated complex to the product; or the pre-exponential factor in Arrhenius equation
$v(\varepsilon)$	the electron speed expressed in ε, $v(\varepsilon) = \sqrt{}(2\varepsilon/m)$
v_{e}	$v_{\mathrm{e}} = (8e\mathrm{T}_{\mathrm{e}}/\pi m_{\mathrm{e}})^{1/2}$ is the mean thermal speed of electrons
v_m	frequency of each vibration mode
v_n	$v_n = (8k_{\mathrm{B}}T_{\mathrm{g}} / \pi m_{\mathrm{n}})^{1/2}$ is the mean thermal speed of a neutral species
v_{r}	the transverse velocity (perpendicular to applied **B** field) of the electron's right-hand gyration, which points from the gyration centre to the electron
v_{res}	the electron speed parallel to the z axis at resonance
W_{ecr}	electron energy gain per pass in an ECR plasma
z'	the distance to the exact resonance in an ECR plasma, $z' = z - z_{\mathrm{res}}$
Δz_{res}	effective resonance zone width in an ECR plasma

Abbreviations

CCP	capacitively coupled plasma
ECR	electron cyclotron resonance
EEDF	electron energy distribution function
ER	Eley-Rideal surface adsorption mechanism
ICP	inductively coupled plasma
LH	Langmuir-Hinshelwood surface adsorption mechanism
LHP	left-hand circularly polarized
PES	potential energy surface
RHP	right-hand circularly polarized
TST	transition state theory
rf	radio frequency

Subscripts or Superscripts

0	at the centre of a plasma; or denote that a quantity is time-independent
(s)	the particle is adsorbed on the surface
#	of the transition state; or of the precursor state for Langmuir-Hinshelwood surface adsorption
‡	of the transition state
*	the particle is adsorbed on the surface
g	of the neutral gas
res	at resonance or near the resonance zone
rdm	random
rot	of a particle's rotational degree of freedom
trans	of a particle's translational degree of freedom
v / vib	of a particle's vibrational degree of freedom

Abstract

Low-pressure high density plasma processes are indispensable today for the microelectronic manufacturing industry. Classic plasma global models have been important tools for studying the properties of low pressure plasmas due to their highly computational efficiency and large chemical reaction capacity. However, the lack of detailed description of surface processes rendered these classic plasma global models incapable of predicting the surface-process-dominated phenomena such as the several times [O] (atomic oxygen density) increase in an SF_6/O_2 plasma compared to a pure O_2 plasma when even small amount of SF_6 is added to the feedstock gas composition (e.g. 5%). It seemed like global modelling in the field of low pressure plasma material processing had reached a dead end. But things were not so hopeless, to combat the challenge global modelling faces, in 2009 Kokkoris *et al* published an SF_6 plasma global model with heterogeneous surface model. However, the details of their surface model and how it was coupled to a plasma global model was not given. In this work, I start from the detailed descriptions of a plasma global model with heterogeneous surface model and then show that my methods for modelling the surface processes of a plasma are viable. The mechanisms are then extended to the development of an SF_6/O_2 plasma model. I will model and give explanations on the mechanisms governing the aforementioned [O] increase in an SF_6/O_2 plasma, which was only reported in experimental works. The work on the fluctuations of a plasma model's outputs due to the statistical variations of the electron-involving reactions' rate coefficients is also discussed in this thesis. The current trend in the microelectronic manufacturing industry is to deploy ECR (electron cyclotron resonance) source plasmas for material processing. To follow this trend, the most crucial step of modelling an ECR discharge, namely the electron heating calculation is also given a detailed discussion in this work.

1 Introduction

Plasma processes have been indispensable to many industries today, such as surgical implant, medical treatment, food packaging, steel, automotive, aerospace, waste management and microelectronic manufacturing, just to name a few of them. The chemically active species of a plasma can effectively alter the surface of a material, thus achieve desired physical-chemical surface properties. In this work, I will concentrate on the modelling of low pressure plasmas, which are extensively used in the microelectronic manufacturing industry. One fact that best shows the importance of the plasma technology to this industry is that among the tens to hundreds fabrication steps for IC (integrated circuit) manufacturing, one-third of them involve plasma processes [1], p.2.

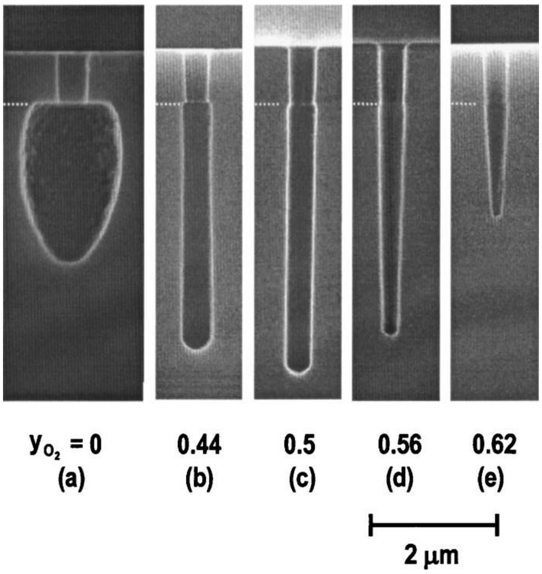

Figure 1 Image of trenches etched on Si by SF_6/O_2 plasma under various O_2 compositions. Except the O_2 percentage composition, all other plasma etching conditions were kept constant. y_{O2} is the O_2 percentage composition in the SF_6/O_2 feedstock gas. (from Ref. [2])

Among the many plasma processes in IC manufacturing, the most crucial are metal deposition, film growth, dopant implant, photoresist or other polymer films removal and etching. In modern IC manufacturing, the similar processes (deposit or grow, dope or modify, etch or remove) have to be repeated again and again [1], p.2. The last application, plasma etching, has been one of the deciding factors to the feature size of the ICs. Due to the highly directional nature of the energetic etchant ions near a substrate surface (such as a silicon wafer), the plasma process can achieve desired anisotropic etching result. The vertical trenches, which are the core structures for transistor isolation in an IC, produced in the plasma etching process are good examples (Figure 1). However, strictly vertical etches are not always desired, some side wall angles are needed in many applications. Plasma processing is the only commercial way to control the side wall angles [1], p.3 (see Figure 1).

Plasma global models are important tools for plasma study due to their irreplaceable temporal efficiency and ability to describe complex chemical kinetics. However, two problems arise when modelling plasmas of a fluorine containing gas and oxygen mixtures with these "classic" plasma global models: (1) these models are not capable of describing surface-process-dominated scenarios, such as the several times increase in [O] (atomic oxygen density) when small SF_6 (e.g. 5% in the feed composition) is added to a pure O_2 plasma's feedstock gas [3], which makes these models much less attractive when study this kind of plasmas. (2) Although all existing explanations have pinpointed the surface processes for such a large increase in [O], to my best knowledge there haven't been any papers that have ever given detailed explanations on the mechanisms (more precisely, the chemical kinetics) that govern the above mentioned scenario. It seemed like global modelling in the field of low pressure plasma materials processing had reached a dead end. But things were not so hopeless, in 2009 Kokkoris *et al.* published an SF_6 plasma global model with heterogeneous (i.e., Eley-Rideal mechanisms) surface model [4]. They showed that the rate coefficient of a surface reaction k_s can be calculated from the adsorbate's surface coverage θ, therefore a sophisticated surface reaction set that describes the detailed surface kinetics can be coupled to a classic SF_6 plasma global model. The challenge was that the details of the heterogeneous surface model and the method of coupling their surface model to a classic plasma global model were not given in their paper. Chapter 2 through chapter 4 of this work shows my efforts in seeking a way to modelling the heterogeneous surface processes, which confronts the first challenge. Chapter 2 gives detailed descriptions on the plasma global model with heterogeneous surface model developed in this work. The assumptions about solid surfaces for theoretical treatment are given in chapter 3. And finally, the calculation of the surface reaction rate coefficients in the transition state theory (TST) is also described in chapter 3. The statistical thermodynamics concept of partition functions, which directly leads to the reaction rate coefficient calculations in TST is given in Appendix A. An introduction to the TST and the calculation of a general reaction rate coefficient in the TST are given in Appendix B. Chapter 4 gives my proposed chemical kinetics of the SF_6/O_2 plasma in an Al chamber.

The aforementioned limitations on classic plasma global models have significantly limited their applications, and posed a serious challenge to plasma modelling. In accepting this challenge, I had developed an SF_6 plasma global model with heterogeneous surface model for Al surfaces (a commonly used material in plasma processing chambers), and the methods were then expanded to an O_2 plasma model and later to an SF_6/O_2 plasma model which is capable of simulating the above mentioned large [O] increase. Chapter 5 of this work is devoted to the study of the density variations of the two most important species in an SF_6/O_2 plasma: atomic O and atomic F by using the model. In chapter 5, I will reveal the mechanisms governing the [O] increase scenario. I will also validate the model with two experimental works. Most of the contents of chapter 5 are from a paper we are going to publish [5].

A source of plasma model inaccuracy could stem from the cross section data uncertainties in their measurements, which in turn cause fluctuations of the reaction rate coefficients in plasma models. To our best knowledge, the fluctuations of plasma models' outputs due to these variations haven't been well studied. Chapter 6 of this work shows these fluctuations by using my SF_6 plasma global model with heterogeneous surface model.

Plasma processing is normally carried out in various types of low pressure high density plasma source chambers. The rf (radio frequency) plasma sources, either CCP (capacitively coupled plasma) or ICP (inductively coupled plasma) chambers, have been used and studied for many years. However, one crucial problem of the rf source plasmas is that the ion-bombarding flux and the ion-bombarding energy can not be controlled independently [1], p.17. For practically reasonable ion flux, the high sheath voltage can cause damage to the Si wafer, and their relatively low ion density has narrowed their applications. The rf plasma source chambers' problems can be solved by switching to the ECR (electron cyclotron resonance) plasma source chambers. Today, the use of the ECR plasma chambers has been a trend in the microelectronic manufacturing industry. ECR chambers can achieve the desired high ion density and low sheath potential by using the microwave electron heating mechanism. Chapter 7 is devoted to the calculation of ECR electron heating, which is arguably the most important step for modelling an ECR plasma.

2 The SF_6/O_2 Plasma Global Model with Heterogeneous Surface Model

Classic plasma global models are important tools for plasma study due to their irreplaceable temporal efficiency and ability to describe complex gas phase chemical kinetics. However, due to the simple surface-process descriptions implemented in them, these models are not capable of describing surface-process-dominated scenarios, such as the several times increase in atomic oxygen density when small SF_6 (e.g. 5% in the feed composition) is added to a pure O_2 plasma's feedstock gas, which makes these models much less attractive when study plasmas of fluorine containing gas and oxygen mixtures. To my best knowledge, the detailed chemical kinetics of the above mentioned scenario haven't been revealed by any literatures to date. One of the main objectives of this work is to study the density variations of the two most important species in an SF_6/O_2 plasma: atomic O and atomic F, which has been achieved by using an SF_6/O_2 plasma global model with heterogeneous surface model for Al surfaces. The model is capable of simulating the above mentioned large [O] increase, the results are shown in chapter 5. This chapter serves as an introduction to the plasma model developed and used in this work. The model uses the surface coverage balance equation obtained in section 2.2.2.3 to calculate the surface coverage for each of the chemisorbed species, which in turn calculates the surface reaction rate coefficients for the corresponding mass balance equations. The derivation of the equations used to calculate the rate coefficients of the surface coverage balance equations is given in chapter 3. The detailed chemical kinetics for the SF_6/O_2 plasma-Al system are proposed in chapter 4. I will reveal the mechanisms governing the aforementioned large [O] increase and validate the model with two experimental works in chapter 5.

2.1 Introduction

Two plasma processes, namely, Fluorine-based low-pressure high density plasma anisotropic etching of silicon [6] and oxygen-based low-pressure high density plasma etching of polymer photoresist films [3] are indispensable for the microelectronics industry. CF_4/O_2, C_4F_8/O_2 and SF_6/O_2 are commonly used processing gas mixtures. In the silicon etching process, as the main etchant, F atoms react with Si and SiO_2 to form volatile SiF_4 [7]. The role of oxygen in an SF_6/O_2 plasma is to improve the anisotropic etching performance and to prevent fluorine from over-etching the substrate [6]. Carefully adjusting O_2's composition in the SF_6/O_2 plasma's feedstock gas can achieve desired structures on silicon wafers in the etching process [2]. The basic chemical kinetics underlying the above application is that due to the high energy barrier of the reverse reaction of O chemisorption (e.g., 4.63 eV on a β-cristobalite (001) surface [8], 5.9 eV on an Al(111) surface [9]), chemisorbed O can only be removed from the surface by directional ion bombardment [6] or by O surface recombinations [8], thus preventing F from further etching the material.

An intriguing experimental scenario that has been known for decades [3] in an SF_6/O_2 plasma is that a small composition of SF_6 in the SF_6/O_2 plasma's feedstock gas will result in several times increase in [O] (atomic oxygen density) comparing to [O] in a pure O_2 plasma [3], which in turn significantly enhances the etch rate in the polymer photoresist film etching application (where O atoms act as the main etchant) [3]. Because this scenario is surface-process-dominated, the increase in [O] has also been seen in plasmas of other fluorine containing gas and O_2 mixtures (e.g. CF_4/O_2 plasmas [10]). Similarly, a small composition of O_2 in the SF_6/O_2 plasma's feedstock gas will result in an increase in [F] (atomic fluorine density) comparing to [F] in a pure SF_6 plasma (from existing experiments, the increase is in a more gradual fashion compared to the above mentioned sharp increase in [O]) [7], [11]–[13], which in turn gives rise to a maximum etch rate of the etching process at certain O_2 feed composition [11]. Moreover, these scenarios have been seen in different types of plasma discharges (CCP [10], ECR [11], DECR [3], HCRIE reactor [13]). Available works have revealed that these phenomena are governed by surface processes [3], [10], however, to my best knowledge there haven't been any papers that have ever given detailed explanations on the mechanisms and chemical kinetics that govern these scenarios.

For low pressure plasma materials processing, the classic global models [14]–[17] are very useful tools for their highly computational efficiency and large chemical reaction capacity. These models use certain analytical approximations to describe the spatial distribution of the plasma species densities, but explicitly calculate the time evolution of these quantities. This approach is quite accurate at low pressure, comparing to any model that explicitly describes the spatial distributions. However, the lack of detailed description of surface processes makes these classic plasma global models incapable of predicting surface-process-dominated phenomena described above. It seemed like global modelling in the field of low pressure plasma materials processing had reached a dead end. But things were not so hopeless, in 2009 Kokkoris *et al.* published an SF_6 plasma global model with heterogeneous (i.e., Eley-Rideal mechanisms) surface model [4]. They showed that the rate coefficient of a surface reaction k_s can be calculated from the adsorbate's surface coverage θ, therefore a sophisticated surface reaction set that describes the detailed surface kinetics can be coupled to a classic SF_6 plasma global model. The challenge was that the details of the heterogeneous surface model and the method of coupling their surface model to a classic plasma global model were not given in their paper.

In this chapter, I give detailed descriptions of the plasma model used through out this work, i.e., the SF_6/O_2 plasma global model with heterogeneous surface model of an rf (radio frequency) discharge. The model explicitly calculates the adsorbates' surface coverage θ by using a heterogeneous surface model, which in turn calculates the surface reactions' rate coefficients k_s for the mass balance equations. I propose a detailed description of the chemical kinetics and mechanisms that govern the aforementioned scenarios (previously the large increase in [O] as mentioned above only manifested in experiments) in Chapter 4 and section 5.1, and validate the model with two experimental works (Ref. [10] and Ref. [13]) in Chapter 5. Due to the length of the thesis, the pure O_2 plasma global model with heterogeneous surface model of an rf discharge used here is to be described in a follow-up paper [18].

2.2 The Model

2.2.1 Classic Plasma Global Model

There have been many papers of detailed descriptions on classic plasma global models (for example, Refs. [14]–[17]). A classic plasma global model is a so called 0-dimension model due to the fact that it uses volume averaged plasma parameters with spatial variations of the charged species taken into account. The global model for high density noble gases was developed by Lieberman and Gottscho, and was then extended to molecular gases by Lee *et al.* [14]. One of the important features of a plasma global model is its capability of including large number of chemical reactions, thus detailed chemical kinetics can be simulated. Essentially a classic plasma global model has two sets of differential equations: the mass balance equations and the energy balance equations. The model uses these equations to calculate the densities of the species and the temperature of the electrons in the process chamber (Figure 2). As no explicit spatial variations are described in these equations, the model can achieve great computational efficiency.

In this work, I make a common assumption for low pressure plasmas that $T_+ \approx T_- \approx T_g$ = constant ($T_\pm$ is the positive/negative ion temperature in kelvin, T_g is the gas temperature in kelvin). Here, I assume T_g = 600 K as Gudmundsson and Thorsteinsson have proposed [14], which has been indicated by studies on neutral gas heating (e.g. Ref. [19]).

2.2.1.1 Mass Balance Equations

For a second order gas phase reaction such as

$$\mathrm{A} + \mathrm{B} \xrightarrow{k} \mathrm{C} + \mathrm{D}, \tag{1}$$

the **mass balance equation** for species A is [17], [20]:

$$\frac{dn_\mathrm{A}}{dt} = \frac{F_\mathrm{A}}{V} - kn_\mathrm{A}n_\mathrm{B} - \frac{n_\mathrm{A}}{\tau_\mathrm{res}}, \tag{2}$$

where n_A, n_B are the densities of species A and B; k is the rate coefficient of the reaction; τ_res is the **residence time** for neutral species, which simulates the throttle position of the plasma chamber's exhaust pump, thus controls the gas pressure in the chamber; F_A is the input rate of the plasma feedstock gas A in particles per second; V is the chamber volume.

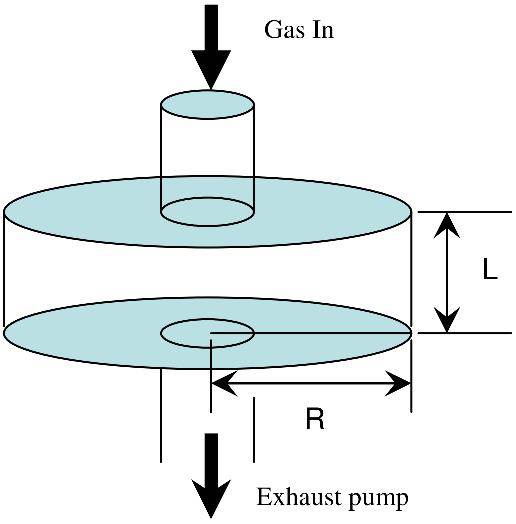

Figure 2 The cylindrical plasma chamber simulated by the model.

For a surface reaction in a classic plasma global model such as the gas phase ground state $O(^3P)$ reacts at the chamber wall to form gas phase ground state O_2 [14]:

$$\mathrm{O}(^3\mathrm{P})(\mathrm{g}) \xrightarrow{\text{surface}} \frac{1}{2}\mathrm{O}_2(\mathrm{g}),$$

its reaction rate coefficient k_s can be written as [14]:

$$k_s = \left[\frac{\Lambda_n^2}{D_O} + \frac{2V(2-\gamma_O)}{Av_O\gamma_O} \right]^{-1}, \tag{3}$$

where γ_O is the sticking coefficient for $O(^3P)$ in the surface reaction. Λ_n is the effective diffusion length of neutral species, which is defined as [14]:

$$\Lambda_n = \left[\left(\frac{\pi}{L}\right)^2 + \left(\frac{2.405}{R}\right)^2 \right]^{-1/2}, \tag{4}$$

where L and R are the length and radius of the cylindrical reactor chamber (see Figure 2); D_O is the neutral **diffusion coefficient** of O, which can be obtained separately for each neutral species as [16]:

$$D_\mathrm{n} = \frac{k_\mathrm{B} T_\mathrm{g} \lambda_\mathrm{n}}{v_\mathrm{n} m_\mathrm{n}}, \tag{5}$$

where $v_n = (8k_\mathrm{B}T_\mathrm{g} / \pi m_\mathrm{n})^{1/2}$ is the **mean thermal speed** of a neutral species; k_B is the Boltzmann constant, which equals to 1.3807 × 10^{-23} J/K; T_g is the neutral gas temperature in kelvin (K); m_n is the mass of the neutral species in kg; λ_n is the **neutral-neutral mean free path**, which is defined as (take the same form as the combined expression from Ref. [14] and Ref. [17] for ion-neutral mean free path):

$$\frac{1}{\lambda_\mathrm{n}} = \sum_{j=1}^{N_j} n_{\mathrm{g},j} \sigma_{\mathrm{n},j} \tag{6}$$

where N_j is the total number of neutral gas species; $n_{\mathrm{g},j}$ is the density of the jth neutral gas species, which has a neutral-neutral scattering cross section of $\sigma_{\mathrm{n},j}$. For O_2 and its child species, $\sigma_{\mathrm{n},j}$ is taken to be 4.1×10^{-19} (m^2) [21], p.245; and for SF_6 and its child species, according to the data provided for other neutral species by Roth [21], p.245, I take the assumed value of 2.5×10^{-19} (m^2), which is half of the corresponding ion-neutral scattering cross section (see the second paragraph below).

The overall mass balance equation of a species A is the sum of the balance equations of all the reactions (gas phase plus surface) that involve A.

The **plasma sheath edge to centre density ratio for positive ions** are different in the axial and radial directions [14]:

$$h_\mathrm{L} \approx 0.86 \left(\frac{1 + 3\alpha/\gamma}{1+\alpha} \right) \left(3 + \frac{L}{2\lambda_\mathrm{i}} \right)^{-\frac{1}{2}}, \tag{7}$$

$$h_\mathrm{R} \approx 0.80 \left(\frac{1 + 3\alpha/\gamma}{1+\alpha} \right) \left(4 + \frac{R}{\lambda_\mathrm{i}} \right)^{-\frac{1}{2}}, \tag{8}$$

where $\gamma = T_\mathrm{e} / T_\mathrm{i}$, T_e is the electron temperature in kelvin, $T_\mathrm{i} \equiv T_\pm = T_\mathrm{g}$ in a plasma global model; α is the **electronegativity**,

$$\alpha = n_- / n_\mathrm{e}, \tag{9}$$

with n_- the total negative ion density and n_e the electron density. λ_i is the **ion-neutral mean free path**, which can be obtained in the same form as Eq. (6) (combine the expressions of Ref. [14] and Ref. [17]):

$$\frac{1}{\lambda_i} = \sum_{j=1}^{N_j} n_{g,j}\sigma_{i,j} ,$$

where $\sigma_{i,\,j}$ is ion-neutral scattering cross section. For O_2 and its child species, $\sigma_{i,\,j}$ is taken to be 7.5×10^{-19} (m^2) [14], and for SF_6 and its child species, due to the lack of reference data, I take the generalized value of 5×10^{-19} (m^2) [17].

The plasma sheath edge to centre density ratio for positive ions [Eqs. (7) and (8)] can be combined to obtain an overall value for the chamber:

$$h = \frac{A_R h_R + A_L h_L}{A} = \frac{A_{eff}}{A} , \tag{10}$$

where $A_R = 2\pi RL$, the area of the cylindrical plasma chamber facing the radial direction; $A_L = 2\pi R^2$, the area of the two circular faces of the cylindrical plasma chamber whose distance defines L; and $A = A_R + A_L$. $A_{eff} = A_R h_R + A_L h_L$ is the **effective area for particle loss** [1], p.333.

The rate coefficient of a positive ion lost to the wall is (Eq. (2) of Ref. [22]):

$$k_{s,i} = u_B h\frac{A}{V} = u_B \frac{A_{eff}}{V} = u_B d_{eff}^{-1} , \tag{11}$$

where $d_{eff} = V/A_{eff}$ is the **effective plasma size for particle loss** [1], p.334, u_B is the **Bohm speed**, the speed of positive ions entering the sheath region:

$$u_B = (e\mathrm{T_e}/m_i)^{1/2} , \tag{12}$$

where e is the electron charge (1.602×10^{-19} C), m_i is the mass of the positive ion in kg, $\mathrm{T_e}$ is the electron temperature in volts.

2.2.1.2 Energy Balance Equation

The energy balance equation allows us to calculate the electron temperature. The general form of an **energy balance equation** can be written as [23], [24]:

$$\frac{dE}{dt}=\frac{P_{\mathrm{ads}}}{V}-\sum_{j=1}^{N_{\mathrm{e,gas}}}k_{\mathrm{e},j}n_{\mathrm{e}}n_{j}\varepsilon_{\mathrm{loss},j}-\sum_{l=1}^{N_{\mathrm{i}}}k_{\mathrm{s,i},l}n_{\mathrm{i},l}\varepsilon_{\mathrm{w}} \tag{13}$$

where E is the **energy density** of electrons; P_{ads} is the input power; $N_{\mathrm{e,gas}}$ is the number of all electron ionization, excitation and elastic collisions; $k_{\mathrm{e},j}$ is the rate coefficient of the electron impact reaction j; n_{e} is the electron density; n_j is the density of the neutral species involved in reaction j; $\varepsilon_{\mathrm{loss},j}$ is the electron energy loss due to collision j, $\varepsilon_{\mathrm{loss},j} = eU_{\mathrm{th}}$ for ionizations and excitations and $\varepsilon_{\mathrm{loss},j} = e\cdot 3\mathrm{T_e}(m_{\mathrm{e}}/M_{\mathrm{n}})$ for elastic collisions, where U_{th} is the ionization or excitation energy threshold in volts, m_{e} and M_{n} are the mass of an electron and the mass of the neutral species involved in the elastic collisions in kg; N_{i} is the number of positive ion species; $k_{\mathrm{s,i},l}$ is the rate coefficient of the surface reaction where a positive ion l is lost to the chamber wall, which is obtained from Eq. (11); ε_{w} is the energy loss when an electron-ion pair lost to the wall, which is defined in Eq. (15). To calculate ε_{w} we need the **plsams sheath potential**, which can be obtained as [1]

$$\Phi=-\mathrm{T_e}\ln\frac{4\bar{u}_{\mathrm{B}}hn_{+}}{n_{\mathrm{e}}v_{\mathrm{e}}}, \tag{14}$$

where n_+ is the total positive ion density, $\bar{u}_{\mathrm{B}}$ is the density-weighted average Bohm speed (see Eq. (23)); $v_{\mathrm{e}} = (8e\mathrm{T_e}/\pi m_{\mathrm{e}})^{1/2}$ is the **mean thermal speed of electrons**. The positive ions enter the sheath edge with Bohm speed $u_{\mathrm{B}} = (e\mathrm{T_e}/m_{\mathrm{i}})^{1/2}$, which gives rise to ion kinetic energy $1/2e\mathrm{T_e}$. Therefore, the energy loss when a positive ion drifts through the sheath is $\varepsilon_{\mathrm{ion,w}} = \Phi + 1/2\ e\mathrm{T_e}$. If Maxwellian electron distribution is assumed, the mean kinetic energy loss per electron due to electron lost to the wall is $\varepsilon_{\mathrm{e,w}} = 2e\mathrm{T_e}$ [15], where $\mathrm{T_e}$ is the electron temperature in volts. The **energy loss due to an electron-ion pair lost to the wall** is

$$\varepsilon_{\mathrm{w}} = \varepsilon_{\mathrm{e,w}} + \varepsilon_{\mathrm{ion,w}} = \frac{5}{2}\mathrm{T_e} + \Phi . \tag{15}$$

The **electron temperature** can be obtained by [24]

$$\mathrm{T_e} = \frac{E}{\frac{3}{2} n_{\mathrm{e}} e}, \tag{16}$$

where E is the **energy density** in Eq. (13).

2.2.1.3 Modified Equations for Electronegative Plasmas

Monahan and Turner [22] have summarised the efforts in extending existing equations into describing electronegative plasma discharge. I have implemented these equations in my models to improve their accuracy.

In their paper, Monahan and Turner [22] referenced Kim, Lieberman and co-workers [25] proposed 1-D plasma sheath edge to centre density ratio for positive ions in electronegative plasmas:

$$h = h_a + h_b + h_c , \tag{17}$$

where

$$h_a \approx \frac{0.86}{[3 + \eta(l_{\mathrm{p}} / \lambda_{\mathrm{i}})]^{1/2}} \frac{1}{1 + \alpha_0}, \tag{18}$$

$$h_b \approx \left[\left(\frac{T_{\mathrm{e}}}{T_-} \right)^{1/2} + \left(\frac{T_{\mathrm{e}}}{T_+} \right)^{1/2} \frac{\eta}{\sqrt{2\pi}} \frac{l_{\mathrm{p}}}{\lambda_{\mathrm{i}}} \right]^{-1} \frac{\alpha_0}{1 + \alpha_0}, \tag{19}$$

$$h_c \approx \left[\left(\frac{T_{\mathrm{e}}}{T_-} \right)^{1/2} + \left(\frac{T_{\mathrm{e}}}{T_+} \right)^{1/2} \frac{n_{\mathrm{i},*}^{1/2} n_{\mathrm{i},0}^{+}}{(n_0^{-})^{3/2}} \right]^{-1}, \tag{20}$$

$$\eta = \frac{2T_+}{T_+ + T_-}, \tag{21}$$

$$n_{\mathrm{i},*} = \frac{15}{56}\left(\frac{8k_{\mathrm{B}}T_+}{\pi\, m_{\mathrm{i}}}\right)^{1/2} \frac{\eta^2}{K_{\mathrm{i,rec}}\lambda_{\mathrm{i}}}. \tag{22}$$

The variables appear through equations (18) to (22) are defined as follows:

λ_{i} : the ion-neutral mean free path of the plasma.

l_{p} : half length of the system, where $l_{\mathrm{p}} = L/2$.

$n_{\mathrm{i},0}^{+}$: the total positive ion density at the centre of the plasma.

n_0^{-} : the total negative ion density at the centre of the plasma.

$\alpha_0 = n_0^{-}/n_{\mathrm{e},0}$: the electronegativity at the centre of the plasma.

T_+ and T_- : the positive and negative ion temperatures in kelvin, for which I made a common assumption that $T_+ \approx T_- \approx T_{\mathrm{g}}$ = constant.

T_{e} : electron temperature in kelvin.

m_{i} : positive ion mass in kg.

$K_{\mathrm{i,\,rec}}$: positive-negative ion recombination coefficient.

A common practice in global modeling is to assign the above quantities with subscript 0 by the values calculated in the global model [22]. For a plasma with multiple positive or negative ion species, $n_{\mathrm{i},0}^{+}$ and n_0^{-} in Eq. (20), m_{i} and $K_{\mathrm{i,\,rec}}$ in Eq. (22) are calculated in a **density-weighted average** fashion [25], for example:

$$m_{\mathrm{i}} = \frac{m_{\mathrm{i},1}n_{\mathrm{i},1} + m_{\mathrm{i},2}n_{\mathrm{i},2} + \ldots}{n_{\mathrm{i},1} + n_{\mathrm{i},2} + \ldots}. \tag{23}$$

Instead of using the expression for h in Eq. (17), Monahan and Turner [22] recommended the following relation:

$$h^2 = h_a^2 + h_b^2 + h_c^2. \tag{24}$$

The recommended Bohm speed of each positive ion entering the plasma sheath for an electronegative plasma is [22]

$$\frac{1}{2}m_+u_B^2 = e\mathrm{T}_e\frac{3\Gamma(\xi_3)^2}{\Gamma(\xi_5)\Gamma(\xi_1)}, \tag{25}$$

where T_e is the electron temperature in volts, m_+ is the mass of the ion in kg, $\xi_p = p/2x$ ($x = 1$ for Maxwellian EEDF, $x = 2$ for Druyvesteyn EEDF).

And the plasma sheath potential for an electronegative plasma is [22]:

$$\left[m_e\frac{\Gamma(\xi_3)^2}{\Gamma(\xi_1)\Gamma(\xi_4)^2}\right]^{1/2}\frac{4}{\bar{n}_{es}}\frac{h\bar{n}_{i0}}{\sqrt{m_i}}$$
$$= \int_{eV_s}^{\infty} c_1(x)(\varepsilon - eV_s)^{1/2}\exp(-c_2(x)\varepsilon^x)d\varepsilon, \tag{26}$$

where $m_e = 9.1 \times 10^{-31}$ kg is the electron mass, $\bar{n}_{es}$ is the electron density at the sheath edge which corresponds to a system of one positive ion species and one negative ion species, I take its value as the density-weighted average of $n_{i,0}^+$ subtracts the density-weighted average of n_0^- in my model; m_i is the density-weighted positive ion mass defined in Eq (23), $\bar{n}_{i0}$ is the density-weighted positive ion density at the plasma centre. For a given T_e, $c_1(x)$ and $c_2(x)$ are defined as [26]:

$$c_1(x) = \frac{x}{\langle\varepsilon\rangle^{3/2}}\frac{\Gamma(\xi_5)^{3/2}}{\Gamma(\xi_3)^{5/2}}, \tag{27}$$

$$c_2(x) = \frac{1}{\langle\varepsilon\rangle^x}\left[\frac{\Gamma(\xi_5)}{\Gamma(\xi_3)}\right]^x, \tag{28}$$

where

$$\langle\varepsilon\rangle = \frac{3}{2}e\mathrm{T}_e, \tag{29}$$

is the mean energy of electrons.

Eq. (26) is an integral equation of V_s, for $x = 1$ (Maxwellian EEDF), it can be solved analytically as:

$$V_s = -\frac{1}{ec_2}\ln\left(c_1^{-1} c_2^{3/2} \frac{8}{\bar{n}_{es}\sqrt{\pi}} \left[m_e \frac{\Gamma(\xi_3)^2}{\Gamma(\xi_1)\Gamma(\xi_4)^2} \right]^{1/2} \frac{h\bar{n}_{i0}}{\sqrt{m_i}} \right) \quad \text{(for } x = 1\text{)} \tag{30}$$

For $x = 2$ (Dryvesteyn EEDF), the integral on the right hand side of Eq. (26) boils down to an Gaussian integral with its lower integration bound being a finite positive number. It is a well known fact that it can not be solved exactly. Gudmundsson has given a numerical solution to Eq. (26) for $x = 2$ as [26]:

$$V_s \approx 3.43\ \mathrm{T_e} \quad \text{(for } x = 2\text{)}. \tag{31}$$

And the energy loss for an electron-ion pair lost to the wall is

$$\varepsilon_w = \left[\frac{\Gamma(\xi_3)\Gamma(\xi_6)}{\Gamma(\xi_5)\Gamma(\xi_4)} + \frac{\Gamma(\xi_3)^2}{\Gamma(\xi_5)\Gamma(\xi_1)} \right] \frac{3}{2} e\mathrm{T_e} + eV_s\,. \tag{32}$$

2.2.2 The Heterogeneous Surface Model

In my SF_6/O_2 plasma model, I developed a heterogeneous (Eley-Rideal mechanisms) surface model to describe the surface processes. For a detailed discussion for the oxygen surface processes, see my follow-up paper on the pure O_2 plasma global model with heterogeneous surface model of an rf discharge [18]. The surface reactions and their initial sticking coefficients (or reaction probabilities, which will be introduced in due course, see section 2.2.2.3 for more details) are listed in Table 9 through Table 11 in chapter 4.

I assume monolayer chemisorption for my models (see section 3.1 for more details), therefore if there exist three chemisorbed species $A_{(s)}$, $B_{(s)}$, $C_{(s)}$ on the surface, the following relation holds:

$$\theta_s = 1 - \theta_A - \theta_B - \theta_C\,, \tag{33}$$

where θ_s is the empty to total *surface adsorption sites* (or simply “surface sites”) ratio, a *surface site* is the fraction of the surface where surface adsorptions can occur.

For simplicity, I also follow the assumptions made by Chorkendorff and Niemantsverdriet [27] for the surface (the mean field approximation): all surface adsorption sites are equivalent and each can be occupied by a single particle only; there's no interaction between adsorbed particles; and the adsorbed species are assumed to distribute randomly over the surface.

I have to point out that fluorination and oxidation processes are not simply monolayer chemisorptions. For example, in the interaction of oxygen with Al surfaces, one has to distinguish chemisorbed oxygen and surface oxides [28]. As oxygen can diffuse into deeper substrate layers [28], oxidation is a process that can go beyond monolayer and can form new surface (e.g. Al_2O_3), which can not be explicitly described in my model. Although the overall surface coverage in my model is below 1 (full coverage), it won't be wise for one to think the “bare surface” we have after running the model is not oxidised or fluorinated.

2.2.2.1 Mass Balance Equations of Neutral Gas Surface Reactions

For a neutral species B chemisorbed on an empty surface site s and forms $B_{(s)}$ on the surface

$$B + s \rightarrow B_{(s)}\,,$$

it's rate coefficient k_s can be written as [4]:

$$k_s = \left(\frac{2V[2 - P_s(1-\theta_B)]}{A v_B P_s (1-\theta_B)} + \frac{\Lambda_B}{D_B} \cdot \frac{V}{A} \right)^{-1}, \tag{34}$$

where P_s is the initial sticking coefficient for surface chemisorptions (or the reaction probability for other surface processes) and $P_s\ (1 - \theta_B) = \gamma_n$ is the sticking coefficient of the surface process as being used to obtain a surface reaction rate coefficient in a classic plasma global model (Eq. (3)); θ_B is the *surface coverage* of $B_{(s)}$, which is defined as the number of $B_{(s)}$ on the surface divided by the total number of surface sites.

2.2.2.2 Mass Balance Equations of Ionic Surface Reactions

All the positive ions are effectively neutralized at the surface for a processing discharge (see, for example, Ref. [1], page 300), thus their reaction probabilities equal to 1. The rate coefficients for such reactions in my model are in the same form as their mass balance equations are in a classic plasma global model (Eq. (11)), except they are limited by the availability of surface sites or, in the case of surface recombination, chemisorbed species. For the following two ionic surface reactions,

$$O^+ + s = O_{(s)}\,, \tag{35}$$

$$O^+ + O_{(s)} = O_2 + s\,, \tag{36}$$

where $O_{(s)}$ is the chemisorbed atomic oxygen on the surface, their rate coefficients are given by

$$\left[u_{B,O^+} h \frac{A}{V}\right]\theta_s\,, \tag{37}$$

$$\left[u_{B,O^+} h \frac{A}{V}\right]\theta_O\,, \tag{38}$$

where θ_s is the unoccupied to total surface sites ratio and θ_O is the surface coverage of $O_{(s)}$. Notice that the above reactions and equations are essentially equivalent to that of a classic plasma global model. To see this, we can add Eq. (35) to Eq. (36) to obtain:

$$2O^+ = O_2 \quad \text{(at the surface)}\,, \tag{39}$$

which is a surface reaction as seen in a classic plasma global model. We can also add Eq. (37) to Eq. (38):

$$\left[u_{\mathrm{B,O^+}} h \frac{A}{V}\right][\theta_{\mathrm{s}} + \theta_{\mathrm{O}}] = \left[u_{\mathrm{B,O^+}} h \frac{A}{V}\right], \tag{40}$$

which is exactly the rate coefficient for the mass and energy balance equations of Eq. (39) in a classic plasma global model. Also, writing the ionic surface reaction rate coefficients in this way ensures that (take reaction (35) for example) when θ_{s} is zero, the surface adsorption reaction's rate is zero, which eventually switches off this reaction channel.

2.2.2.3 The Surface Coverage Balance Equations

For a surface reaction

$$\mathrm{A} + \mathrm{s} \rightarrow \mathrm{A_{(s)}},$$

the **surface coverage balance equation** for the chemisorbed $\mathrm{A_{(s)}}$ can be written as [27]:

$$\frac{d\theta_{\mathrm{A}}}{dt} = k_{\theta}(1-\theta_{\mathrm{A}}). \tag{41}$$

k_{θ} is the rate coefficient for the surface coverage change. I use a simple expression for k_{θ}:

$$k_{\theta} = \frac{P_{\mathrm{s}} \cdot \Gamma}{N_0}, \tag{42}$$

where P_{s} is the initial sticking coefficient or reaction probability depending on the type of the surface reaction; Γ is the adsorbate's flux at the surface; N_0 is the surface site density (sites per m^2). Surface site density varies from material to material. For example, 7.41×10^{18} sites m^{-2} for a β-cristobalite (001) surface [8]. In this work, the surface site density value for oxides, 2.3 × 10^{18} (sites / m^2) (an intermediate value of the recommended values given by Pivovarov [29]), is used in my models.

For a neutral species A, Eq. (42) can be written as [27]:

$$k_\theta = \frac{P_\mathrm{s} \cdot p_\mathrm{A}}{N_0 \sqrt{2\pi \cdot m_\mathrm{A} k_\mathrm{B} T_\mathrm{g}}}, \tag{43}$$

where p_A is the partial pressure of A, which equals to $n_\mathrm{A} k_\mathrm{B} T_\mathrm{g}$, with n_A the density of A obtained in the plasma global model; m_A is the mass of species A in kg; k_B is the Boltzmann constant; T_g is the gas temperature in kelvin. Eq. (43) can be derived in the transition state theory as shown in section 3.2.

For a positive ion A, Eq. (42) can be written as:

$$k_\theta = \frac{P_\mathrm{s} \cdot h u_\mathrm{B} n_\mathrm{A}}{N_0}, \tag{44}$$

where h is the sheath edge to plasma centre positive ion density ratio defined in Eq. (24); u_B is the Bohm speed defined in Eq. (25); for a typical processing discharge, all the positive ions reaching the surface are neutralized (See, for example, Ref. [1], page 300), thus $P_\mathrm{s} = 1$ for all positive ion surface reactions.

The overall surface coverage balance equation for species A is the sum of the surface coverage balance equations of all the surface reactions that involve A.

3 Modelling the Surface Processes

The purpose of this chapter is to show how to theoretically determine a neutral species' surface reaction rate coefficient k_s by using the transition state theory, which is essential to writing the surface coverage balance equations for calculating θ. Although the material in this chapter still leaves out practical methods of deriving the initial sticking coefficients/reaction probabilities for surface reactions (which is beyond the scope of this work), it nevertheless gives a viable way of writing the rate coefficients for the surface coverage balance equations by using the available surface reaction initial sticking coefficients/reaction probabilities reported in other works. It's a long way to go, I'm going to follow the discussions in chapter 3 of Chorkendorff and Niemantsverdriet's book [27] and also show materials from other sources. I will add my own understandings to the materials to make them as clear as possible.

3.1 Introduction

3.1.1 Adsorption Surface Sites on Solid Surfaces

Surface spectroscopic techniques have shown that surface adsorptions can only occur in a fraction of the whole surface area. There exist surface structures where surface adsorptions can only occur when the adsorbates are located on these structures. These surface structures are called **surface sites**. Physically, we can consider the adsorption surface sites on solid surfaces as two-dimensional low potential boxes [30], p.612. When an incoming particle collides with the surface site, its energy and momentum are lost. If this energy exceeds the activation energy of the surface reaction, chemical bond will be formed, and chemisorption will occur. Surface adsorptions are always exothermic [31], p.13.

The adsorption **surface site density** N_0 is defined as the number of surface sites per unit area. Interested readers could refer to Ref. [27], page 172 for more details.

3.1.2 Adsorption of Gases on Solid Surfaces

As stated at the end of section 3.1.1, adsorption sites can be considered as low potential boxes, when an incoming particle collides with a surface, the gas-surface attractive potential can trap the incident particle such that adsorption occurs (so called the “soft-cube model”, see Ref. [31], section 4.3.3). How do we tell if adsorption occurs when a particle strikes a solid surface? One criterion is the time that a particle stays in the vicinity of the surface. As described by Adamson and Gast [30], pp. 601-602, if there's no attraction force at all between the particle and the surface, the particle's time of stay in the vicinity of the surface would be in the order of a molecular vibration time, which is about 10^{-13} seconds. In this case, adsorption does not occur. If attraction forces are present, and the average time of stay τ of the molecule is as large as several vibration periods, we can reasonably consider that adsorption has occurred.

Adsorption phenomena can be customarily divided into two classes, physical adsorption and chemical adsorption. However, the differences between these two adsorption mechanisms are not clearly distinguishable. Generally speaking, in physical adsorption, the process is rapid, reversible and the adsorption energy is low (in the range of the heats of condensation) (Ref. [30], Chapter XVII), the adsorption can result in multilayer formation (Ref. [30], page 618; Ref. [32], page 411). Whereas in chemisorption, the process is slow, and as stated in section 3.1.1, the energy of adsorption is large enough to form chemical bond. The reverse process of chemisorption (i.e. desorption) generally takes much longer time than physical adsorption does, and there's evidence that chemisorption is limited to a monolayer (Ref. [30], page 618; Ref. [32], page 411; also see Ref. [33]).

At low temperatures, physical adsorption is dominating and practically it is the only adsorption mechanism that can be observed, whereas at high temperatures, the reverse is true (because physical adsorption's small energy, at high temperatures, the adsorbates' high energy makes them more likely to overcome the activation energy barrier and become chemisorbed, see Ref. [30], page 601).

3.1.3 Physical Adsorption or Chemical Adsorption?

Adamson and Gast showed that (Ref. [30], Table XVII-1 in page 603) the adsorption energy and adsorption time associated with physical adsorption can range from 1.5 to 9 kcal/mol and 10^{-12} to 10^{-7} s respectively; whereas the adsorption energy and adsorption time of chemisorption can range from 20 to 40 kcal/mol and 100 to 10^{17} s.

The short time scale of physical adsorption means we can imagine particles involved in physical adsorption as Ping-Pong balls bouncing against a wall. Although an adsorption surface site can be occupied by a physically adsorbed particle, it is freed so fast that it won't affect a chemisorbed particle to occupy this surface site. As the adsorption time of physical adsorption is negligible compared to that of chemisorption, and in most papers, physical adsorptions are only considered in the form of the physically adsorbed precursor particles' surface diffusion (which may become chemisorbed or desorb back to gas phase, see the section 3.1.4), and furthermore a common assumption in low pressure plasma modelling is that almost all the input power is coupled to the charged particles (mainly electrons), thus the adsorption energy associated with the physical surface adsorption (physical adsorption involves only neutral particles) doesn't affect the electron temperature. Nevertheless, we can imagine the small energy loss through physical adsorption will be compensated from the plasma chamber's environment. Plus, the gas temperature in my model is relatively high (600 K), based on the discussion at the end of section 3.1.2, we can assume chemical adsorption is dominating. With that said, physical adsorptions are not considered in this work.

3.1.4 Surface Adsorption Mechanisms

A chemical adsorption process [1] can be *indirect* or *direct*, which corresponds to two main surface reaction mechanisms (Ref. [27], section 2.10.1; Ref. [31], section 4.3.3): the Langmuir–Hinshelwood mechanism and the Eley–Rideal mechanism.

The **Langmuir-Hinshelwood** mechanism assumes that all species have to be physically adsorbed before they are able to participate in any surface reactions. That means a gas phase particle can not directly react with a chemisorbed particle at the surface. For a surface reaction to happen, the incident particle is trapped by the surface potential and can freely move on the surface in a physisorbed **precursor state** (Ref. [27], section 3.8.2.1; Ref. [31], section 4.3.3). In this state, an **adsorbate** (particles being adsorbed) can visit several adsorption sites before being chemisorbed or reacting with another chemisorbed particle or desorbing to gas phase. This process can be illustrated in the following reaction for gaseous species A:

$$\mathrm{A} + \mathrm{s} \leftrightarrow \mathrm{A}^{\#}_{(\mathrm{s})} \rightarrow \mathrm{A}_{(\mathrm{s})}\,,$$

where s is an adsorption surface site, $\mathrm{A}^{\#}_{(\mathrm{s})}$ represents the precursor state.

On the other hand, in the **Eley–Rideal** mechanism, a gas phase particle A approaching an empty surface site can be directly chemisorbed; or the gas phase particle A approaching a chemically adsorbed particle $\mathrm{B}_{(\mathrm{s})}$ can directly react with $\mathrm{B}_{(\mathrm{s})}$. This approach can be written as:

$$\mathrm{A} + \mathrm{s} \rightarrow \mathrm{A}_{(\mathrm{s})}\ .$$

3.1.5 The Assumptions about the Surface

Langmuir made the following assumptions about the surface [33]: the adsorption takes place on a plane surface having only one kind of elementary space (i.e. adsorption

---

[1] The treatment for “chemical adsorption” in this work can be extended to surface reactions between gaseous particles and adsorbed particles. See Ref. [8].

surface site) and in which each space can hold only one adsorbed molecule. Chorkendorff and Niemantsverdriet derived the surface coverage balance equation [27], p.49 by employing similar assumptions: (1) the total number of adsorption sites is constant and equal to *M*, (2) all adsorption sites are equivalent and each can be occupied by a single particle only, (3) there's no interaction between adsorbed particles, and (4) the adsorbed particles are assumed to distribute randomly over the surface.

Points (3) and (4) of the above assumptions are called the "**mean field approximation**". However, as stated by Chorkendorff and Niemantsverdriet (Ref. [27], section 2.8.1), on the surface there normally exists attractive or repulsive interactions between adsorbed species. The mean field approximation works well when the interactions between adsorbed species are repulsive and the surface coverage is low; or when the interactions are attractive but the temperature is high, as high temperatures tend to randomize the adsorbed species across the surface. When attractive interactions are strong, even at low coverage, the adsorbed species will gather to form islands on the surface (Figure 3), which breaks down the mean field approximation. In this case, Langmuir-Hinshelwood mechanism is strongly affected as the precursor state adsorbates can only react with the adsorbents at the edge of the islands. For simplicity purpose, and for the facts that I'm modelling for a relatively high surface temperature (above 300 K) and not considering the Langmuir-Hinshelwood mechanism at all, I will assume the mean field approximation is valid throughout my work.

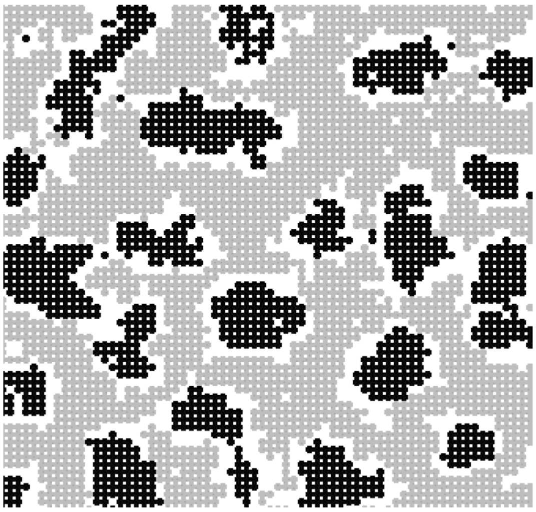

Figure 3 Adsorbed species gather to form islands on solid surface due to attractive interactions between them. (from Ref. [27], section 2.8.1)

3.2 Transition State Theory for Surface Reactions

In this section, I'm going to derive the rate coefficient expression Eq. (43) for the neutral species' surface coverage balance equations by using the transition state theory. An introduction to the transition state theory is given in Appendix B. I'm going to follow the discussion in Chorkendorff and Niemantsverdriet's work in chapter 3 of Ref. [27], and add my own understandings plus discussions from other references to make the material as clear as possible. My previous assumptions about chemisorption and surfaces are still valid (see section 3.1), such as the mean field approximation, which is valid when there's only repulsive interactions between adsorbed species or when the surface temperature is relatively high.

Note that the sticking coefficient $S(\theta)$ (the definition of the terms and symbols will be given in due course) obtained in this section is for single adsorbate formation only (i.e., the adsorbed particle occupies one surface site). For double adsorbate formation (e.g. in one form of the O_2 dissociative chemisorption, both of the dissociated O atoms are adsorbed on the surface, which occupies two adsorption surface sites), $S(\theta)$ has to be written as: [31], p. 336

$$S(\theta) = S_0(T)(1-\theta_\mathrm{A})^2 , \quad \text{for Eley–Rideal direct adsorption} \qquad (45)$$

or [31], p.337

$$S(\theta) = \frac{(1+K)(1-\theta_\mathrm{A})^2}{1+K(1-\theta_\mathrm{A})^2} S_0(T) , \quad \text{for Langmuir-Hinshelwood indirect adsorption} \qquad (46)$$

where K is defined below Eq. (63).

3.2.1 Adsorption of Atoms

(1) Indirect Adsorption

The following discussion for LH indirect adsorption is only valid for an overly ideal condition that all the atoms hitting the surface will be physisorbed to the free-moving precursor state [27], p.115. In practice, the surface coverage balance equation derived for indirect adsorption Eq. (62) has to be tacked with the probability that an atom can be physisorbed and the probability that a diffusing physisorbed atom can reach a surface site. Interested readers can refer to Refs. [8] and [34] for more details. Nevertheless, this section gives the insight of the meaning of the experimentally obtained sticking coefficients for LH indirect adsorptions. Indirect adsorption follows the Langmuir-Hinshelwood mechanism (LH), which I have discussed in section 3.1.4. For indirect adsorption of atoms, the transition state is the 2-D free-moving precursor state on the surface, the reaction scheme can be written as:

$$\mathrm{A} + * \rightleftharpoons \mathrm{A}^{*\#}_{\mathrm{mobile}}. \tag{47}$$

The precursor state atom will soon find a free adsorption surface site or react with some adsorbed species, a chemical bond is formed and the atom is immobile.

$$\mathrm{A}^{*\#}_{\mathrm{mobile}} \rightarrow \mathrm{A}^{*}_{\mathrm{immobile}} \tag{48}$$

Let's denote N_g as the number of gaseous atoms in the system. M is the number of adsorption sites available on the surface, which is a fixed value. $N_0 = M/A$ is the adsorption surface site density with unit of sites per area. Now the mass balance equation can be written as

$$\frac{dN_{\mathrm{A}*}}{dt} = vN^{\#} = vK^{\#}N_\mathrm{g} \tag{49}$$

where $N_{\mathrm{A}*}$ is the number of atoms chemisorbed on the surface, v is the frequency of the transition from the activated complex to the product, $N^{\#}$ is the number of atoms in the precursor transition state, $K^{\#}$ is the equilibrium constant of reaction Eq. (47). The surface coverage of the chemisorbed A$_*$ can be simply written as the number of A$_*$-covered adsorption surface sites divided by the total number of surface sites:

$$\theta_{A*} = \frac{N_{A*}}{M}. \tag{50}$$

Differentiate both sides of Eq. (50) and use Eq. (49) for dN_{A*}/dt, we have the surface coverage balance equation as:

$$\frac{d\theta_{A*}}{dt} = \frac{dN_{A*}}{Mdt} = v\frac{K^{\#}N_{g}}{M} = v\frac{K^{\#}}{M}\frac{V}{k_{B}T}p_{A} \equiv k_{TST}p_{A}, \tag{51}$$

where I've used the ideal gas relation $pV = N_g k_B T \rightarrow N_g = pV/k_B T$. Now the surface coverage balance equation is simply the rate coefficient multiplies the partial pressure of A.

We now derive the rate coefficient k_{TST}. The reaction coordinate (see Appendix B.1) is the very weak vibration between the atom and the surface. The relative partition functions (a detailed discussion of the partition functions is given in Appendix A) for the atoms in the gas phase and in transition state can be written in the canonical partition function form as (the discussions of canonical ensembles and canonical partition functions are given in Appendix A.4, recall that an ensemble of gaseous particles are indistinguishable):

$$Q_{gas} = \frac{q_{g}^{N_g}}{N_g!}; \qquad Q^{\#} = \frac{q^{\# N^{\#}}}{N^{\#}!} \tag{52}$$

where N_g and $N^{\#}$ are the numbers of atoms in gas phase and in transition state.

Apply the transition state theory assumption (see Appendix B.1) that the gas phase is in equilibrium with the transition state, the equilibrium constant can be written as (see, for example, Ref. [1], page 288)

$$K^{\#} = \frac{N^{\#}}{N_g}. \tag{53}$$

Statistical mechanics tells us that in equilibrium, the chemical potential in both states will be equal:

$$\mu_{\mathrm{gas}} = \mu^{\#}, \tag{54}$$

where the chemical potential μ can be written as

$$\mu = -k_{\mathrm{B}} T \frac{\partial \ln Q}{\partial N}. \tag{55}$$

Apply Eq. (52) to Eq. (55) and use the result of Eq. (54), we have

$$-k_{\mathrm{B}} T \frac{\partial}{\partial N_{\mathrm{g}}} \ln \frac{q_{\mathrm{g}}^{N_{\mathrm{g}}}}{N_{\mathrm{g}}!} = -k_{\mathrm{B}} T \frac{\partial}{\partial N^{\#}} \ln \frac{q^{\# N_{\#}}}{N^{\#}!}. \tag{56}$$

Use Stirling's formula

$$\ln(N!) \approx N \ln(N) - N,$$

the left hand side of Eq. (56) can be written as

$$-k_{\mathrm{B}} T \left[\frac{\partial}{\partial N_{\mathrm{g}}} \left(N_{\mathrm{g}} \ln q_{\mathrm{g}} - \ln N_{\mathrm{g}}! \right) \right] = -k_{\mathrm{B}} T \left[\ln q_{\mathrm{g}} + \frac{\partial}{\partial N_{\mathrm{g}}} \left(-N_{\mathrm{g}} \ln N_{\mathrm{g}} + N_{\mathrm{g}} \right) \right]$$

$$= -k_{\mathrm{B}} T \left(\ln q_{\mathrm{g}} - \ln N_{\mathrm{g}} - 1 + 1 \right) = -k_{\mathrm{B}} T \left(\ln q_{\mathrm{g}} - \ln N_{\mathrm{g}} \right).$$

The right hand side has similar result. Equate both sides, we have

$$\ln q_{\mathrm{g}} - \ln N_{\mathrm{g}} = \ln q^{\#} - \ln N^{\#}$$

$$\Rightarrow \ln q_{\mathrm{g}} - \ln q^{\#} = \ln N_{\mathrm{g}} - \ln N^{\#} \Rightarrow \ln \frac{q_{\mathrm{g}}}{q^{\#}} = \ln \frac{N_{\mathrm{g}}}{N^{\#}}$$

$$\Rightarrow \frac{q_{\mathrm{g}}}{q^{\#}} = \frac{N_{\mathrm{g}}}{N^{\#}} \tag{57}$$

Substitute Eq. (57) into Eq. (53), we have

$$K^{\#} = \frac{N^{\#}}{N_{g}} = \frac{q^{\#}}{q_{\mathrm{g}}}, \tag{58}$$

where $q^{\#}$ and q_g are measured with respect to the same zero-point energy (ZPE, see Appendix A.3.2): the ground electronic state of the gaseous atoms. As being discussed in Appendix B.1, if we raise the ZPE of $q^{\#}$ to the transition state, Eq. (58) should be written in the form as shown in Eq (204) (see below Eq. (222) in Appendix B.1.1 for more details on the term $\mathrm{e}^{-\Delta E/k_\mathrm{B}T}$):

$$K^{\#} = \frac{N^{\#}}{N_\mathrm{g}} = \frac{q^{\#}}{q_\mathrm{g}} \mathrm{e}^{-\frac{E_\mathrm{a}}{k_\mathrm{B}T}} . \tag{59}$$

For each individual atom, we have

$$q_\mathrm{g} = q_\mathrm{trans}^{3\mathrm{D}} ; \qquad q^{\#} = q_\mathrm{v}^{\#} q_\mathrm{trans}^{2\mathrm{D}} . \tag{60}$$

Note in Eq. (60), for the transition state partition function $q^{\#}$, the two-dimensional translation of the atom on the surface is the same as its translation in the non-transition state gas phase, except the dimension difference (2D vs. 3D). This is valid in the sense that only the vibration perpendicular to the surface contributes to the reaction coordinate (Ref. [27], page 116).

Substitute Eqs. (59) and (60) in Eq. (51), we have

$$\begin{aligned} \frac{d\theta_{\mathrm{A}*}}{dt} &= v\frac{N_{\#}}{M} = \frac{vK^{\#}}{M}\frac{Vp_\mathrm{A}}{k_\mathrm{B}T} = \frac{vq_v^{\#}}{M}\frac{q_\mathrm{trans}^{2\mathrm{D}}}{q_\mathrm{trans}^{3\mathrm{D}}}\frac{Vp_\mathrm{A}}{k_\mathrm{B}T}\mathrm{e}^{-\frac{\Delta E}{k_\mathrm{B}T}} \\ &= \frac{k_\mathrm{B}T}{Mh}\frac{A(2\pi mk_\mathrm{B}T)/h^2}{V(2\pi mk_\mathrm{B}T)^{3/2}/h^3}\frac{Vp_\mathrm{A}}{k_\mathrm{B}T}\mathrm{e}^{-\frac{\Delta E}{k_\mathrm{B}T}} = \frac{Ap_\mathrm{A}}{M\sqrt{2\pi mk_\mathrm{B}T}}\mathrm{e}^{-\frac{\Delta E}{k_\mathrm{B}T}} \\ &= \frac{p_\mathrm{A}}{N_0\sqrt{2\pi mk_\mathrm{B}T}}\mathrm{e}^{-\frac{\Delta E}{k_\mathrm{B}T}} , \end{aligned} \tag{61}$$

where the energy factor $\mathrm{e}^{-\Delta E/k_\mathrm{B}T}$, as stated above Eq. (59), is due to the zero-point energy of the transition state being set at the transition state itself, it is the surface reaction probability in this case; ΔE is the potential energy barrier, or the activation energy of the surface reaction (see Appendix A.1). Again, I've made the assumption by using the classical limit (see Appendix A.3.2, Eq. (171)) that the partition function of the ultra-weak vibration that acts as the reaction coordinate (see the discussion in Appendix B.1.1 below Eq. (216)) is $q_\mathrm{v}^{\#} \approx k_\mathrm{B}T\,/\,h\nu$, because $h\nu << k_\mathrm{B}T$.

We've obtained the expression for writing a surface coverage balance equation for atoms in indirect adsorption

$$\frac{d\theta_\mathrm{A}}{dt} = \frac{p_\mathrm{A}}{N_0\sqrt{2\pi m k_\mathrm{B}T}}\,\mathrm{e}^{-\frac{\Delta E}{k_\mathrm{B}T}}\,. \tag{62}$$

Eq. (62) is only valid for an overly ideal condition that all the atoms hitting the surface will be physisorbed to the free-moving precursor state [27], p.115. In practice, Eq. (62) has to be tacked with the probability that an atom can be physisorbed and the probability that a diffusing physisorbed atom can reach a surface site. Interested readers can refer to Refs. [8] and [34] for more details.

We recognize that $p_\mathrm{A}/(2\pi m k_\mathrm{B}T)^{1/2}$ is the well known equation for calculating the number of particles hitting a unit surface area per second (i.e., the flux) from kinetic theory. $p_\mathrm{A}/(2\pi m k_\mathrm{B}T)^{1/2}$ multiplies the theoretically or experimentally obtained **sticking coefficient** [2] (for LH indirect adsorption, the sticking coefficient equals to $\mathrm{e}^{-\Delta E/k_\mathrm{B}T}$ multiplied by the probability that an atom can be physisorbed and the probability that a diffusing physisorbed atom can reach a surface site), is the flux of atoms that will be successfully chemisorbed, or in other words, the number of the surface sites being occupied by chemisorption per unit area per second. This value divided by the number of surface sites per unit area N_0 gives rise to the ratio of the surface sites being occupied per unit area per second to the total number of surface sites within a unit area, i.e. the surface coverage change per second.

For indirect adsorption, the sticking coefficient $S(\theta)$ can also be written as a function of the **initial sticking coefficient** (it's also called the **zero-coverage sticking coefficient**) [3] $S_0(T)$ as [31], p. 337:

$$S(\theta) = \frac{(1+K)(1-\theta_\mathrm{A})}{1+K(1-\theta_\mathrm{A})}\,S_0(T)\,, \tag{63}$$

---

[2] Sticking coefficient is the probability that particles being successfully adsorbed when they reach the surface, thus its value is always smaller or equal to 1 (Ref. [27], page 117).

[3] Initial sticking coefficient is the sticking coefficient at zero surface site coverage.

where $K = (k_a^*/k_d^*)$, with $k_a^* = v$, the rate of chemisorbed products formation; $k_d^* = K^{\#}$, the rate of the activated complexes (i.e. the physisorbed precursor state particles) reverse back to gas phase reactants.

(2) Direct Adsorption

In direct adsorption, the atoms enter transition state when they are fully immobilized at the adsorption surface sites. We use the Eley–Rideal mechanism (ER) here and assume there's no precursor state exists. The reaction scheme is

$$\mathrm{A} + * \rightleftarrows \mathrm{A}^{*\#}_{\text{immobile}}, \tag{64}$$

$$\mathrm{A}^{*\#}_{\text{immobile}} \longrightarrow \mathrm{A}^{*}_{\text{immobile}}, \tag{65}$$

An atom at its immobilized transition state has three vibration modes. The one perpendicular to the surface is the reaction coordinate; the other two are parallel to the surface, which contribute to the transition state partition function. The later two vibrations are very weak and comply with the classical limit: $k_B T >> hv$ (Ref. [27], page 116). The partition function of the system in transition state is

$$q^{\#} = q_{\mathrm{v}}^{\#} q_{\text{2D-vib}}^{\#} ,$$

where $q_{\mathrm{v}}^{\#}$ is for the vibration perpendicular to the surface, which is the reaction coordinate; $q_{\text{2D-vib}}^{\#}$ is for the vibration parallel to the surface, which can be decomposed as two vibration modes. If we assume they are the same, and denote each of them as $q'^{\#}_{\text{2D-vib}}$ then

$$q_{\text{2D-vib}}^{\#} = q'^{\#}_{\text{2D-vib}} \cdot q'^{\#}_{\text{2D-vib}} .$$

Apply the classical limit, we have $q'^{\#}_{\text{2D-vib}} = k_{\mathrm{B}}T / h v_{\text{2D-vib}}$. Thus (by similar fashion to Eq. (211))

$$q^{\#}_{\mathrm{2D-vib}} = \left(\frac{k_{\mathrm{B}}T}{hv_{\mathrm{2D-vib}}} \right)^2 \mathrm{e}^{-hv_{\mathrm{2D-vib}}/k_{\mathrm{B}}T} ,$$

where the energy term $hv_{\mathrm{2D-vib}}$ in the exponent is due to a single common (the two vibrations are decomposed from the one vibration parallel to the surface anyway) new ZPE level of the two identical 2-D vibrations (i.e., $hv_{\mathrm{2D-vib}}$ is the correction for the ZPE being raised to the transition state). Also note that associative (non-dissociative) adsorptions usually have zero energy barrier (Ref. [27], page 116).

For the ER surface process Eqs. (64) and (65), let M denote the number of adsorption surface sites, the area of each unit cell that contains one surface site is a^2. The adsorption site density is therefore $N_0 = M/A = 1/a^2$. Assume there are $N_{\#}$ atoms in transition state on the surface, which will occupy $N_{\#}$ adsorption sites. If the number of free adsorption sites is M', the fraction of free sites will be $\theta_* = M'/M = (1- \theta_{\mathrm{A}})$. We also introduce the surface coverage $\theta_{\#} = N_{\#} / M$ for the atoms in the immobilized transition state. In general $\theta_{\#} << \theta_*$ and can be neglected, i.e. $\theta_* - \theta_{\#} \approx \theta_*$.

The gas phase partition function is the same as that of the indirect adsorption:

$$q_{\mathrm{g}} = q^{\mathrm{3D}}_{\mathrm{trans}} \tag{66}$$

The transition state partition function of the system, however, has to be considered with the **weight of configuration** of the adsorbed atoms taken into account. For the process listed in Eq. (64)

$$\mathrm{A} + * \rightleftharpoons \mathrm{A}^{*\#}_{\mathrm{immobile}},$$

the incident atoms reaching the M' free surface sites have two states: in transition state (where the atoms may be chemisorbed or may desorb into gas phase) and in non-transition state (where the atoms will bounce off the surface immediately). In addition to Chorkendorff and Niemantsverdriet's discussion [27], p. 116, I point out here that although the surface sites are distinguishable, in *in*direct adsorption, particles in transition state are mobile, thus they are not associated with a specific surface site (although a precursor transition state particle is going to end up being immobile on a surface site and become chemisorbed, at the moment it becomes immobile, it's not in transition state any more), thus surface sites in indirect adsorption don't play a role in determining the system's state. Therefore I use the canonical partition function for the *in*direct adsorption without considering how all the transition state particles are distributed among the surface sites. However in direct adsorption, as the position of the surface sites are distinguishable, the canonical partition function of the immobile transition state particles not only depends on their own states, but also depends on how they are distributed among the surface sites they sit on. More specifically, let Q represent the number of accessible states of the system composed of M' incident particles sitting on M' free surface sites, where $N_\#$ particles are in transition state, $M' - N_\#$ particles are in non-transition state. We have to consider the fact that these $N_\#$ transition state particles can be distributed in different ways among the M' surface sites. For the first surface site (remember the surface sites are distinguishable, other wise we won't know which site is the first site, which is the second site, etc.), there are M' choices from the M' particles striking the sites, for the second surface site, there are $M' - 1$ choices from the remaining $M' - 1$ particles ..., thus there're $M'!$ choices in total. However, among the $N_\#$ *in*distinguishable particles that are in transition state, exchanging any two of them on the surface sites they already sit on (I call them the *chosen* $N_\#$ surface sites among the M' free surface sites, because these $N_\#$ surface sites are *chosen* to hold the transition state particles) gives the same permutation. There're $N_\#!$ permutations of distributing these particles in the *chosen* $N_\#$ surface sites, all of these permutations are the same because the particles are indistinguishable; similarly for the $M' - N_\#$ *in*distinguishable particles in the non-transition state, there're $(M' - N_\#)!$ permutations of distributing them in the $M' - N_\#$ surface sites that are chosen to hold the non-transition state particles, all are in the same permutation. Thus the weight of configuration (the number of ways of distributing M' particles into M' surface sites) is:

$$\frac{M'!}{N_\#!(M'-N_\#)!}.$$

With that said, the canonical partition function of the system at transition state is

$$Q^\# = \frac{M'!}{N_\#!(M'-N_\#)!}(q^\#)^{N_\#}. \tag{67}$$

Use the transition state theory assumption that the gas phase reactant is in equilibrium with the transition state activated complex, thus their chemical potential are equal $\mu_{\mathrm{gas}} = \mu_{\#}$, recall

$$\mu = -k_{\mathrm{B}}T\frac{\partial \ln Q}{\partial N}.$$

We first calculate the chemical potential:

$$\begin{aligned}\ln Q^{\#} &= \ln\frac{M'!}{N_{\#}!(M'-N_{\#})!}(q^{\#})^{N_{\#}} \\ &= \ln(M'!) + N_{\#}\ln q^{\#} - \ln(N_{\#}!) - \ln(M'-N_{\#})!,\end{aligned}$$

applying Stirling's formula $\ln(N!) \approx N\ln(N) - N$

$$\begin{aligned}\ln Q^{\#} &\approx M'\ln(M') - M' + N_{\#}\ln q^{\#} - N_{\#}\ln(N_{\#}) + N_{\#} \\ &\quad -(M'-N_{\#})\ln(M'-N_{\#}) + (M'-N_{\#}) \\ &= M'\ln(M') + N_{\#}\ln q^{\#} - N_{\#}\ln(N_{\#}) \\ &\quad -(M'-N_{\#})\ln(M'-N_{\#}).\end{aligned} \tag{68}$$

Now we can calculate $\partial \ln Q^{\#}/\partial N_{\#}$, we have

$$\begin{aligned}\frac{\partial \ln Q^{\#}}{\partial N_{\#}} &= 0 + \ln q^{\#} - \ln(N_{\#}) - 1 + \ln(M'-N_{\#}) + 1 \\ &= \ln q^{\#} + \ln\frac{(M'-N_{\#})}{N_{\#}}.\end{aligned} \tag{69}$$

From the derivation below Eq. (56) for the indirect adsorption, we have

$$\frac{d\ln Q_{\mathrm{g}}}{dN_{\mathrm{g}}} = \ln q_{\mathrm{g}} - \ln N_{\mathrm{g}}. \tag{70}$$

As $\mu_{\mathrm{gas}} = \mu_{\#}$ in equilibrium, we can equate Eq. (69) and Eq. (70) to have

$$\ln q^{\#} + \ln\frac{(M'-N_{\#})}{N_{\#}} = \ln q_{\mathrm{g}} - \ln N_{\mathrm{g}}$$

$$\Rightarrow \ln q^{\#} - \ln q_{\mathrm{g}} = \ln \frac{1}{N_{\mathrm{g}}} + \ln \frac{N_{\#}}{(M' - N_{\#})}$$

$$\Rightarrow \ln \frac{q^{\#}}{q_{\mathrm{g}}} = \ln \frac{N_{\#}}{N_{\mathrm{g}}(M' - N_{\#})} \Rightarrow \frac{N_{\#}}{N_{\mathrm{g}}} = (M' - N_{\#}) \frac{q^{\#}}{q_{\mathrm{g}}} \ . \tag{71}$$

But in equilibrium we have

$$K^{\#} = \frac{N_{\#}}{N_{\mathrm{g}}}. \tag{72}$$

Substitute Eq. (71) to Eq. (72), we have

$$K^{\#} = \frac{N_{\#}}{N_{\mathrm{g}}} = (M' - N_{\#}) \frac{q^{\#}}{q_{\mathrm{g}}}. \tag{73}$$

Now, substitute Eq. (73) into Eq. (51), we have

$$\frac{d\theta_{\mathrm{A}}}{dt} = v \frac{N_{\#}}{M} = v \frac{K^{\#} N_{\mathrm{g}}}{M} = \frac{vK^{\#}}{M} \frac{Vp_{\mathrm{A}}}{k_{\mathrm{B}}T} = \frac{v(M' - N_{\#})}{M} \frac{q^{\#}}{q_{\mathrm{g}}} \frac{Vp_{\mathrm{A}}}{k_{\mathrm{B}}T},$$

where I used the ideal gas relation $pV = N_{\mathrm{g}} k_{\mathrm{B}} T \rightarrow N_{\mathrm{g}} = pV/k_{\mathrm{B}}T$. But $M'/M = \theta_{*}$, the fraction of free adsorption surface sites, $N_{\#}/M = \theta_{\#}$, the fraction of adsorption surface sites covered by atoms in transition state, therefore we can write the above equation as

$$\frac{d\theta_{\mathrm{A}}}{dt} = v(\theta_{*} - \theta_{\#}) \frac{q^{\#}}{q_{\mathrm{g}}} \frac{Vp_{\mathrm{A}}}{k_{\mathrm{B}}T}.$$

Following the same discussion in deriving the rate of surface coverage change for indirect adsorption, we raise the zero-point energy of the activated complex to the transition state, therefore we have to multiply $\exp(-E_{\mathrm{a}}/k_{\mathrm{B}}T)$ to the above equation:

$$\frac{d\theta_{\mathrm{A}}}{dt} = v(\theta_{*} - \theta_{\#}) \frac{q^{\#}}{q_{\mathrm{g}}} \frac{Vp_{\mathrm{A}}}{k_{\mathrm{B}}T} \mathrm{e}^{-\frac{E_a}{k_{\mathrm{B}}T}}.$$

Recall from the discussion above Eq. (66), in general $\theta_{\#} << \theta_{*}$ and can be neglected, i.e. $\theta_{*} - \theta_{\#} \approx \theta_{*}$. The partition function of the transition state is $q^{\#} = q_{\mathrm{v}}^{\#} q_{\mathrm{2D-vib}}^{\#}$, where $q_{\mathrm{v}}^{\#}$ and $q_{\mathrm{2D-vib}}^{\#}$ are the partition functions of the atom's vibrations perpendicular and parallel to the surface. $q^{\#}_{\text{2D}-\text{vib}}$ has been written in the form of the product of two identical partition functions of the two weak vibrations decomposed from the atom's vibration parallel to the surface, as discussed below Eq. (65); the atom's vibration perpendicular to the surface, which acts as the reaction coordinate, is also “ultra-weak” (see the discussions in this section below Eq. (65) and in Appendix B.1.1 below Eq. (216)). Therefore we can use the classical limit $hv << k_{\text{B}}T$ for these vibration modes. The electronic partition function is usually unity (see, for example, Ref. [35], page 220; also see Appendix A.3.4 for more details on the electronic partition functions). According to my discussion below Eq. (60), only the degree of freedom that corresponds to the reaction coordinate is significantly raised to the transition state, thus the electronic partition function doesn't produce an energetic exponential term here. Furthermore, as in transition state, the chemical bond between the adsorbate and the adsorbent hasn't been formed, it is reasonable to assume the temperature of the system is the same before and after the atom reaches the transition state, and the atom has the same number of accessible electronic energy states before and after reaching the transition state, thus the electronic partition function in transition state and in gas phase cancel each other in the above equation. Using the 3-D translational partition function from Eq. (163) as q_{g}, we can now write $d\theta_{\text{A}}/dt$ as

$$\begin{aligned}
\frac{d\theta_{\text{A}}}{dt} &= \frac{Vp_{\text{A}}\theta_{*}}{h}\frac{q^{\#}_{\text{2D-vib}}}{q^{\text{3D}}_{\text{trans}}}\mathrm{e}^{-\frac{E_a}{k_{\text{B}}T}} \\
&= \frac{Vp_{\text{A}}\theta_{*}}{h}\frac{\left(\dfrac{k_{\text{B}}T}{hv_{\text{2D-vib}}}\right)^{2}h^{3}}{V(2\pi mk_{\text{B}}T)^{3/2}}\mathrm{e}^{-\frac{(\Delta E+hv_{\text{2D-vib}})}{k_{\text{B}}T}} \\
&= \frac{p_{\text{A}}\theta_{*}}{N_0\sqrt{2\pi mk_{\text{B}}T}}\frac{N_0\left(\dfrac{k_{\text{B}}T}{hv_{\text{2D-vib}}}\right)^{2}h^{2}}{(2\pi mk_{\text{B}}T)}\mathrm{e}^{-\frac{(\Delta E+hv_{\text{2D-vib}})}{k_{\text{B}}T}} \\
&= \frac{p_{\text{A}}\theta_{*}}{N_0\sqrt{2\pi mk_{\text{B}}T}}\frac{N_0 q^{\#}_{\text{2D-vib}}}{q^{\text{2D}}_{\text{trans}}}\mathrm{e}^{-\frac{(\Delta E+hv_{\text{2D-vib}})}{k_{\text{B}}T}} \\
&= \frac{p_{\text{A}}\theta_{*}}{N_0\sqrt{2\pi mk_{\text{B}}T}}S_0(T)
\end{aligned}$$

$$= \frac{(1-\theta_\mathrm{A}) p_\mathrm{A}}{N_0 \sqrt{2\pi m k_\mathrm{B} T}} S_0(T) . \tag{74}$$

Now the surface coverage balance equation becomes:

$$\frac{d\theta_\mathrm{A}}{dt} = \frac{S_0(T) p_\mathrm{A}}{N_0 \sqrt{2\pi m k_\mathrm{B} T}} (1-\theta_\mathrm{A}) , \tag{75}$$

where $S_0(T)$ is the initial sticking coefficient. For direct adsorption, the sticking coefficient is [31], p. 336:

$$S(\theta) = S_0(T)(1 - \theta_\mathrm{A}). \tag{76}$$

For a surface area A of 1 m^2, we can define a **unit cell** as the surface area divided by the number of surface sites per m^2, i.e., the area of the unit cell $a^2 = 1/N_0$. The number of surface sites $M = AN_0 = N_0$. We now can write the initial sticking coefficient as:

$$\begin{aligned} S_0(T) &= \frac{N_0 q^{\#}_{\text{2D-vib}}}{q^{\text{2D}}_{\text{trans}}} \mathrm{e}^{-\frac{E_\mathrm{a}}{k_\mathrm{B} T}} \\ &= \frac{q^{\#}_{\text{2D-vib}}}{\frac{q^{\text{2D}}_{\text{trans}}}{M}} \mathrm{e}^{-\frac{E_\mathrm{a}}{k_\mathrm{B} T}} \\ &= \frac{q^{\#}_{\text{2D-vib}}}{q^{\text{2D}}_{\text{trans-unitcell}}} \mathrm{e}^{-\frac{E_\mathrm{a}}{k_\mathrm{B} T}} , \end{aligned} \tag{77}$$

and

$$q^{\text{2D}}_{\text{trans-unitcell}} = \frac{A}{M} \frac{(2\pi m k_\mathrm{B} T)}{h^2} = a^2 \frac{(2\pi m k_\mathrm{B} T)}{h^2} \tag{78}$$

is the translational partition function of a unit cell.

It would be helpful to give an example with some typical values here (Ref. [27], page 118), such as $a = 2.5$ Å, $T = 300$ K, $m = 40 \times 1.66 \times 10^{-27}$ kg for Ar, $\Delta E = 0$ if the surface reaction is not activated, and $h\nu = 40\ \mathrm{cm}^{-1}$ ($1\ \mathrm{cm}^{-1} = 1.99 \times 10^{-23}$ Joule). Substitute these values into Eq. (77), we have

$$S_0(T) = \frac{\left(\frac{k_{\mathrm{B}}T}{h\nu_{\mathrm{2D\text{-}vib}}}\right)^2 h^2}{a^2(2\pi m k_{\mathrm{B}}T)} \mathrm{e}^{-\frac{(\Delta E + h\nu_{\mathrm{2D\text{-}vib}})}{k_{\mathrm{B}}T}}$$
$$= 4.0\times 10^{-3} \times \left(\frac{k_{\mathrm{B}}T}{h\nu_{\mathrm{2D\text{-}vib}}}\right)^2 \mathrm{e}^{-\frac{h\nu_{\mathrm{2D\text{-}vib}}}{k_{\mathrm{B}}T}} = 0.09 . \tag{79}$$

The limit of the model is that it breaks down when $h\nu$ (energy of the oscillator) becomes large in comparison to $k_{\mathrm{B}}T$, as the attractive potential of the adsorption surface sites becomes so soft that the atoms will start to diffuse over the surface, in which case the two-dimensional vibration has to be replaced by two-dimensional translation. The initial sticking coefficient S_0 normally varies between 1 to 10^{-3}. When the adsorption is activated ($E_{\mathrm{a}} \neq 0$) S_0 tend to be small. Interested readers can refer to Ref. [27], page 118 for more details. The initial sticking coefficient is normally written in an Arrhenius expression [31], p. 336:

$$S_0(T) = S_{00}\mathrm{e}^{-\frac{E_{\mathrm{a}}}{k_{\mathrm{B}}T}} , \tag{80}$$

where S_{00} is the pre-exponential factor.

3.2.2 Adsorption of Molecules

As molecules have internal degrees of freedom, we need to take into account the changes of these degrees of freedom in transition state when we calculate the rate coefficient. We again differentiate two situations.

(1) Indirect Adsorption

The only thing that is different from the analysis for atoms is that the total partition function of molecules has contribution from the internal degrees of freedom. The transition state is again the free moving precursor molecules on the surface. The rate coefficient (or the equilibrium constant in this case, see section 3.2.1 for more details) of the gaseous molecules transferring to the precursor transition state molecules can still be written as

$$K^{\#} = \frac{N_{\#}}{N_{\mathrm{g}}} = \frac{q^{\#}}{q_{\mathrm{gas}}} \tag{81}$$

We can write the surface coverage balance equation based on Eq. (51) as (again, the electronic partition function is assumed to be 1 and is the same for the activated complex and the reactants):

$$\frac{d\theta_{\mathrm{A}}}{dt} = \nu \frac{N_{\#}}{M} = \frac{\nu K^{\#}}{M} \frac{Vp_{\mathrm{A}}}{k_{\mathrm{B}}T} = \frac{\nu V p_{\mathrm{A}}}{Mh} \frac{q^{\mathrm{2D}}_{\mathrm{trans}} q^{\#}_{rot} q^{\#}_{vib}}{q^{\mathrm{3D}}_{\mathrm{trans}} q^{\mathrm{gas}}_{\mathrm{rot}} q^{\mathrm{gas}}_{\mathrm{vib}}} \mathrm{e}^{-\frac{E_{\mathrm{a}}}{k_{\mathrm{B}}T}}$$

$$= \frac{p_{\mathrm{A}}}{N_0\sqrt{2\pi m k_{\mathrm{B}}T}} \frac{q^{\#}_{rot} q^{\#}_{vib}}{q^{\mathrm{gas}}_{\mathrm{rot}} q^{\mathrm{gas}}_{\mathrm{vib}}} \mathrm{e}^{-\frac{E_{\mathrm{a}}}{k_{\mathrm{B}}T}} \tag{82}$$

Thus the surface coverage balance equation for molecules in indirect adsorption is:

$$\frac{d\theta_{\mathrm{A}}}{dt} = \frac{p_{\mathrm{A}}}{N_0\sqrt{2\pi m k_{\mathrm{B}}T}} S(\theta), \tag{83}$$

where $S(\theta)$ is the sticking coefficient for the LH indirect adsorption. Here, we get a similar result as to that for atoms. The surface reaction probability (or the sticking coefficient) in this case is

$$S(\theta) = \frac{q^{\#}_{rot} q^{\#}_{vib}}{q^{\mathrm{gas}}_{\mathrm{rot}} q^{\mathrm{gas}}_{\mathrm{vib}}} \mathrm{e}^{-\frac{E_{\mathrm{a}}}{k_{\mathrm{B}}T}}. \tag{84}$$

Again, Eq. (83) is only valid for an overly ideal condition that all the molecules hitting the surface will be physisorbed to the free-moving precursor state [27], p.115. A practical treatment to the rate coefficient of the LH indirect adsorption has been given below Eq. (62).

(2) Direct Adsorption

In ER direct adsorption, the molecules striking the adsorption surface sites are immobilized in the transition state, so the only degree of freedom a molecule has in the transition state is vibration, and the vibration between the molecule and the surface represents the reaction coordinate. In a similar fashion to the derivation of the surface coverage balance equation for direct adsorption of atoms, the surface coverage balance equation for direct adsorption of molecules is:

$$\frac{d\theta_{\mathrm{A}}}{dt} = \frac{p_{\mathrm{A}}}{N_0\sqrt{2\pi m k_{\mathrm{B}} T}} S_0(T)(1-\theta_{\mathrm{A}}), \qquad (85)$$

where N_0 is the surface site density which is defined as number of adsorption surface sites / surface area, p_{A} is the partial pressure of gaseous species A. $(1 - \theta_{\mathrm{A}})$ is the fraction of available surface sites. $S_0(T)$ is the initial sticking coefficient (or reaction probability if the process is surface reaction) of the adsorption process (see below Eq. (75)). Note that except the detailed expression of the sticking coefficient (or reaction probability), the surface coverage balance equation for molecules in direct adsorption is exactly the same as that for atoms in direct adsorption.

3.3 Conclusion

(1) We can now conclude that the surface coverage balance equation for a non-ionic surface reaction following the Eley–Rideal mechanism such as

$$\mathrm{A} + \mathrm{s} \rightarrow \mathrm{A}_{(\mathrm{s})}$$

can be written as

$$\frac{d\theta_{\mathrm{A}}}{dt}=\frac{p_{\mathrm{A}}}{N_0\sqrt{2\pi m k_{\mathrm{B}}T}}S_0(T)(1-\theta_{\mathrm{A}})$$

where N_0 is the surface site density defined as the number of adsorption surface sites per unit surface area. p_{A} is the partial pressure of gaseous species A. $(1 - \theta_{\mathrm{A}})$ is the fraction of available surface sites. $S_0(T)$ is the initial sticking coefficient (or reaction probability if the process is a surface reaction). The sticking coefficient of the surface process is (see Eq. (76)):

$$S(\theta) = S_0(T)(1 - \theta_{\mathrm{A}}). \qquad (86)$$

(2) The reaction probability $S_0(T)$ is a tricky quantity. From my derivation we can see it is temperature dependent, and is a function of the activation energy E_a, and is proportional to the ratio of the reactants' partition functions in transition state and gas phase. In practice, the reaction probability $S_0(T)$ can be measured experimentally. As stated by Kolasinski: "the study of sticking coefficients (another name of $S_0(T)$) and their dependence on various experimental parameters is itself a study of the validity of CTST (classic transition state theory) and its corrections" (Ref. [35], page 230).

(3) In practice, ΔE (or the activation energy E_a, see Appendix A.1) is often taken as the vibrationally adiabatic barrier [36], p. 151 ("vibrationally adiabatic" means "they occur in the vibrational ground state, with the conservation of the ZPE along the reaction coordinate" [36], p. 156). It can be calculated from the PES (potential energy surface) analysis, or obtained from experiments (Ref. [36], page 6).

4 The SF_6/O_2 Plasma Chemical Kinetics

This chapter lists the chemical kinetics I use for my SF_6/O_2 plasma model. The reaction set, rate coefficients and electron energy thresholds (if relevant) for the gas phase reactions are given in section 4.1. My proposed surface kinetics for the SF_6/O_2 plasma on Al surfaces are given in section 4.2.

4.1 The Gas Phase Reaction Set

The reaction set, rate coefficients and reaction energy thresholds (if relevant) for the gas phase SF_6, O_2 and their child species are listed in Table 1 through Table 8.

4.1.1 Gas Phase Reactions for SF_6 and Its Child Species

The gas phase reactions for SF_6 and its child species have been given in Ref. [4]. For the reader's convenience, this information is listed in Table 1. In my model, I use Kokkoris *et al.*'s [4] reaction set and reaction rate coefficients, as well as the energy thresholds for reactions involving electron energy loss (which are necessary for calculating T_e). In addition to electrons, the following species are present in the model: SF_6, SF_5, SF_4, SF_3, F_2, F, SF_5^+, SF_4^+, SF_3^+, F_2^+, SF_6^- and F^-. Kokkoris *et al.* gave their reaction rate coefficients in the general form of a gas phase reaction in Eq. (87) by either fitting their calculated rate coefficients or citing from other papers [4]:

$$k_G = \exp\left(A + B \ln T_e + \frac{C}{T_e} + \frac{D}{T_e^2} + \frac{E}{T_e^3} \right), \tag{87}$$

where T_e is the electron temperature in volts.

Table 1 Gas phase chemical kinetics for SF_6 plasma.

This table lists the reaction set, rate coefficients and threshold energies for SF_6 and its child species published in Ref. [4]. For each reaction, the first line lists its Druyvesteyn EEDF rate coefficient, the second line lists its Maxwellian EEDF rate coefficient. E_{th} is the energy threshold (electron energy loss) for relevant reactions.

No.	Reaction	E_{th} (V)	EEDF	Rate coefficient (m^3/s) $^{a.}$	Ref.
	Neutral dissociations				
R1K1	$SF_6 + e \rightarrow SF_5 + F + e$	9.6	Druy.	$\exp(-29.35 - 0.2379 \ln T_e - 14.11/T_e - 15.25/T_e^2 - 1.204/T_e^3)$	[4]
			Max.	$\exp(-29.57 - 0.2859 \ln T_e - 13.80/T_e + 1.148/T_e^2 - 0.0781/T_e^3)$	
R2K1	$SF_6 + e \rightarrow SF_4 + 2F + e$	12.1	Druy.	$\exp(-31.61 - 0.2592 \ln T_e - 10.0/T_e - 31.24/T_e^2 - 0.7126/T_e^3)$	[4]
			Max.	$\exp(-31.37 - 0.3721 \ln T_e - 14.42/T_e + 0.5679/T_e^2 - 0.0375/T_e^3)$	
R3K1	$SF_6 + e \rightarrow SF_3 + 3F + e$	16.0	Druy.	$\exp(-40.26 + 3.135 \ln T_e + 5.895/T_e - 64.68/T_e^2 + 0.2607/T_e^3)$	[4]
			Max.	$\exp(-33.91 + 1.237 \ln T_e - 15.06/T_e - 0.0081/T_e^2 - 0.0042/T_e^3)$	
R4K1	$SF_5 + e \rightarrow SF_4 + F + e$	9.6	Druy.	$\exp(-29.36 - 0.2379 \ln T_e - 14.11/T_e - 15.25/T_e^2 - 1.204/T_e^3)$	[4]
			Max.	$\exp(-29.57 - 0.2859 \ln T_e - 13.80/T_e + 1.148/T_e^2 - 0.0781/T_e^3)$	
R5K1	$SF_4 + e \rightarrow SF_3 + F + e$	9.6	Druy.	$\exp(-29.36 - 0.2379 \ln T_e - 14.11/T_e - 15.25/T_e^2 - 1.204/T_e^3)$	[4]
			Max.	$\exp(-29.57 - 0.2859 \ln T_e - 13.80/T_e + 1.148/T_e^2 - 0.0781/T_e^3)$	
R6K1	$F_2 + e \rightarrow 2F + e$	3.16	Druy.	$\exp(-31.44 - 0.6986 \ln T_e - 5.17/T_e - 1.389/T_e^2 - 0.065/T_e^3)$	[4]
			Max.	$\exp(-31.89 - 0.5549 \ln T_e - 5.238/T_e + 0.4288/T_e^2 - 0.0266/T_e^3)$	
R7K1	$F_2 + e \rightarrow 2F + e$	4.34	Druy.	$\exp(-33.44 - 0.2761 \ln T_e - 3.564/T_e - 3.946/T_e^2 - 0.0393/T_e^3)$	[4]
			Max.	$\exp(-33.36 - 0.2982 \ln T_e - 5.312/T_e + 0.1970/T_e^2 - 0.0124/T_e^3)$	
	Ionizations				
R8K1	$SF_6 + e \rightarrow SF_5^+ + 2e + F$	15.5	Druy.	$\exp(-33.66 + 1.212 \ln T_e - 4.594/T_e - 56.66/T_e^2 - 0.3226/T_e^3)$	[4]
			Max.	$\exp(-31.46 + 0.5827 \ln T_e - 15.62/T_e + 0.0392/T_e^2 - 0.0028/T_e^3)$	
R9K1	$SF_6 + e \rightarrow SF_4^+ + 2e + 2F$	18.5	Druy.	$\exp(-37.14 + 1.515 \ln T_e - 4.829/T_e - 80.42/T_e^2 - 0.7924/T_e^3)$	[4]
			Max.	$\exp(-34.41 + 0.7534 \ln T_e - 18.39/Te + 0.0054/T_e^2 - 0.0010/T_e^3)$	
R10K1	$SF_6 + e \rightarrow SF_3^+ + 2e + 3F$	20	Druy.	$\exp(-36.82 + 1.74 \ln T_e - 0.1047/T_e - 98.18/T_e^2 + 0.106/T_e^3)$	[4]
			Max.	$\exp(-33.01 + 0.6900 \ln T_e - 19.32/T_e - 0.1185/T_e^2 + 0.0065/T_e^3)$	
R11K1	$SF_5 + e \rightarrow SF_5^+ + 2e$	11.2	Druy.	$\exp(-34.92 + 1.487 \ln T_e - 2.377/T_e - 29.71/T_e^2 - 0.1449/T_e^3)$	[4]
			Max.	$\exp(-32.78 + 0.8601 \ln T_e - 10.76/T_e - 0.0558/T_e^2 + 0.0025/T_e^3)$	
R12K1	$SF_5 + e \rightarrow SF_4^+ + F + 2e$	14.5	Druy.	$\exp(-36.27 + 1.892 \ln T_e - 1.387/T_e - 50.87/T_e^2 - 0.0758/T_e^3)$	[4]
			Max.	$\exp(-33.20 + 1.0177 \ln T_e - 13.76/T_e - 0.1309/T_e^2 + 0.0075/T_e^3)$	
R13K1	$SF_4 + e \rightarrow SF_4^+ + 2e$	13	Druy.	$\exp(-32.95 + 0.8763 \ln T_e - 10.19/T_e - 31.21/T_e^2 - 3.989/T_e^3)$	[4]
			Max.	$\exp(-32.01 + 0.5939 \ln T_e - 14.83/T_e + 2.220/T_e^2 - 0.9045/T_e^3)$	
R14K1	$SF_4 + e \rightarrow SF_3^+ + F + 2e$	14.5	Druy.	$\exp(-32.75 + 0.8222 \ln T_e - 10.82/T_e - 40.59/T_e^2 - 4.274/T_e^3)$	[4]
			Max.	$\exp(-31.78 + 0.5357 \ln T_e - 16.26/T_e + 1.974/T_e^2 - 0.7729/T_e^3)$	
R15K1	$SF_3 + e \rightarrow SF_3^+ + 2e$	11	Druy.	$\exp(-35.55 + 1.75 \ln T_e - 2.086/T_e - 28.7/T_e^2 - 0.1357/T_e^3)$	[4]
			Max.	$\exp(-33.23 + 1.073 \ln T_e - 10.36/T_e - 0.1016/T_e^2 + 0.0055/T_e^3)$	

R16K1	$F_2 + e \rightarrow F_2^+ + 2e$	15.69	Druy.	$\exp(-35.6 + 1.467 \ln T_e - 6.14/T_e - 57.14/T_e^2 - 0.486/T_e^3)$	[4]
			Max.	$\exp(-33.38 + 0.8249 \ln T_e - 15.96/T_e + 0.0655/T_e^2 - 0.0041/T_e^3)$	
	Attachments				
R17K1	$SF_6 + e \rightarrow SF_5 + F^-$		Druy.	$\exp(-33.43 - 1.173 \ln T_e - 0.5614/T_e + 0.1798/T_e^2 - 0.0145/T_e^3)$	[4]
			Max.	$\exp(-33.40 - 1.061 \ln T_e - 0.1017/T_e - 0.0161/T_e^2 + 0.0006/T_e^3)$	
R18K1	$SF_6 + e \rightarrow SF_6^-$		Druy.	$\exp(-33.46 - 1.5 \ln T_e + 0.0002/T_e - 0.0023/T_e^2 + 0/T_e^3)$	[4]
			Max.	$\exp(-32.77 - 1.500 \ln T_e - 0.0788/T_e + 0.0013/T_e^2 + 0/T_e^3)$	
R19K1	$F_2 + e \rightarrow F + F^-$		Druy.	$\exp(-33.31 - 1.487 \ln T_e - 0.2795/T_e + 0.0109/T_e^2 - 0.0004/T_e^3)$	[4]
			Max.	$\exp(-32.81 - 1.440 \ln T_e - 0.5283/T_e + 0.0558/T_e^2 - 0.0028/T_e^3)$	
	Detachment				
R20K1	$F^- + N \rightarrow F + N + e$, $N = SF_6, SF_5, SF_4, SF_3, F, F_2$			$\exp(-44.39 + 0 \ln T_e + 0/T_e + 0/T_e^2 + 0/T_e^3)$	[4]
R21K1	$SF_6^- + N \rightarrow SF_6 + N + e$ $N = SF_6, SF_5, SF_4, SF_3, F, F_2$			$\exp(-44.98 + 0 \ln T_e + 0/T_e + 0/T_e^2 + 0/T_e^3)$	[4]
	Momentum transfer				
R22K1	$SF_6 + e \rightarrow SF_6 + e$	b.	Druy.	$\exp(-29.15 + 0.2126 \ln T_e - 1.455/T_e + 0.2456/T_e^2 - 0.0141/T_e^3)$	[4]
			Max.	$\exp(-29.23 + 0.2158 \ln T_e - 1.400/T_e + 0.2460/T_e^2 - 0.0145/T_e^3)$	
R23K1 to	$SF_x + e \rightarrow SF_x + e$,	b.	Druy.	Same as (R22K1)	[4]
R25K1	$x = 3, 4, 5$		Max.	Same as (R22K1)	
R26K1	$F_2 + e \rightarrow F_2 + e$	b.	Druy.	$\exp(-29.04 - 0.0987 \ln T_e - 0.4897/T_e - 0.0319/T_e^2 + 0.0055/T_e^3)$	[4]
			Max.	$\exp(-29.01 - 0.1088 \ln T_e - 0.6889/T_e + 0.0533/T_e^2 - 0.0011/T_e^3)$	
R27K1	$F + e \rightarrow F + e$	b.	Druy.	Same as (R26K1)	[4]
			Max.	Same as (R26K1)	
	Excitations				
R28K1	Total vibrational excitation of SF_6	0.09	Druy.	$\exp(-24.81 - 2.174 \ln T_e - 13.47/T_e + 12.45/T_e^2 - 4.4/T_e^3)$	[4]
			Max.	$\exp(-26.84 - 1.461 \ln T_e - 8.346/T_e + 7.867/T_e^2 - 2.913/T_e^3)$	
R29K1	Vibrational excitation of F_2	0.1108	Druy.	$\exp(-33.85 - 1.549 \ln T_e - 0.6197/T_e + 0.0306/T_e^2 - 0.0012/T_e^3)$	[4]
			Max.	$\exp(-33.47 - 1.460 \ln T_e - 0.9889/T_e + 0.1224/T_e^2 - 0.0070/T_e^3)$	
R30K1	Vibrational excitation of F_2	0.2188	Druy.	$\exp(-33.57 - 1.552 \ln T_e - 0.6555/T_e + 0.0224/T_e^2 - 0.0012/T_e^3)$	[4]
			Max.	$\exp(-33.19 - 1.460 \ln T_e - 1.061/T_e + 0.1228/T_e^2 - 0.0071/T_e^3)$	
R31K1	Vibrational excitation of F_2	0.3237	Druy.	$\exp(-33.9 - 1.554 \ln T_e - 0.6757/T_e + 0.0041/T_e^2 - 0.0008/T_e^3)$	[4]
			Max.	$\exp(-33.53 - 1.460 \ln T_e - 1.135/T_e + 0.1202/T_e^2 - 0.0069/T_e^3)$	
R32K1	Vibrational excitation of F_2	0.4205	Druy.	$\exp(-35.01 - 1.546 \ln T_e - 0.6177/T_e - 0.0295/T_e^2 + 0.0001/T_e^3)$	[4]
			Max.	$\exp(-34.62 - 1.460 \ln T_e - 1.1440/T_e + 0.1037/T_e^2 - 0.0060/T_e^3)$	
R33K1	Excitation of F_2	11.57	Druy.	$\exp(-33.89 + 0.7953 \ln T_e - 6.732/T_e - 29.19/T_e^2 - 0.5969/T_e^3)$	[4]
			Max.	$\exp(-32.57 + 0.3734 \ln T_e - 12.69/T_e + 0.3318/T_e^2 - 0.0227/T_e^3)$	
R34K1	Excitation of F_2	13.08	Druy.	$\exp(-39.03 + 1.74 \ln T_e - 3.465/T_e - 40.04/T_e^2 - 0.2956/T_e^3)$	[4]
			Max.	$\exp(-36.25 + 0.9008 \ln T_e - 13.30/T_e + 0.1361/T_e^2 - 0.0107/T_e^3)$	

	Neutral recombinations		
R35K1	$F + SF_5 \rightarrow SF_6$	$\exp(-42.83 +0 \ln T_e +0/T_e +0/T_e^2 +0/T_e^3)$	[4]
R36K1	$F + SF_4 \rightarrow SF_5$	$\exp(-42.83 +0 \ln T_e +0/T_e +0/T_e^2 +0/T_e^3)$	[4]
R37K1	$F + SF_3 \rightarrow SF_4$	$\exp(-42.83 +0 \ln T_e +0/T_e +0/T_e^2 +0/T_e^3)$	[4]
R38K1	$F_2 + SF_5 \rightarrow SF_6 + F$	$\exp(-46.41 +0 \ln T_e +0/T_e +0/T_e^2 +0/T_e^3)$	[4]
R39K1	$F_2 + SF_4 \rightarrow SF_5 + F$	$\exp(-46.41 +0 \ln T_e +0/T_e +0/T_e^2 +0/T_e^3)$	[4]
R40K1	$F_2 + SF_3 \rightarrow SF_4 + F$	$\exp(-46.41 +0 \ln T_e +0/T_e +0/T_e^2 +0/T_e^3)$	[4]
R41K1	$SF_5 + SF_5 \rightarrow SF_6 + SF_4$	$\exp(-41.5 +0 \ln T_e +0/T_e +0/T_e^2 +0/T_e^3)$	[4]
	Ion recombinations		
R42K1 to R49K1	$I^+ + J^- \rightarrow I + J$, I = SF_5, SF_4, SF_3, F_2, J = SF_6, F	$\exp(-29.93 +0 \ln T_e +0/T_e +0/T_e^2 +0/T_e^3)$	[4]
	Ion–molecule reactions		
R50K1	$SF_6 + SF_5^+ \rightarrow SF_6 + SF_3^+ + F_2$	$\exp(-39.65 +0 \ln T_e +0/T_e +0/T_e^2 +0/T_e^3)$	[4]

a. T_e is the electron temperature in volts.

b. The energy loss for momentum transfer reactions R22K1 to R27K1 equals to $3T_e(m_e/m_n)$ [19], [23], where m_e and m_n are the masses of electron and neutral species involved, with unit of kg.

4.1.2 Gas Phase Reactions for O_2 and Its Child Species

The gas phase reactions for O_2 and its child species are listed in Table 2 through Table 6. In addition to electrons, the following species are present in the model: ground state molecular oxygen $O_2(X\,^3\Sigma_g^-)$, metastable molecular oxygen $O_2(a^1\Delta_g)$, $O_2(b^1\Sigma_g^+)$, O_2(Ryd) [the Rydberg states, short for the states $O_2(A^3\Sigma_u^+)$, $O_2(A^3\Delta_u)$, $O_2(c^1\Sigma_u^-)$], ground state atomic oxygen $O(^3P)$, metastable atomic oxygen $O(^1D)$, as well as O_3, O^+, O_2^+ and O^-, O_2^-, O_3^-. I adopt the reaction set in Ref. [14] and part of the Maxwellian EEDF rate coefficients from Gudmundsson and Thorsteinsson's works [14], [37]. I recalculated all the Maxwellian EEDF rate coefficients by integrating my referenced cross section data over the electron temperature range of 1 to 10 eV. Two reactions' rate coefficients listed in Ref. [14] are absent from this work, namely R12K2: $e + e + O^+ \rightarrow O + e$ and R7K4: $e + O_2(a^1\Delta_g) \rightarrow O(^1D) + O^-$ due to the availability of their cross section data. For each reaction, I compared my calculated rate coefficient with that of both Ref. [14] and Ref. [37], if neither of their values agreed with my result, I would use my result and fit it to the electron temperature range of 1 to 10 eV; otherwise, if either value from Ref. [14] or Ref. [37] agreed with my calculated result, I directly used their published value. I also calculated the Druyvesteyn EEDF rate coefficients and fitted them to the same electron temperature range (1 to 10 eV) for all the relevant reactions. The majority of the electron energy loss (i.e., threshold energies) for the relevant reactions are from Kiehlbauch and Graves' work [19]. Other references where some of the values were obtained are also given in the tables. The method for calculating the reaction rate coefficients is listed in Gudmundsson's work Ref. [26]. For more details on the gas phase reactions of O_2 and its child species, please refer to my follow-up paper on the pure O_2 plasma global with heterogeneous surface model [18].

Table 2 Gas phase chemical kinetics for O_2 plasma (1 of 5).

This table lists the reactions involving the ground state $O_2(X\ ^3\Sigma_g^-)$, the ground state $O(^3P)$ and the ions O^-, O^+ and O_2^+. The reactions are adopted from Ref. [14]. For each reaction, the first line lists its Druyvesteyn EEDF rate coefficient, the second line lists its Maxwellian EEDF rate coefficient. If not commented, the electron energy loss E_{th} is from Kiehlbauch and Graves' work [19]. I fitted most of my rate coefficients to their base-10 logarithms, I indicate this by writing "$\log_{10}k$ =" in front of their expressions.

No.	Reaction	E_{th} (V)	EEDF	Rate coefficient [a.]	Ref.
R1K2	$e + O_2 \rightarrow O_2^+ + e + e$	12.06	Druy.	$\log_{10}k = -11.634\ T_e^{0.0473} \exp(1.011/T_e)$ (m^3/s)	[38]
			Max.	$2.34\times10^{-15}\ T_e^{1.03} \exp(-12.29/T_e)$ (m^3/s)	[14]
R2K2	$e + O_2 \rightarrow O + O^-$		Druy.	$\log_{10}k = -13.478\ T_e^{0.0799} \exp(0.3291/T_e)$ (m^3/s)	[39]
			Max.	$1.07\times10^{-15}\ T_e^{-1.39} \exp(-6.26/T_e)$ (m^3/s)	[14]
R3K2	$e + O \rightarrow O^+ + e + e$	13.62	Druy.	$\log_{10}k = -10.897\ T_e^{0.0668} \exp(1.208/T_e)$ (m^3/s)	[40]
			Max.	$4.75\times10^{-15}\ T_e^{0.78} \exp(-14.27/T_e)$ (m^3/s)	[37]
R4K2	$O_2^+ + O^- \rightarrow O_2 + O$			$2.6\times10^{-14}\ (300/T_g)^{0.44}$ (m^3/s)	[14]
R5K2	$O^+ + O^- \rightarrow O + O$			$4\times10^{-14}\ (300/T_g)^{0.43}$ (m^3/s)	[14]
R6K2	$e + O^- \rightarrow O + e + e$	5.5	Druy.	$\log_{10}k = -13.025\ T_e^{-0.0095} \exp(0.1633/T_e)$ (m^3/s)	[41], [42]
			Max.	$4.64\times10^{-14}\ T_e^{0.50} \exp(-3.44/T_e)$ (m^3/s)	[37]
R7K2	$e + O_2 \rightarrow O + O + e$	6.4	Druy.	$\log_{10}k = -11.765\ T_e^{0.0776} \exp(0.5038/T_e)$ (m^3/s)	[43]
			Max.	$\log_{10}k = -13.896\ T_e^{0.0182} \exp(0.1987/T_e)$ (m^3/s)	[43]
R8K2	$O + O^- \rightarrow O_2 + e$			2.3e−16 (m^3/s)	[14]
R9K2	$e + O_2 \rightarrow O^+ + O^- + e$	17	Druy.	$\log_{10}k = -11.843\ T_e^{0.0863} \exp(1.411/T_e)$ (m^3/s)	[44]
			Max.	$7.1\times10^{-17}\ T_e^{0.5} \exp(-17/T_e)$ (m^3/s)	[14]

R10K2	$e + O_2 \rightarrow O + O^+ + 2e$	18.7	Druy.	$\log_{10}k = -11.562\ T_e^{0.0498} \exp(1.557/T_e)$ (m^3/s)	[38]
			Max.	$1.88\times10^{-16}\ T_e^{1.699} \exp(-16.81/T_e)$ (m^3/s)	[14]
R11K2	$O_2 + O^+ \rightarrow O + O_2^+$			$2.1\times10^{-17}\ (300/T_g)^{0.5}$ (m^3/s)	[14]
R12K2	$e + e + O^+ \rightarrow O + e$	−13.62		b.	[14]
R13K2	$e + O_2 + O \rightarrow O_2 + O^-$			10^{-43} (m^6/s)	[14]
R14K2	$O_2^+ + O^- \rightarrow O + O + O$			$2.6\times10^{-14}\ (300/T_g)^{0.44}$ (m^3/s)	[14]
R15K2	$e + O_2 + O^+ \rightarrow O_2 + O$			10^{-38} (m^6/s)	[14]
R16K2	$O_2 + O^+ + O^- \rightarrow O_2 + O_2$			$2.1\times10^{-37}\ (300/T_g)^{2.5}$ (m^6/s)	[14]

a. T_e is the electron temperature in volts, T_g is the gas temperature in K.

b. The cross section data of this reaction is unavailable to us.

Table 3 Gas phase chemical kinetics for O_2 plasma (2 of 5).

This table lists the reactions involving metastable oxygen atom $O(^1D)$. The reactions are adopted from Ref. [14]. For each reaction, the first line lists its Druyvesteyn EEDF rate coefficient, the second line lists its Maxwellian EEDF rate coefficient. If not commented, the electron energy loss E_{th} is from Kiehlbauch and Graves' work [19]. I fitted most of my rate coefficients to their base-10 logarithms, I indicate this by writing "$\log_{10}k =$" in front of their expressions.

No.	Reaction	E_{th} (V)	EEDF	Rate coefficient [a.]	Ref.
R1K3	$e + O_2^+ \rightarrow O + O(^1D)$		Druy.	$\log_{10}k = -14.133\ T_e^{0.0183} \exp(-0.0005/T_e)$ (m^3/s)	[45]
			Max.	$1.889\times10^{-14}\ T_e^{-0.6248} \exp(-0.0331/T_e)$ (m^3/s)	[45]
R2K3	$e + O_2 \rightarrow O + O(^1D) + e$	8.57	Druy.	$\log_{10}k = -10.552\ T_e^{0.0869} \exp(0.7438/T_e)$ (m^3/s)	[43]
			Max.	$\log_{10}k = -13.652\ T_e^{-0.0045} \exp(0.2250/T_e)$ (m^3/s)	[43]
R3K3	$e + O \rightarrow O(^1D) + e$	1.97	Druy.	$\log_{10}k = -13.738\ T_e^{0.0178} \exp(0.1253/T_e)$ (m^3/s)	[46]
			Max.	$1.088\times10^{-14}\ T_e^{-0.4087} \exp(-3.496/T_e)$ (m^3/s)	[46]
R4K3	$O_2 + O(^1D) \rightarrow O_2 + O$			$2.56\times10^{-17} \exp(67/T_g)$ (m^3/s)	[14]
R5K3	$O + O(^1D) \rightarrow O + O$			8×10^{-18} (m^3/s)	[14]
R6K3	$e + O(^1D) \rightarrow O^+ + e + e$	11.65	Druy.	$\log_{10}k = -11.288\ T_e^{0.0569} \exp(1.008/T_e)$ (m^3/s)	b.
			Max.	$4.75\times10^{-15}\ T_e^{0.78} \exp(-12.30/T_e)$ (m^3/s)	b.
R7K3	$e + O(^1D) \rightarrow O + e$	−1.97	Druy.	$1.978\times10^{-14}\ T_e^{-0.4117} \exp(-1.358/T_e)$ (m^3/s)	c.
			Max.	$1.599\times10^{-14}\ T_e^{-0.3247} \exp(-1.218/T_e)$ (m^3/s)	c.
R8K3	$e + O_2 \rightarrow 2O(^1D) + e$	9.97 [47]	Druy.	$\log_{10}k = -13.165\ T_e^{0.0447} \exp(0.7519/T_e)$ (m^3/s)	[43]

			Max.	$\log_{10}k = -16.715\ T_e^{-0.0407} \exp(0.1961/T_e)$ (m^3/s)	[43]

a. T_e is the electron temperature in volts, T_g is the gas temperature in K.

b. Threshold reduced from R3K2.

c. Reverse reaction of R3K3 (detailed balance).

Table 4 Gas phase chemical kinetics for O_2 plasma (3 of 5).

This table lists the reactions involving metastable oxygen molecule $O_2(a^1\Delta_g)$. The reactions are adopted from Ref. [14]. For each reaction, the first line lists its Druyvesteyn EEDF rate coefficient, the second line lists its Maxwellian EEDF rate coefficient. If not commented, the electron energy loss E_{th} is from Kiehlbauch and Graves' work [19]. I fitted most of my rate coefficients to their base-10 logarithms, I indicate this by writing "$\log_{10}k$ =" in front of their expressions.

No.	Reaction	E_{th} (V)	EEDF	Rate coefficient [a.]	Ref.
R1K4	$e + O_2 \rightarrow O_2(a^1\Delta_g) + e$	0.98	Druy.	$2.394\times10^{-14}\ T_e^{-1.199} \exp(-6.244/T_e)$ (m^3/s)	[48]
			Max.	$6.565\times10^{-15}\ T_e^{-0.7442} \exp(-4.325/T_e)$ (m^3/s)	[48]
R2K4	$e + O_2(a^1\Delta_g) \rightarrow O_2^+ + 2e$	11.08	Druy.	$\log_{10}k = -11.905\ T_e^{0.0310} \exp(0.9068/T_e)$ (m^3/s)	b.
			Max.	$2.34\times10^{-15}\ T_e^{1.03} \exp(-11.31/T_e)$ (m^3/s)	[14], b.
R3K4	$e + O_2(a^1\Delta_g) \rightarrow O + O^-$		Druy.	$\log_{10}k = -13.326\ T_e^{0.0715} \exp(0.2506/T_e)$ (m^3/s)	[49] via [39] h.
			Max.	$4.19\times10^{-15}\ T_e^{-1.376} \exp(-5.19/T_e)$ (m^3/s)	[14]
R4K4	$e + O_2(a^1\Delta_g) \rightarrow O_2 + e$	−0.98	Druy.	$6.918\times10^{-15}\ T_e^{-0.5228} \exp(-2.874/T_e)$ (m^3/s)	c.
			Max.	$4.171\times10^{-15}\ T_e^{-0.3438} \exp(-2.305/T_e)$ (m^3/s)	c.
R5K4	$e + O_2(a^1\Delta_g) \rightarrow O + O + e$	5.42	Druy.	$\log_{10}k = -12.190\ T_e^{0.0655} \exp(0.3990/T_e)$ (m^3/s)	d.
			Max.	$\log_{10}k = -13.855\ T_e^{0.0193} \exp(0.1760/T_e)$ (m^3/s)	d.
R6K4	$e + O_2(a^1\Delta_g) \rightarrow O + O^+ + 2e$	17.7	Druy.	$\log_{10}k = -11.499\ T_e^{0.0540} \exp(1.486/T_e)$ (m^3/s)	e.
			Max.	$1.88\times10^{-16}\ T_e^{1.699} \exp(-15.83/T_e)$ (m^3/s)	[14], e.
R7K4	$e + O_2(a^1\Delta_g) \rightarrow O(^1D) + O^-$			f.	
R8K4	$O_2 + O(^1D) \rightarrow O + O_2(a^1\Delta_g)$			10^{-18} (m^3/s)	[14]
R9K4	$O + O_2(a^1\Delta_g) \rightarrow O_2 + O$			1.3×10^{-22} (m^3/s)	[14]
R10K4	$O_2 + O_2(a^1\Delta_g) \rightarrow O_2 + O_2$			$2.2\times10^{-24}\ (300/T_g)^{-0.8}$ (m^3/s)	[14]
R11K4	$O_2(a^1\Delta_g) + O_2(a^1\Delta_g) \rightarrow O_2 + O_2$			$5.5\times10^{-29}\ (300/T_g)^{-0.5}$ (m^3/s)	[14]
R12K4	$e + O_2(a^1\Delta_g) \rightarrow O + O(^1D) + e$	7.59	Druy.	$\log_{10}k = -10.974\ T_e^{0.073} \exp(0.6224/T_e)$ (m^3/s)	g.
			Max.	$\log_{10}k = -13.584\ T_e^{-0.0029} \exp(0.2043/T_e)$ (m^3/s)	g.
R13K4	$O_2 + O + O_2(a^1\Delta_g) \rightarrow 2O_2 + O$			10^{-44} (m^6/s)	[14]

R14K4	$O + O + O \rightarrow O + O_2(a^1\Delta_g)$			$1.93\times10^{-47}\,(300/T_g)^{0.63}$ (m^6/s)	[14]
R15K4	$O_2 + O + O \rightarrow O_2 + O_2(a^1\Delta_g)$			$6.93\times10^{-47}\,(300/T_g)^{0.63}$ (m^6/s)	[14]

a. T_e is the electron temperature in volts, T_g is the gas temperature in K.

b. Threshold reduced from R1K2.

c. Reverse reaction of R1K4 (detailed balance).

d. Threshold reduced from R7K2.

e. Threshold reduced from R10K2.

f. The cross section data of this reaction is unavailable to us.

g. Threshold reduced from R2K3.

h. Ref. [49] is not available to us but is originally referenced by Ref. [14], however, Ref. [39] lists the data we need from Ref. [49].

Table 5 Gas phase chemical kinetics for O_2 plasma (4 of 5).

This table lists the reactions involving O_3 and negative ions O_2^- and O_3^-. The reactions are adopted from Ref. [14]. For each reaction, the first line lists its Druyvesteyn EEDF rate coefficient, the second line lists its Maxwellian EEDF rate coefficient. If not commented, the electron energy loss E_{th} is from Kiehlbauch and Graves' work [19]. I fitted most of my rate coefficients to their base-10 logarithms, I indicate this by writing "$\log_{10}k$ =" in front of their expressions.

No.	Reaction	E_{th} (V)	EEDF	Rate coefficient [a.]	Ref.
R1K5	$O^- + O_2(a^1\Delta_g) \rightarrow O + O_2^-$			4.75×10^{-17} (m^3/s)	[14]
R2K5	$O_2^+ + O_2^- \rightarrow O_2 + O_2$			$2.01\times10^{-13}\,(300/T_g)^{0.5}$ (m^3/s)	[14]
R3K5	$O^+ + O_2^- \rightarrow O_2 + O$			$2.7\times10^{-13}\,(300/T_g)^{0.5}$ (m^3/s)	[14]
R4K5	$e + O_2 + O_2 \rightarrow O_2 + O_2^-$			$2.26\times10^{-42}\,(300/T_g)^{0.5}$ (m^6/s)	[14]
R5K5	$O + O_2^- \rightarrow O_2 + O^-$			3.31×10^{-16} (m^3/s)	[14]
R6K5	$O_2(a^1\Delta_g) + O_2^- \rightarrow O_2 + O_2 + e$			2×10^{-16} (m^3/s)	[14]
R7K5	$e + O_3 \rightarrow O_2 + O^-$		Druy.	$2.060\times10^{-15}\,T_e^{-1.093}\exp(-0.8404/T_e)$ (m^3/s)	[50]
			Max.	$2.185\times10^{-15}\,T_e^{-1.006}\exp(-0.9862/T_e)$ (m^3/s)	[50]
R8K5	$O_2 + O^- \rightarrow O_3 + e$			5×10^{-21} (m^3/s)	[14]
R9K5	$O^- + O_2(a^1\Delta_g) \rightarrow O_3 + e$			1.42×10^{-16} (m^3/s)	[14]
R10K5	$O^+ + O_3 \rightarrow O_2 + O_2^+$			10^{-16} (m^3/s)	[14]
R11K5	$O + O_3 \rightarrow O_2 + O_2$			$1.81\times10^{-17}\exp(-2300/T_g)$ (m^3/s)	[14]

R12K5	$O^- + O_3 \rightarrow O + O_3^-$		5.3×10^{-16} (m^3/s)	[14]
R13K5	$O + O_3^- \rightarrow O_2 + O_2^-$		10^{-16} (m^3/s)	[14]
R14K5	$O + O_3^- \rightarrow O_2 + O_2 + e$		3×10^{-16} (m^3/s)	[14]
R15K5	$O_2^+ + O_3^- \rightarrow O_2 + O_3$		$2\times10^{-13}\,(300/T_g)^{0.5}$ (m^3/s)	[14]
R16K5	$O_2^+ + O_3^- \rightarrow O + O + O_3$		$1.01\times10^{-13}\,(300/T_g)^{0.5}$ (m^3/s)	[14]
R17K5	$O_2^- + O_3 \rightarrow O_2 + O_3^-$		4×10^{-16} (m^3/s)	[14]
R18K5	$O + O_2^- \rightarrow O_3 + e$		3.3×10^{-16} (m^3/s)	[14]
R19K5	$e + O_3 \rightarrow O_2 + O + e$	1.04 [b.]	10^{-14} (m^3/s)	[14]
R20K5	$O_2 + O_2 + O \rightarrow O_2 + O_3$		$6.91\times10^{-40}\,(300/T_g)^{-1.25}$ (m^6/s)	[14]
R21K5	$O_2 + O + O \rightarrow O + O_3$		$2.15\times10^{-40}\exp(345/T_g)$ (m^6/s)	[14]
R22K5	$e + O_2 + O \rightarrow O + O_2^-$		10^{-43} (m^6/s)	[14]
R23K5	$O_2 + O_2 + O^- \rightarrow O_2 + O_3^-$		$1.11\times10^{-42}\,(300/T_g)$ (m^6/s)	[14]
R24K5	$O_2 + O_2^+ + O^- \rightarrow O_2 + O_3$		$2.01\times10^{-37}\,(300/T_g)^{2.5}$ (m^6/s)	[14]
R25K5	$O_2 + O_2 + O \rightarrow O_2 + O_3$		$6.9\times10^{-46}\,(300/T_g)^{1.25}$ (m^6/s)	[14]
R26K5	$e + O_3 \rightarrow O + O_2^-$	Druy.	$7.805\times10^{-16}\,T_e^{-1.385}\exp(-0.6225/T_e)$ (m^3/s)	[51]
		Max.	$9.56\times10^{-16}\,T_e^{-1.26}\exp(-0.95/T_e)$ (m^3/s)	[37]
R27K5	$O_2 + O_3 \rightarrow O_2 + O_2 + O$		$7.26\times10^{-16}\exp(-11400/T_g)$ (m^3/s)	[14]
R28K5	$O_2(a^1\Delta_g) + O_3 \rightarrow O_2 + O_2 + O$		$6.01\times10^{-17}\exp(-2853/T_g)$ (m^3/s)	[14]
R29K5	$O_2^+ + O_2^- \rightarrow O_2 + O + O$		$1.01\times10^{-13}\,(300/T_g)^{0.5}$ (m^3/s)	[14]

---

a. T_e is the electron temperature in volts, T_g is the gas temperature in K.

b. Ref. [1] page 260. The dissociation energy of O_3 is used.

Table 6 Gas phase chemical kinetics for O_2 plasma (5 of 5).

Reactions involving metastable oxygen molecules O_2(b) [short for the state $O_2(b^1\sum_g^+)$] and the Rydberg states O_2(Ryd) [short for the states $O_2(A^3\sum_u^+)$, $O_2(A^3\Delta_u)$, $O_2(c^1\sum_u^-)$]. The reactions are adopted from Ref. [14]. For each reaction, the first line lists its Druyvesteyn EEDF rate coefficient, the second line lists its Maxwellian EEDF rate coefficient. If not commented, the electron energy loss E_{th} is from Kiehlbauch and Graves' work [19]. [O_2(a) is short for the state $O_2(a^1\Delta_g)$]. I fitted most of my rate coefficients to their base-10 logarithms, I indicate this by writing "$\log_{10}k$ =" in front of their expressions.

No.	Reaction	E_{th} (V)	EEDF	Rate coefficient [a.]	Ref.
R1K6	$e + O_2 \rightarrow O_2(b) + e$	1.63	Druy.	$7.676\times10^{-16}\ T_e^{-0.3011} \exp(-3.575/T_e)$ (m^3/s)	[43]
			Max.	$3.24\times10^{-16} \exp(-2.218/T_e)$ (m^3/s)	[14]
R2K6	$e + O_2(a) \rightarrow O_2(b) + e$	0.65	Druy.	$5.757\times10^{-16}\ T_e^{-0.2070} \exp(-2.079/T_e)$ (m^3/s)	b.
			Max.	$3.24\times10^{-16} \exp(-1.57/T_e)$ (m^3/s)	[14], b.
R3K6	$e + O_2(b) \rightarrow O + O + e$	4.77	Druy.	$\log_{10}k = -12.461\ T_e^{0.0579} \exp(0.3343/T_e)$ (m^3/s)	c.
			Max.	$\log_{10}k = -13.831\ T_e^{0.0199} \exp(0.1603/T_e)$ (m^3/s)	c.
R4K6	$e + O_2(b) \rightarrow O + O(^1D) + e$	6.94	Druy.	$\log_{10}k = -11.264\ T_e^{0.0639} \exp(0.5438/T_e)$ (m^3/s)	d.
			Max.	$\log_{10}k = -13.540\ T_e^{-0.0019} \exp(0.1902/T_e)$ (m^3/s)	d.
R5K6	$e + O_2(b) \rightarrow O_2^+ + e + e$	10.43	Druy.	$\log_{10}k = -12.108\ T_e^{0.0344} \exp(0.8362/T_e)$ (m^3/s)	e.
			Max.	$2.34\times10^{-15}\ T_e^{1.03} \exp(-10.663/T_e)$ (m^3/s)	[14], e.
R6K6	$e + O_2(b) \rightarrow O + O^+ + 2e$	17.07	Druy.	$\log_{10}k = -11.492\ T_e^{0.0555} \exp(1.437/T_e)$ (m^3/s)	f.
			Max.	$1.88\times10^{-16}\ T_e^{1.699} \exp(-15.183/T_e)$ (m^3/s)	[14], f.
R7K6	$O^- + O_2(b) \rightarrow O_2 + O + e$			6.9×10^{-16} (m^3/s)	[14]
R8K6	$O + O_2(b) \rightarrow O + O_2(a)$			8.1×10^{-20} (m^3/s)	[14]
R9K6	$e + O_2(b) \rightarrow O_2 + e$	−1.63	Druy.	$1.523\times10^{-15}\ T_e^{-0.1654} \exp(-1.276/T_e)$ (m^3/s)	g.
			Max.	$1.400\times10^{-15}\ T_e^{-0.1522} \exp(-1.276/T_e)$ (m^3/s)	g.
R10K6	$e + O_2(b) \rightarrow O + O^-$		Druy.	$3.513\times10^{-14}\ T_e^{-2.340} \exp(-7.002/T_e)$ (m^3/s)	h.
			Max.	$4.19\times10^{-15}\ T_e^{-1.376} \exp(-4.54/T_e)$ (m^3/s)	[14], h.
R11K6	$O_2 + O_2(b) \rightarrow O_2 + O_2(a)$			$3.79\times10^{-22}\ (300/T_g)^{-2.4} \exp(-281/T_g)$ (m^3/s)	[14]
R12K6	$e + O_2 \rightarrow O_2(Ryd) + e$	4.5	Druy.	$1.859\times10^{-13}\ T_e^{-1.653} \exp(-12.930/T_e)$ (m^3/s)	[52]
			Max.	$\log_{10}k = -14.303\ T_e^{0.0128} \exp(0.1737/T_e)$ (m^3/s)	[52]
R13K6	$e + O_2(a) \rightarrow O_2(Ryd) + e$	3.52	Druy.	$1.128\times10^{-13}\ T_e^{-1.503} \exp(-10.691/T_e)$ (m^3/s)	i.
			Max.	$1.383\times10^{-14}\ T_e^{-0.8141} \exp(-6.814/T_e)$ (m^3/s)	i.
R14K6	$e + O_2(b) \rightarrow O_2(Ryd) + e$	2.87	Druy.	$8.149\times10^{-14}\ T_e^{-1.405} \exp(-9.287/T_e)$ (m^3/s)	i.
			Max.	$\log_{10}k = -14.242\ T_e^{0.0143} \exp(0.1381/T_e)$ (m^3/s)	i.
R15K6	$e + O_2(Ryd) \rightarrow O + O^-$		Druy.	$8.880\times10^{-16}\ T_e^{-1.287} \exp(-0.6282/T_e)$ (m^3/s)	[53]
			Max.	$9.167\times10^{-16}\ T_e^{-1.135} \exp(-0.4412/T_e)$ (m^3/s)	[53]
R16K6	$e + O_2(Ryd) \rightarrow O + O + e$	1.9 [j.]	Druy.	$\log_{10}k = -15.808\ T_e^{-0.0292} \exp(0.0738/T_e)$ (m^3/s)	k.
			Max.	$\log_{10}k = -15.724\ T_e^{-0.0251} \exp(0.0665/T_e)$ (m^3/s)	k.
R17K6	$e + O_2(Ryd) \rightarrow O + O(^1D) + e$	4.07 [l.]	Druy.	$2.648\times10^{-14}\ T_e^{0.0039} \exp(-8.994/T_e)$ (m^3/s)	m.
			Max.	$\log_{10}k = -14.473\ T_e^{-0.0202} \exp(0.1269/T_e)$ (m^3/s)	m.
R18K6	$O + O_2(Ryd) \rightarrow O(^1D) + O_2(b)$			1.35×10^{-18} (m^3/s)	[14]
R19K6	$O_2(a) + O_2(a) \rightarrow O_2 + O_2(b)$			$1.8\times10^{-24}\ (300/T_g)^{-3.8} \exp(700/T_g)$ (m^3/s)	[14]

R20K6	$O_3 + O_2(b) \rightarrow O_2 + O_2 + O$	1.5×10^{-17} (m^3/s)	[14]
R21K6	$O_2 + O_2(Ryd) \rightarrow 2O_2(b)$	2.9×10^{-19} (m^3/s)	[14]
R22K6	$O_2 + 2O \rightarrow O_2 + O_2(Ryd)$	1.2×10^{-46} (m^6/s)	[14]
R23K6	$O_2(Ryd) \rightarrow O_2 + hv$	6.25 (s^{-1})	[14]
R24K6	$O + O_2(Ryd) \rightarrow O_2 + O$	4.95×10^{-18} (m^3/s)	[14]
R25K6	$O + O_2(Ryd) \rightarrow O(^1D) + O_2(a)$	2.7×10^{-18} (m^3/s)	[14]
R26K6	$O_2(b) + O_2(b) \rightarrow O_2 + O_2(a)$	$3.6\times10^{-23}\,(300/T_g)^{-0.5}$ (m^3/s)	[14]

---

a. T_e is the electron temperature in volts, T_g is the gas temperature in K.

b. Threshold reduced from R1K6.

c. Threshold reduced from R7K2.

d. Threshold reduced from R2K3.

e. Threshold reduced from R1K2.

f. Threshold reduced from R10K2.

g. Reverse reaction of R1K6 (detailed balance).

h. Threshold reduced from R3K4.

i. Threshold reduced from R12K6.

j. Reverse reaction of R12K6 (−4.5 V) + R7K2 (6.4 V).

k. Threshold reduced from R3K6.

l. Reverse reaction of R12K6 (−4.5 V) + R2K3 (8.57).

m. Threshold reduced from R4K6.

4.1.3 Gas Phase Reactions between SF_6/O_2's Child Species

The gas phase reactions between SF_6/O_2's child species are listed in Table 7 and Table 8. All the reactions and their rate coefficients in Table 7 are adopted from Hamaoka *et al.*'s work [54]; all except one reaction (R12K8) and their rate coefficients in Table 8 are adopted from Gudmundsson's work [16], where reaction R12K8 and its rate coefficient is from Kimura and Noto's work [55]. In addition to electron and SF_6/O_2's child species, the following species are present: SO_2F_2, SOF_5, SOF_4, SOF_3, SOF_2, FO, FO_2, O_2F_2.

Table 7 Gas phase SF_6-O_2 cross-reaction chemical kinetics (1 of 2).

This table lists the reactions involving SF_6's child species, the ground state $O(^3P)$ and their reaction products. All the reactions and their rate coefficients are adopted from Hmaoka *et al.*'s work [54].

No.	Rection	Rate coefficient	Ref.
R1K7	$SF_5 + O \rightarrow SOF_4 + F$	10^{-18} (m^3/s)	R58 of [54]
R2K7	$SF_4 + O \rightarrow SOF_4$	10^{-20} (m^3/s)	R59 of [54]
R3K7	$SF_4 + O \rightarrow SOF_2 + 2F$	4×10^{-20} (m^3/s)	R60 of [54]
R4K7	$SF_3 + O \rightarrow SOF_2 + F$	10^{-18} (m^3/s)	R61 of [54]
R5K7	$SF_3 + O \rightarrow SOF_3$	10^{-16} (m^3/s)	R62 of [54]
R6K7	$SOF_3 + O \rightarrow SO_2F_2 + F$	10^{-16} (m^3/s)	R63 of [54]
R7K7	$SOF_2 + O \rightarrow SO_2F_2$	10^{-21} (m^3/s)	R64 of [54]
R8K7	$SO_2F_2 + O \rightarrow SOF_2 + O_2$	10^{-18} (m^3/s)	R65 of [54]
R9K7	$SOF_4 \rightarrow SOF_3 + F$	10^{-2} (s^{-1})	R66 of [54]
R10K7	$SOF_3 + F \rightarrow SOF_4$	10^{-16} (m^3/s)	R67 of [54]
R11K7	$SOF_2 + F \rightarrow SOF_3$	2×10^{-21} (m^3/s)	R68 of [54]
R12K7	$SOF_3 + F_2 \rightarrow SOF_4 + F$	10^{-17} (m^3/s)	R72 of [54]
R13K7	$SOF_2 + F_2 \rightarrow SOF_3 + F$	10^{-17} (m^3/s)	R73 of [54]
R14K7	$SF_4 + O + O \rightarrow SO_2F_2 + 2F$	10^{-38} (m^6/s)	R74 of [54]
R15K7	$SOF_4 + F + M \rightarrow SOF_5 + M$ [a.]	10^{-40} (m^6/s)	R78 of [54]
R16K7	$SOF_3 + F + M \rightarrow SOF_4 + M$	10^{-40} (m^6/s)	R79 of [54]
R17K7	$SOF_2 + F + M \rightarrow SOF_3 + M$	10^{-40} (m^6/s)	R80 of [54]

a. Where M represents all the neutral species in the system.

Table 8 Gas phase SF_6-O_2 cross-reaction chemical kinetics (2 of 2).

More reactions involving F, F_2, the ground state $O(^3P)$, the ground state $O_2(X\ ^3\Sigma_g^-)$, O_3, their ions and reaction products. All except one reaction (R12K8) and their rate coefficients are adopted from Gudmundsson's work [16], where reaction R12K8 and its rate coefficient is from Kimura and Noto's work [55].

No.	Rection	Rate coefficient [a.]	Ref.
R1K8	$F^- + O^+ \rightarrow F + O$	$2.7\times10^{-13}\,(300/T_g)^{0.5}$ (m^3/s)	k_{115} of [16]
R2K8	$F^- + O_2^+ \rightarrow F + O_2$	$1.5\times10^{-13}\,(300/T_g)^{0.5}$ (m^3/s)	k_{116} of [16]
R3K8	$O^- + F_2^+ \rightarrow O + F_2$	$1.5\times10^{-13}\,(300/T_g)^{0.5}$ (m^3/s)	k_{117} of [16]
R4K8	$F_2 + O^+ \rightarrow F_2^+ + O$	$1.2\times10^{-17}\,(300/T_g)^{0.5}$ (m^3/s)	k_{120} of [16]
R5K8	$F_2 + O_2^+ \rightarrow F_2^+ + O_2$	$1.2\times10^{-17}\,(300/T_g)^{0.5}$ (m^3/s)	k_{122} of [16]
R6K8	$O + FO_2 \rightarrow FO + O_2$	5.0×10^{-17} (m^3/s)	k_{123} of [16]

R7K8	$O + FO \rightarrow F + O_2$	2.7×10^{-17} (m^3/s)	k_{124} of [16]
R8K8	$O_2 + F + M \rightarrow FO_2 + M$ $^{b.}$	3.1×10^{-45} (m^6/s)	k_{125} of [16]
R9K8	$O_2 + F + F_2 \rightarrow FO_2 + F_2$	1.1×10^{-44} (m^6/s)	k_{126} of [16]
R10K8	$FO_2 + F \rightarrow O_2 + F_2$	9.5×10^{-20} (m^3/s)	k_{127} of [16]
R11K8	$FO_2 + F + O_2 \rightarrow O_2F_2 + O_2$	3.0×10^{-44} (m^6/s)	k_{128} of [16]
R12K8	$F + F + M \rightarrow F_2 + M$	6.77×10^{-40} (m^6/s)	k_{24} of [55]
R13K8	$F + O_3 \rightarrow O_2 + FO$	7.5×10^{-18} (m^3/s)	k_{130} of [16]
R14K8	$FO + FO \rightarrow O_2 + 2F$	$10^{-17}\,(T_g/300)^{0.85}$ (m^3/s)	k_{131} of [16]
R15K8	$FO + FO \rightarrow FO_2 + F$	5.0×10^{-19} (m^3/s)	k_{132} of [16]
R16K8	$FO + FO \rightarrow F_2 + O_2$	3.0×10^{-20} (m^3/s)	k_{133} of [16]
R17K8	$FO_2 + O_3 \rightarrow 2O_2 + FO$	5×10^{-22} (m^3/s)	k_{134} of [16]
R18K8	$O + F_2 \rightarrow FO + F$	10^{-24} (m^3/s)	k_{135} of [16]
R19K8	$F^- + O(^1D) \rightarrow FO + e$	3×10^{-16} (m^3/s)	k_{136} of [16]
R20K8	$F^- + O_2 \rightarrow FO_2 + e$	2×10^{-17} (m^3/s)	k_{137} of [16]

---

a. T_g is the gas temperature in K.

b. Where M represents all the neutral species in the system.

4.2 The Surface Reaction Set

The surface reaction set for the SF_6/O_2 plasma on Al surfaces are given in Table 9 through Table 11. recall that chemisorbed O can only be removed from the surface by directional ion bombardment [6] or by O surface recombinations [8] (see section 2.1), thus my model doesn't have direct surface reactions between SF_6 and O_2's neutral child species.

4.2.1 The Surface Reaction Set for SF_6 and Its Child Species

The surface reactions of SF_6 and its child species on an Al surface for my heterogeneous surface model are listed in Table 9. I adopt most of the surface reactions from Kokkoris *et al.*'s work [4]. Here, I highlight the changes I've made to their reaction set. I also give my interpretations to some of the reactions. The reasoning of the different initial sticking coefficient values of reactions R1S1 and R41S1 in a pure SF_6 plasma and in an SF_6/O_2 plasma follows the same discussion in section 4.2.2 for O and O_2 chemisorptions.

Which is notable in Table 9 is the small initial sticking coefficient for F bare surface chemisorption (R1S1). Although F atoms are more reactive than O atoms due to their outer shell electron structure, F atoms have a quite small chemisorption initial sticking coefficient compared to that of O atoms on Al surfaces. Using this surprisingly small initial sticking coefficient, the small surface coverage value we obtained for θ_F (3.38%, in our simulation for Pessoa *et al.*'s work [13] at 20 mTorr, see Table 15) at the Al plasma chamber wall of a pure SF_6 plasma agrees with the simulated result seen at the feature bottom of a pure SF_6 plasma Si etching simulation reported by Belen *et al.* [2].

Table 9 SF_6 plasma surface chemical kinetics on Al surfaces.
The surface reactions involving SF_6 and its child species. I adopt most of the surface reactions from Table 2 of Kokkoris *et al.*'s work [4], but replace reactions S15, S19, S29-S31 in Table 2 of Ref. [4] by R15S1, R19S1, R29S1-R31S1 in this work to comply with the Eley-Rideal mechanisms on Al surfaces. If not commented, the reactions and their reaction probabilities are from Ref. [4].

No.	Rection [a.]	Reaction Probability
R1S1	$F + s \rightarrow F_{(s)}$	0.15 for pure SF_6 model; 0.0015 for SF_6/O_2 model. [b.]
R2S1 — R4S1	$SF_x + s \rightarrow SF_{x(s)},\ x = 3, 4, 5$	0.08
R5S1	$F + SF_{3(s)} \rightarrow SF_{4(s)}$	0.5
R6S1	$F + SF_{4(s)} \rightarrow SF_{5(s)}$	0.2
R7S1	$F + SF_{5(s)} \rightarrow SF_6$	0.025
R8S1	$F + F_{(s)} \rightarrow F_2 + s$	0.5
R9S1 — R11S1	$SF_x + F_{(s)} \rightarrow SF_{x+1} + s,\ x = 3, 4, 5$	1
R12S1 — R14S1	$SF_x^+ + s \rightarrow SF_{x(s)},\ x = 3, 4, 5$	1 [c.]
R15S1	$F_2^+ + s \rightarrow F_{(s)} + F$ [d.]	1 [c.]
R16S1 — R18S1	$SF_x^+ + F_{(s)} \rightarrow SF_{x(s)} + F,\ x = 3, 4, 5$	1 [c.]
R19S1	$F_2^+ + F_{(s)} \rightarrow F_{(s)} + F_2$ [d.]	1 [c.]
R20S1 — R28S1	$SF_x^+ + SF_{y(s)} \rightarrow SF_{x(s)} + SF_y$ $x = 3, 4, 5$ and $y = 3, 4, 5$	1 [c.]

R29S1 — R31S1	$F_2^+ + SF_{x(s)} \rightarrow F_{(s)} + F + SF_x$, $x = 3, 4, 5$ [d.]	1 [c.]
R32S1 — R40S1	$SF_x + SF_{y(s)} + s \rightarrow SF_{x(s)} + P_{(s)}$ [e.] $x = 3, 4, 5$ and $y = 3, 4, 5$	0.03
R41S1	$F_2 + s = F_{(s)} + F$	0.002 for pure SF_6 model; [b.] 0.2 for SF6/O2 model. [b.]

a. Where s represents an empty surface site, the subscript (s) represents a particle chemisorbed at a surface site.

b. See text.

c. For a typical processing discharge, all the positive ions reaching the surface are neutralized. See, for example, Ref. [1], page 300.

d. Reaction differs from that in Table 2 of Ref. [4].

e. for simplicity, $P_{(s)}$ is considered to have the same property as s, see text for more details.

In Kokkoris *et al.*'s work [4], the surface adsorption of F_2 molecule (R41S1) is absent. However, as I've indicated for [O] in section 4.2.2, the bare surface chemisorptions of atomic and diatomic neutral species of the O element almost dictate [O]'s profile with respect to the O_2 feed composition; and more importantly, to see a large increase in [O] when small SF_6 feed composition is added to a pure O_2 plasma's feedstock gas, a factor of 10^2 has to be multiplied to the initial sticking coefficients of O_2 and its excited species dissociative adsorptions (see section 5.1). Therefore it's worthwhile to include F_2 molecule's surface adsorption into the model. It is known that the chemical kinetics of F_2 on Si surfaces is similar to that of O_2 on Al surfaces [9], thus I assume both F_2 and F_2^+ follow the same surface reaction path as O_2 on Al surfaces (i.e., *abstractive dissociative adsorption* (R41S1); in this work, I only consider Al surfaces, therefore if not stated, the terms “*abstractive adsorption*”, “*dissociative adsorption*” and “*abstractive dissociative adsorption*” are interchangeable for all the diatomic fluorine and oxygen species). Furthermore, I assume the initial sticking coefficient of F_2 dissociative adsorption on Al surfaces is slightly smaller than that of O_2, to be consistent with the small value of F bare surface chemisorption (R1S1), and I take its value as 0.002. Same to O_2 dissociative adsorption, I assume the initial sticking coefficient of F_2 dissociative adsorption in an SF_6/O_2 plasma has a factor of 10^2 increase compared to its value in a pure SF_6 plasma (see section 4.2.2 for the explanation). Actually, my SF_6/O_2 model without reaction R41S1 gave us a very different [F] profile from the experimental results I referred to [13]. It turned our just like the O_2 chemisorption, the F_2 bare surface chemisorption is a key reaction that decides [F] in the discharge. Therefore, this reaction has to be included to get an acceptable [F] profile. I speculate that the reason Kokkoris *et al*'s [4] model still worked even if they had excluded F_2 molecules from the surface reactions was due to the fact that reaction R41S1's small initial sticking coefficient in a pure SF_6 plasma almost closes this reaction channel. My model test has confirmed this, the simulated results of the model without this reaction channel were only slightly different from that of the model with this reaction channel [I tested this by closing the F_2 dissociative chemisorption channel R41S1 in the pure SF_6 plasma model for simulating Pessoa *et al.*'s work [13]. The test model had the same SF_6 feed rate, input power and residence time as the original model (SF_6 input rate = 10 sccm, input power = 14.7 W, $\tau_{\mathrm{res}} = 0.0946$ s, see Table 15 for the results of the original model). Compared to the original SF_6 model, I saw [F] differed by 0.44%, the chamber pressure differed by 0.38%, [F_2] differed by 5.42%, [SF_6] differed by 2.62%, [e] differed by 1.32%, θ_F was 3.38% with the surface reaction R41S1 vs. 3.01% without R41S1.

In addition to adding F_2 to the surface reaction set, I also make the following changes to the surface reactions of Kokkoris *et al.*'s work [4]:

Reaction (S15) in Table 2 of Ref. [4]:

$$\text{(S15) of Ref. [4]:}\quad F_2^+ + 2s \rightarrow 2F_{(s)}$$

is changed to R15S1 to comply with the abstractive adsorption mechanism:

$$\text{(R15S1)}\quad F_2^+ + s \rightarrow F_{(s)} + F\ .$$

For the same reason, surface reaction (S19) in Table 2 of Ref. [4]:

$$\text{(S19) of Ref. [4]:}\quad F_2^+ + F_{(s)} + s \rightarrow 2F_{(s)} + F$$

has to be changed. Furthermore, as stated in comment c. of Table 9, for a typical processing discharge, all the positive ions reaching the surface are neutralized. However, the reaction in question says that F_2^+ can not be neutralized at an $F_{(s)}$ occupied surface site unless there's another empty surface site available. Therefore, for my heterogeneous surface model, I write this reaction as

$$\text{(R19S1)}\quad F_2^+ + F_{(s)} \rightarrow F_{(s)} + F_2\ .$$

This discussion can also be extended to reactions (S29) to (S31) in Table 2 of Ref. [4]

$$\text{(S29)–(S31) of Ref. [4]:}\quad F_2^+ + SF_{x(s)} + s \rightarrow 2F_{(s)} + SF_x\,,\ x = 3,4,5.$$

These reactions will not happen when there's no empty surface sites available, which also contradicts the comment c. of Table 9, thus in my model, I rewrite them as

$$\text{(R29S1)–(R31S1)}\quad F_2^+ + SF_{x(s)} \rightarrow F_{(s)} + F + SF_x\,,\ x = 3,4,5$$

I also make the following interpretations for reactions (R32S1) to (R40S1):

$$SF_x + SF_{y(s)} + s \rightarrow SF_{x(s)} + P_{(s)},\ x = 3, 4, 5 \text{ and } y = 3, 4, 5,$$

where the $P_{(s)}$s are the fluoro-sulfur films formed at the reactor chamber wall. An immediate question is raised as how should $P_{(s)}$ be modelled? If $P_{(s)}$ is not regarded to be equivalent to an empty surface site, I will have to add the thin film $P_{(s)}$ as a new species to the model. However, to my best knowledge, there's no published paper about the detailed chemical kinetics of $P_{(s)}$ to date. For simplicity I assume the thin film has the same adsorbent (i.e., the surface) properties as the original surface, i.e., $P_{(s)}$ is equivalent to a surface adsorption site s, so the net surface site consumption for this reaction is 0. These reactions indicate that the plasma chamber wall should be cleaned periodically to minimize the effect of the reaction-generated thin film on it.

4.2.2 The Surface Reaction Set for O_2 and Its Child Species

My proposed surface reactions for O_2 and its child species on Al surfaces and their initial sticking coefficients / reaction probabilities are listed in Table 10. I give discussions below on the pertinent reactions to this work. For more detailed discussions on these reactions, please see my follow-up paper on the O_2 plasma global model with heterogeneous surface model [18].

Table 10 O_2 plasma surface chemical kinetics on Al surfaces.

This table lists the surface reactions and their initial sticking coefficient/reaction probabilities involving O_2 and its child species.

No.	Rection [a.]	Reaction Probability	Reference
R1S2	$O^+ + s = O_{(s)}$	1 [c.]	
R2S2	$O_2^+ + s = O + O_{(s)}$	1 [c.]	
R3S2	$O + s = O_{(s)}$	0.95 for pure O_2 plasma model; 0.0095 for SF_6/O_2 plasma model. [b.]	b.
R4S2	$O(^1D) + s = O_{(s)}$	Same as R3S2	
R5S2	$O^+ + O_{(s)} = O_2 + s$	1 [c.]	
R6S2	$O_2^+ + O_{(s)} = O_2 + O_{(s)}$	1 [c.]	
R7S2	$O + O_{(s)} = O_2 + s$	0.17	[56]
R8S2	$O(^1D) + O_{(s)} = O_2 + s$	0.17	[56]
R9S2	$O_2 + s = O + O_{(s)}$	0.005 for pure O_2 plasma model; 0.5 for SF_6/O_2 plasma model. [b.]	b.
R10S2	$O_2(a) + s = O + O_{(s)}$	Same as R9S2.	
R11S2	$O_2(b) + s = O + O_{(s)}$	Same as R9S2.	
R12S2	$O_2(Ryd) + s = O + O_{(s)}$	Same as R9S2.	

a. Where s represents an empty surface site, the subscript (s) represents a particle chemisorbed at a surface site.

b. See text.

c. For a typical processing discharge, all the positive ions reaching the surface are neutralized. See, for example, Ref. [1], page 300.

The study of O_2 adsorption on Al surfaces has been a hot topic since early 1990s. Binetti *et al.* [9] supported the abstraction/dissociation hypothesis that for thermal (room temperature) O_2, abstractive adsorption (e.g. reaction R9S2) on Al surfaces dominates and the normal dissociative chemisorption (i.e., the chemisorption of both O atoms from the surface dissociation of O_2) pathway is completely closed. They reported that their theoretical data was consistent with the above hypothesis, such that at energies below about 0.4 eV (4638 K), the abstractive adsorption mechanism dominated. This was later supported by an STM observation that the abstractive to normal chemisorption ratio changed smoothly from 15 at the translational energy of 25 meV (289.9 K) to 2 at the translational energy of 0.8 eV (9275K) [57]. Therefore, in my reaction set, I assume all the diatomic oxygen species follow this reaction path. In this work, for the pure O_2 plasma, I use the O_2 dissociative adsorption initial sticking coefficient on Al surfaces proposed by Brune *et al.* [28] and Lee *et al.* [58], which takes the value of 0.005.

There's surprisingly little work on the initial sticking coefficient of atomic oxygen chemisorption on Al surfaces (R3S2, R4S2). Here I assume its value is close to 1 as seen in literatures for atomic oxygen chemisorption on Si and stainless steel surfaces [8], [14].

A notable scenario in Table 10 is the initial sticking coefficient variations of the atomic and diatomic oxygen species chemisorptions (R3S2, R4S2, R9S2 to R12S2) in a pure O_2 plasma and in an SF_6/O_2 plasma, just as we've seen in Table 9 for F and F_2. The reason for the decrease of the O and $O(^1D)$ initial sticking coefficients in an SF_6/O_2 plasma can't be revealed by my model as the initial sticking coefficients I use are macroscopic quantities. Booth and Sadeghi [3] proposed a 10 to 50 times decrease for O atoms' initial sticking coefficient on stainless-steel reactor walls. The most common explanation for this scenario is that the surface sites favourable to O chemisorption are either fluorinated or occupied by chemisorbed $F_{(s)}$ or $SF_{5(s)}$ [3], [10]. The above mentioned fluoro-sulfur films might have impact on O's initial sticking coefficient too. Incidentally, as I have pointed out in the last paragraph of section 2.2.2, surface chemisorption and surface fluorination/oxidation are two distinct processes, my model is only concerned about surface chemisorption. Thus the “empty surface sites” we see after the simulation are more likely fluorinated or oxidised.

On the other hand, the reason for the increase of O_2 and its excited species abstractive adsorption (R9S2 to R12S2) initial sticking coefficients in an SF_6/O_2 plasma is likely due to the gas temperature rise, as well as surface defects introduced by the surface processes. The gas temperature rise when SF_6 is added to pure O_2 plasma's feedstock gas has been reported in Kechkar *et al.*'s work [10]. Österlund *et al.* [59] found that the initial sticking coefficient of O_2 on Al(111) surface was independent of the surface temperature, and a precursor-mediated sticking on Al(111) surface was not seen in their work. They saw a sharp increase in the initial sticking coefficient of O_2

adsorption on this surface with increased normal incident translational energy. They found the O_2 initial sticking coefficient reached near unity in the energy range of 0.6-2.0 eV. More recently, Binetti and Hasselbrink's experimental work [57] also showed a strong increase of the O_2 abstractive adsorption probability with increasing translational energy. Surface defects introduced by the fluorination/oxidation processes or the fluoro-sulfur films generated by the SF_6 plasma [reactions (R32S1) to (R40S1)] might play a role here too. An example for such increase is given by Somorjai [31], p. 335 for the H_2/platinum system: the $H_2 \leftrightarrow D_2$ dissociation exchanges probabilities on platinum surface are significant different depending on the surface conditions: for stepped (332) surface, the probability is nearly unity; on the flat (111) surface, the probability is lowered by at least an order of magnitude (≈0.1); on a defect-free (111) surface, the probability is less than 10^{-3}.

Owning to the lack of reference data, I take the O surface recombination reaction probability (R7S2, R8S2) to be 0.17, as proposed by Singh *et al.* [56] for a stainless steel surface.

4.2.3 The Surface Reaction Set for the Ions of SF_6 and O_2's Child Species

The surface reaction set for the positive ions of SF_6 and O_2's child species are listed in Table 11. There's no available reference that lists these reactions, thus I could only assume these ionic surface reactions follow the same pattern as seen in Table 9 that due to their high energy, a positive ion A^+ reaching a chemisorbed particle $B_{(s)}$ at the surface will return $B_{(s)}$ to gas phase B and become chemisorbed $A_{(s)}$.

Table 11 The surface reactions for the positive ions of SF_6 and O_2's child species.

No.	Rection [a.]	Reaction Probability
R1S3	$SF_5^+ + O_{(s)} = SF_{5(s)} + O$	1 [b.]
R2S3	$SF_4^+ + O_{(s)} = SF_{4(s)} + O$	1 [b.]
R3S3	$SF_3^+ + O_{(s)} = SF_{3(s)} + O$	1 [b.]

R4S3	$F_2^+ + O_{(s)} = F_{(s)} + FO$	1 [b.]
R5S3	$O^+ + SF_{5(s)} = SF_5 + O_{(s)}$	1 [b.]
R6S3	$O^+ + SF_{4(s)} = SF_4 + O_{(s)}$	1 [b.]
R7S3	$O^+ + SF_{3(s)} = SF_3 + O_{(s)}$	1 [b.]
R8S3	$O^+ + F_{(s)} = O_{(s)} + F$	1 [b.]
R9S3	$O_2^+ + SF_{5(s)} = SF_5 + O_{(s)} + O$	1 [b.]
R10S3	$O_2^+ + SF_{4(s)} = SF_4 + O_{(s)} + O$	1 [b.]
R11S3	$O_2^+ + SF_{3(s)} = SF_3 + O_{(s)} + O$	1 [b.]
R12S3	$O_2^+ + F_{(s)} = O_{(s)} + FO$	1 [b.]

---

a. Where s represents an empty surface site, the subscript (s) represents a particle chemisorbed at a surface site.

b. For a typical processing discharge, all the positive ions reaching the surface are neutralized. See, for example, Ref. [1], page 300.

Two reactions worth mentioning are R4S3 and R12S3, which follow the same pattern as reaction R18K8: $O + F_2 \rightarrow FO + F$. I assume that due to the high energy of the positive ions and the fact that the reaction

$$F + O = FO$$

is endothermic [60] (i.e., absorbs heat), the heat released from the surface reactions will better facilitate the generation of FO. I tested my model by changing the gas phase products of R4S3 and R12S3 to O + F instead of FO under the test conditions for simulating Kechkar *et al.*'s work [10] (see section 5.2). Due to the small densities of the positive ions compared to the neutrals, I didn't see any pronouced differences in any of the model's outputs.

5 Results and Discussion

In this chapter, by investigating the simulation results of my SF_6/O_2 plasma global model with heterogeneous surface model, I will reveal the mechanisms governing the several times increase in [O] (atomic oxygen density) when small SF_6 (e.g. 5% in the feed composition) is added to a pure O_2 plasma's feedstock gas [3], and validate the model with two experimental works. I will show that the chemisorptions of oxygen and fluorine's atomic and diatomic neutral species almost dictate the profiles of [O] and [F] with respect to the O_2 feed composition in an SF_6/O_2 plasma. I have the following main findings in this chapter: (1) The reason for the above mentioned several times increase in [O] is due to a sharp decrease (a factor of 10^2 in my model) in the initial sticking coefficients of O and $O(^1D)$'s chamber wall chemisorptions, plus a sharp increase (a factor of 10^2 in my model) in the initial sticking coefficients of O_2 and its excited species' chamber wall chemisorptions when SF_6 is added to the pure O_2 plasma's feedstock gas, which effectively switches the main contribution channels of $O_{(s)}$ surface coverage from O and $O(^1D)$ chemisorptions (as in the pure O_2 plasma) to O_2 and its excited species chemisorptions (as in the SF_6/O_2 plasma). In an SF_6/O_2 plasma, comparing to a pure O_2 plasma, the smaller $O_{(s)}$ surface coverage reduces atomic O surface recombination, which is the main atomic oxygen loss channel, thus increases [O]. The atomic O produced by the enhanced abstractive adsorptions of the oxygen molecules in the SF_6/O_2 plasma further increases [O]. (2) The increase of O_2's gas phase dissociation reactions rate coefficients is not the reason for the above mentioned large increase in [O]. (3) The main loss channel of the atomic oxygen in O_2 and SF_6/O_2 plasmas is the O surface recombination.

5.1 The Mechanisms that Govern the Large [O] Increase When Small SF_6 is Added to a Pure O_2 Plasma's Feed Composition

The main challenge of this work was to reveal the mechanisms governing the scenario, which was only seen in experiments before, that even small SF_6 was added to the feed composition, a several times' increase of [O] could be seen in an SF_6/O_2 plasma compared to a pure O_2 plasma. The fact that I had an O_2 plasma global model with heterogeneous surface model in my disposal made the exploration of the mechanisms behind the scenario possible.

Table 12 Gas phase O_2, $O_2(a)$, $O_2(b)$ dissociation reactions adopted from Gudmundsson and Thorsteinsson's work [14].

Reaction No.	Reaction
R7K2	$e + O_2 \rightarrow O + O + e$
R2K3	$e + O_2 \rightarrow O + O(^1D) + e$
R8K3	$e + O_2 \rightarrow O(^1D) + O(^1D) + e$
R5K4	$e + O_2(a) \rightarrow O + O + e$
R12K4	$e + O_2(a) \rightarrow O + O(^1D) + e$
R3K6	$e + O_2(b) \rightarrow O + O + e$
R4K6	$e + O_2(b) \rightarrow O + O(^1D) + e$

First, let's investigate the effect of increasing the rate coefficients for O_2, $O_2(a)$ and $O_2(b)$'s gas phase dissociation reactions. These reactions are listed in Table 12. At one stage, my pure O_2 plasma model used some relatively old cross section data from Cosby's work [61] to calculate the rate coefficients for these reactions, and I later used the newer data from Phelps compiled cross section data [43] to improve my model's accuracy. The use of two sets of cross section data at different development stages for the O_2 gas phase dissociation reactions gave me a chance to investigate the effect of increasing the rate coefficients for these reactions to [O] in my pure O_2 plasma model. The plot of the rate coefficients for reaction R7K2 is shown in Figure 4 (the rate coefficients of reactions R2K3 and R8K3 differ from R7K2 by a constant factor (branching ratio), the rate coefficients of the rest of the reactions in Table 12 are threshold reduced from either R7K2 or R2K3, see Ref. [14]).

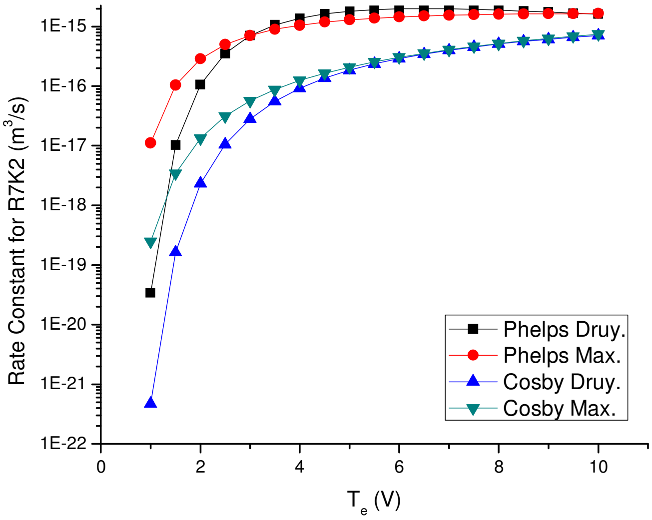

Figure 4 Rate coefficients vs. T_e plot for reaction R7K2: $e + O_2 \rightarrow O + O + e$.
Both rate coefficients calculated by using relatively old cross section data (from Cosby's work Ref. [61], not used in my final model) and new cross section data (from Phelps compiled cross section data Ref. [43], used in my final model) are presented. Max. : Maxwellian EEDF, Druy. : Druyvesteyn EEDF.

For my current test, the model's setup is the same as for simulating Kechkar *et al.*'s work [10] (see Figure 12). For the pure O_2 plasma model, we see that the rate coefficients obtained by using the cross section data from Ref. [43] are about one order of magnitude larger than those from Ref. [61] in the electron temperature range I'm concerned about (3 to 5 V). The corresponding [O]s are plotted in Figure 5. From Figure 5 we can see that the [O]s of the same EEDF but different set of cross section data (either “Max. C.” compared with “Max. P.” or “Druy. C.” compared with “Druy. P.”) are very close, even if the gas phase dissociation rate coefficients for O_2, O_2(a) and O_2(b) are about one order of magnitude different. This scenario is consistent with the results we see in Figure 6, where the close $O_{(s)}$ surface coverage values indicate that the surface processes are not disturbed by this rate coefficient increase, because the partial pressures of atomic oxygen are very close in the models. This can be explained by the fact that the input power is lost to the increased O_2 dissociation reactions, which reduces the power coupled to the ionization processes, thus reduces [e] in the plasma (see Figure 9). In the mass balance equations for the O_2 dissociation reactions listed in Table 12, the increase in the rate coefficients $k_{O2\text{-}dis}$'s is cancelled by the decrease in [e], thus the [O], which is proportional to their product $k_{O2\text{-}dis} \cdot [e]$, won't show a large increase. This can be observed more clearly when I compare the results of the models "1000*$k_{O2\text{-}dis}$" and "Max. P." in the next paragraph.

To further investigate the scenario, I made a test version of the model based on Maxwellian EEDF rate coefficients of the newer cross section data from Ref. [43]. In this test version of the model, I looked into the extreme situation in which a factor of 10^3 was multiplied to the rate coefficients of O_2, $O_2(a)$ and $O_2(b)$ gas phase dissociations (all the reactions listed in Table 12). In this test let's compare the results between the models "1000*$k_{O2\text{-}dis}$" and "Max. P.". The simulated [O] for this model is labelled in Figure 5 as "1000*$k_{O2\text{-}dis}$". We can see that the [O] only has a very small increase here. In Figure 9, we can clearly see the [e] in the model "1000*$k_{O2\text{-}dis}$" is close to 10^3 times smaller than that of the model "Max. P.". Thus for the model "1000*$k_{O2\text{-}dis}$", in the mass balance equations of O_2 dissociation reactions, the 10^3 times' increase in $k_{O2\text{-}dis}$'s is cancelled by the 10^3 times' decrease in [e]. As I have discussed in the previous paragraph, this will generate close [O]s in the two models. This test has confirmed that with the same input power coupled to electrons, the increase in O_2 and its excited species' electron gas-phase dissociation rate coefficients is not the reason for a large [O] increase.

To reveal the scenario where [O] has a significant increase, I made another test version of the model, which was also based on the Maxwellian EEDF rate coefficients calculated from Ref. [43]'s cross section data. This time, I made the initial sticking coefficients of the two atomic oxygen surface chemisorptions:

$$\text{(R3S2) } O + s = O_{(s)} \quad \text{and} \quad \text{(R4S2) } O(^1D) + s = O_{(s)}$$

100 times smaller. The simulated [O] for this model is labelled "P_s" in Figure 5.

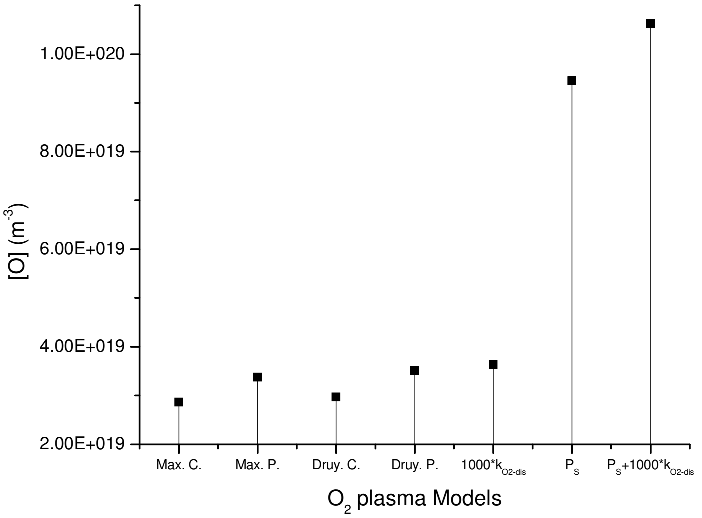

Figure 5 Simulated [O] for pure O_2 plasma under various manufactured conditions.

The model was simulated under two sets of rate coefficients for O_2, O_2(a), O_2(b) gas phase dissociation reactions listed in Table 12 and three manufactured conditions. “Max. C. / P.”: Maxwellian EEDF rate coefficients of cross section data from Ref. [61]/Ref. [43]; “Druy. C. / P.”: Druyvesteyn EEDF rate coefficients of cross section data from Ref. [61]/Ref. [43]; “1000$*k_{O2\text{-}dis}$”: multiply 1000 to the rate coefficients of the reactions listed in Table 12 in the Maxwellian EEDF O_2 plasma model which uses cross section data from Ref. [43]; “P_s”: make the initial sticking coefficients of reactions R3S2 and R4S2 100 times smaller in the Maxwellian EEDF O_2 plasma model which uses cross section data from Ref. [43]; “P_s+1000$*k_{O2\text{-}dis}$”: combine the test conditions of the previous two models. The model's setup was the same as for simulating Kechkar *et al.*'s work [10] (see Figure 12), the input power was kept to 343.605 W, the steady state chamber pressure was kept to 100 mTorr (13.3 Pa) for all tests.

From Figure 5 we can see that [O] of “P_s” is a factor of 2.80 larger than [O] of “Max. P.”. The reason for this increase is simply because the chemisorption of atomic oxygen [reactions (R3S2) and (R4S2)] were significantly reduced, thus there was much less O surface recombination presursor $O_{(s)}$ on the surface (see Figure 6), which significantly reduced the O surface loss. The above tests have clearly shown that under the same input power and chamber pressure, [O] is decided by the surface processes, not the O_2 gas phase dissociation processes. For the model “P_s+1000$*k_{O2\text{-}dis}$”, I combined the above two models' test conditions, in which I reduced the initial sticking coefficients of O and O(^{1}D) chemisorptions by a factor of 10^2, and multiplied 10^3 to the rate coefficients of the O_2 gas phase dissociation reactions listed in Table 12. As expected, we don't see large increase in [O] compared to the model “P_s” in Figure 5. As I will discuss below, the main effect of this combined test condition is to decrease [e] in the plasma.

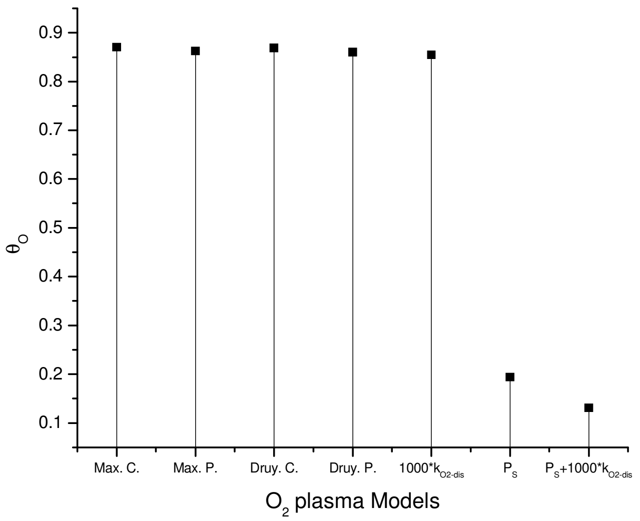

Figure 6 Simulated θ_O for pure O_2 plasma under various manufactured conditions.

The O surface coverage θ_O was simulated under two sets of rate coefficients for O_2, O_2(a), O_2(b) gas phase dissociation reactions listed in Table 12 and three manufactured conditions. The labels of the O_2 plasma models and the test conditions are explained in Figure 5.

The values of T_e for the various test versions of the pure O_2 plasma model are shown in Figure 8. Here we see that T_e in "Max. P." is higher than T_e in "Max. C." and T_e in "Druy. P." is higher than T_e in "Druy. C.", which is owing to the fact that the new rate coefficients of cross section data from Ref [43] significantly increase the rate of dissociation of O_2, which in turn increase the energy loss for electrons, and decrease the average electron energy (and the electron temperature). However, the increased lower energy electron population favours electron attachment, and is consumed in the attachment processes [10]. At the end of the simulation, the fraction of higher energy electrons in the electron population is higher, thus the average electron energy (and electron temperature) increases. As reported by Gudmundsson and Thorsteinsson [14], in a pure O_2 plasma, the dominant electron attachment channels are the dissociative attachment of oxygen molecules: (R2K2) $e + O_2 \rightarrow O + O^-$, (R3K4) $e + O_2(a^1\Delta_g) \rightarrow O + O^-$ and (R15K6) $e + O_2(Ryd) \rightarrow O + O^-$. The cross sections vs. electron energy for these reactions are plotted in Figure 7. In Figure 8, T_e of the model "1000*$k_{O2\text{-}dis}$" is higher than that of the model "P_s+1000*$k_{O2\text{-}dis}$". This can be explained by the fact that the much higher $O_{(s)}$ surface coverage in "1000*$k_{O2\text{-}dis}$" (see Figure 6) produces more

O_2 through atomic oxygen surface recombination. These extra O_2 molecules can facilitate more gas phase O_2 dissociation processes, which reduce the electron energy (and electron temperature), thus there are more low energy electrons lost in the attachment processes in “1000*$k_{O2\text{-}dis}$” and increase its T_e. Indeed, the negative ion density in “1000*$k_{O2\text{-}dis}$” is 1.22×10^{15} m^{-3}, which is a factor of 1.56 larger compared to the value of 7.82×10^{14} m^{-3} in “P_s+1000*$k_{O2\text{-}dis}$”. As I have discussed below, the processes that dominate [e] are ionizations. The above mentioned increase in the gas phase O_2 dissociations reduces the electron energy and thus reduces the ionization processes, which in turn reduces [e]. Therefore [e] of the model “1000*$k_{O2\text{-}dis}$” is smaller than that of the model “P_s+1000*$k_{O2\text{-}dis}$” in Figure 9.

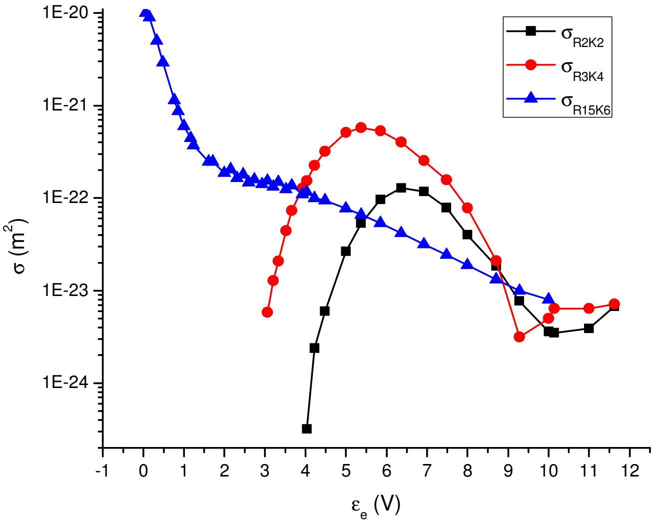

Figure 7 Cross section σ vs. electron energy ε_e plot.

These are plotted for the dominant electron attachment channels in a pure O_2 plasma [14]: (R2K2) e + $O_2 \rightarrow O + O^-$, (R3K4) e + $O_2(a^1\Delta_g) \rightarrow O + O^-$ and (R15K6) e + O_2(Ryd) → O + O^-. σ_{R2K2} is from Ref. [39]; σ_{R3K4} is from Ref. [49] via Ref. [39]; σ_{R3K4} is from Ref. [53].

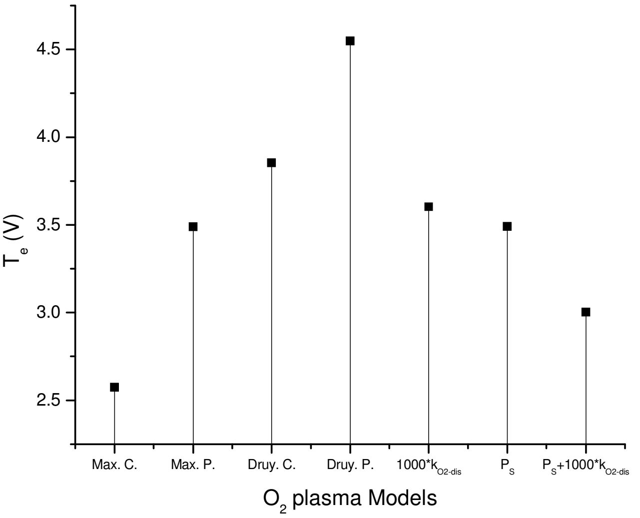

Figure 8 Simulated T_e for pure O_2 plasma under various manufactured conditions.
The electron temperature T_e was simulated under two sets of rate coefficients for O_2, $O_2(a)$, $O_2(b)$ gas phase dissociation reactions listed in Table 12 and three manufactured conditions. The labels of the O_2 plasma models and the test conditions are explained in Figure 5.

The simulated [e] for each of the test models is plotted in Figure 9. If electron attachment was the dominant electron loss channel in the pure O_2 plasma, we would expect for such significant [e] difference between the models "1000*$k_{O2\text{-}dis}$" and "Max. P.", if the lower energy electrons were significantly consumed in the electron attachment processes in the model "1000*$k_{O2\text{-}dis}$", the T_e difference would be much more pronounced than we see in Figure 8. The small difference in T_e between the two models indicates that the main cause of [e] decrease in the model "1000*$k_{O2\text{-}dis}$" compared to "Max. P." is the electron energy loss caused by the factor of 10^3 increase in the O_2 gas phase dissociation rate coefficients, which significantly reduces the electron production from the ionization processes. One might expect the increased electron energy loss to O_2 dissociation would reduce T_e in the model "1000*$k_{O2\text{-}dis}$", but the extra low energy electrons produced by the increased O_2 dissociation reactions are consumed in the electron attachment processes, which further reduces [e] and raises T_e (as discussed above), that's why T_e values of the two models are not far away in Figure 8. With that said, in Figure 9, [e] is significantly smaller for the models "1000*$k_{O2\text{-}dis}$" and "P_s+1000*$k_{O2\text{-}dis}$", which is as expected.

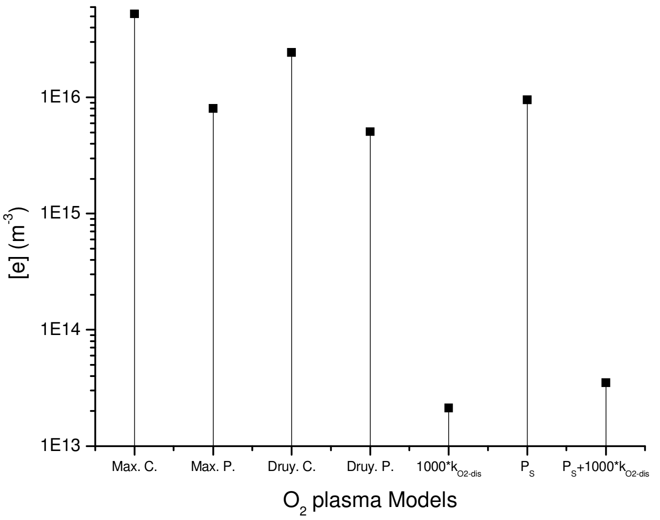

Figure 9 Simulated [e] for pure O_2 plasma under various manufactured conditions.
The electron density [e] was simulated under two sets of rate coefficients for O_2, $O_2(a)$, $O_2(b)$ gas phase dissociation reactions listed in Table 12 and three manufactured conditions. The labels of the O_2 plasma models and the test conditions are explained in Figure 5.

On the other hand, when SF_6 is added to the feed composition, reducing the initial sticking coefficients of atomic O and $O(^1D)$ chemisorptions (R3S2, R4S2) alone as mentioned above won't be enough to see a large increase in [O]. My models' set-up for this test is the same as for simulating Kechkar *et al.*'s work [10], which is listed in Figure 12. In the test version SF_6/O_2 model, I only reduced the initial sticking coefficients of atomic O and $O(^1D)$ chemisorptions, and left the initial sticking coefficients of O_2 and its excited species chemisorptions unchanged as in the pure O_2 plasma model (the initial sticking coefficient of (R41S1) took the value as in a pure SF_6 plasma to prevent it from dominating the surface processes). I used an input power of 88 W for the test version 95% O_2 feed composition SF_6/O_2 plasma model to match $[e] = 10^{15}$ m^{-3} as reported in Kechkar *et al.*'s work (see Table 13). From the test version SF_6/O_2 plasma model, I got $\theta_O = 60.39\%$, $[O] = 1.08 \times 10^{19}$ m^{-3} ; whereas from the pure O_2 plasma model, I got $\theta_O = 86.20\%$, $[O] = 3.38 \times 10^{19}$ m^{-3} (see Table 13). That is, in this test, when 5% SF_6 was added to a pure O_2 plasma's feed composition, the [O] became smaller. The smaller [O] in the test version SF_6/O_2 plasma model is due to two factors: first, the increased [O] due to the reduced O surface loss was in some extent reduced by the gas phase reactions with SF_6 and its child species (compare [O] of the pure O_2 model labelled "P_s" in Figure 5); second, the reduced power in the test version SF_6/O_2 plasma model (88 W for the test version SF_6/O_2 plasma model, 343.605 W for the pure O_2 plasma model) further reduced [O]. When I raised the input power of the test version SF_6/O_2 plasma model to the same value as for the pure O_2 plasma model (343.605 W) while kept its steady state chamber pressure to 100 mTorr, I got θ_O = 28.03%, [O] = 4.80×10^{19} m^{-3}, which is a higher [O] than that of the pure O_2 plasma model.

One notable scenario we see in the above test is that compared to θ_O = 19.4% of the pure O_2 plasma model labelled "P_s" in Figure 6, there is a significant increase in θ_O of the test version SF_6/O_2 plasma model (θ_O = 60.39%), although the initial sticking coefficients / reaction probabilities of the oxygen surface chemical kinetics are the same in the pure O_2 model "P_s" and in the test SF_6/O_2 model. I attribute this to the reduced input power (343.605 W in "P_s" in Figure 6, 88 W in the test SF_6/O_2 model), which reduces the positive ion densities. Due to their large Bohm speeds and unity surface reaction probabilities, despite their small densities compared to the neutrals, the positive ions can influence θ_O [see Eq. (44)], especially when all the neutral species initial sticking coefficients are small, which was the situation I had for the test SF_6/O_2 model. I tested this interpretation by increasing the input power of the test SF_6/O_2 model to the same value as in the O_2 model "P_s" in Figure 6 (343.605 W) and still kept its steady state pressure to 100 mTorr (13.3 Pa), I got [O] = 4.80×10^{19} m^{-3}, θ_O = 28.03%, which are a higher [O] than that of the pure O_2 plasma model for simulating Kechkar *et al.*'s work [10] in section 5.2 (see Table 13) and a θ_O value much closer to that of the O_2 plasma model labelled "P_s" in Figure 6, thus prove my above discussion.

As I have mentioned in section 4.2.2, when SF_6 is added to the feed composition, the gas temperature and surface defects increase, and the initial sticking coefficients of O_2 and its excited species abstractive adsorptions (R9S2–R12S2) have two orders of magnitude increase. Therefore, when small SF_6 feed composition is added to the O_2 feed stock gas, most of the surface coverage is contributed by the abstractive adsorptions of F_2, O_2 and its excited species (F_2^+ and O_2^+ are not considered here due to their small densities compared to F_2 and O_2, and the large initial sticking coefficients of F_2 and O_2 chemisorptions in an SF_6/O_2 plasma), because the atomic O chemisorption channels (R3S2, R4S2) are almost closed. This has been confirmed by my two test versions of the SF_6/O_2 plasma model.

In the first version of the test models, I manually closed the O and O(^{1}D) chemisorption channels (R3S2, R4S2) in my SF_6/O_2 model for simulating Kechkar *et al.*'s work [10] in section 5.2, and I saw at 95% O_2 feed composition, [O] = 9.68×10^{19} m^{-3}, $\theta_O = 71.43\%$, compared to [O] = 8.42×10^{19} m^{-3}, $\theta_O = 71.85\%$ with these channels open as listed in Table 13 (the two models had the same input power of 27 W; the original models had [e] = 1.03×10^{15} m^{-3}, the test model had [e] = 9.64×10^{14} m^{-3}; both models had steady state pressure of 100 mTorr). The two very close θ_O values confirms that when small SF_6 feed composition is added to the O_2 feed stock gas, most of the surface coverage is contributed by the abstractive adsorptions of O_2 and its excited species; I did similar test to prove that θ_O of the pure O_2 plasma is mostly contributed from O and O(^{1}D) chemisorptions, in which I closed O_2 and its excited species chemisorption channels in my pure O_2 model for simulating Kechkar *et al.*'s work [10] in section 5.2. I used the same input power for the test model and the original model and kept the steady state pressure of both models to 100 mTorr. The test model had θ_O = 84.84% and the original model had θ_O = 86.20%, which proves that O and O(^{1}D) chemisorption channels contribute most of the $O_{(s)}$ surface coverage in a pure O_2 plasma. These results show that when SF_6 is added to a pure O_2 plasma's feed composition, the sharp (a factor of 10^2) increase / decrease in the initial sticking coefficients of O_2 and its excited species chemisorptions / O and O(^{1}D) chemisorptions reduces θ_O contributed by the atomic O and O(^{1}D) chemisorptions from about 84.84% to about 0.42% (71.85% − 71.43%), where I assume due to the atomic oxygen's large density and near unity initial sticking coefficient in the pure O_2 plasma, its contribution in surface coverage dominates that of O^+ and O_2^+.

In the second version of the test model, I replaced the abstractive adsorptions of O_2 and its excited species (R9S2–R12S2) with normal dissociative adsorptions (i.e., $O_2 + 2s \rightarrow 2O_{(s)}$) in my SF_6/O_2 model for simulating Kechkar *et al.*'s work [10] in section 5.2. At 95% O_2 feed composition, I matched the test model's simulated [e] to the same value as in the original model, and kept the steady state pressure of both models to 100 mTorr (13.3 Pa). I saw [O] = 6.27×10^{18} m^{-3} (smaller than [O] = 3.38×10^{19} m^{-3} in the pure O_2 plasma model, see Table 13), θ_O = 93.49%, where the smaller [O] compared to the pure O_2 plasma model was due to its reduced input power (92 W in the test model, 343.605 W in the pure O_2 model) in order to match [e] reported in Kechkar *et al.*'s work [10]. When I increased the input power of the test model to the same value as in the pure O_2 model (343.605 W) while kept its steady state chamber pressure to 100 mTorr, I got

$[O] = 4.09 \times 10^{19}$ m^{-3}, $\theta_O = 59.35\%$, which was a small increase in [O] compared to the pure O_2 model. One notable point is that the previous test version SF_6/O_2 model which only reduced O and O(^{1}D) chemisorption initial sticking coefficients and kept O_2 and its excited species chemisorption initial sticking coefficients as they were in the pure O_2 plasma model, got $[O] = 4.80 \times 10^{19}$ m^{-3}, $\theta_O = 28.03\%$ (when the input power was 343.605 W and the steady state pressure was 100 mTorr), which was an even higher [O] than that of the current test model with input power of 343.605 W. This is due to the increased O surface coverage in the current test model, which favoures the O surface recombination and reduces [O]. Comparing to $[O] = 8.42 \times 10^{19}$ m^{-3} obtained from the SF_6/O_2 model for simulating Kechkar *et al.*'s work [10] with the oxygen molecule abstractive chemisorptions turned on, these results confirm that the atomic O produced from the abstractive adsorptions of O_2 and its excited species is also the cause of the large [O] increase, therefore prove that the switch of the main contribution channel of θ_O as discussed above is the reason for the large [O] increase when SF_6 is added to a pure O_2 plasma's feed composition.

I now give a summary of the above discussions. In an SF_6/O_2 plasma, bare surface chemisorptions dictate [O]. When small SF_6 is added to a pure O_2 plasma's feed stock gas, the main contribution channels of $O_{(s)}$ surface coverage switches from O and O(^{1}D) chemisorptions to O_2 and its excited species chemisorptions, which almost closes the former $O_{(s)}$ production channel. In an SF_6/O_2 plasma, the smaller $O_{(s)}$ surface coverage reduces atomic O surface recombination, thus increases [O]. The atomic O produced by the enhanced abstractive adsorptions of the oxygen molecules in the SF_6/O_2 plasma further increases [O]. The overall result of the above two processes gives rise to a large increase in [O]. For the same input power (more precisely, for the same input power coupled to the electrons) and steady state gas pressure, we see a general trend that the smaller θ_O, the larger [O].

5.2 SF_6/O_2 Plasma Model Validation by Kechkar *et al.*'s Experimental Work

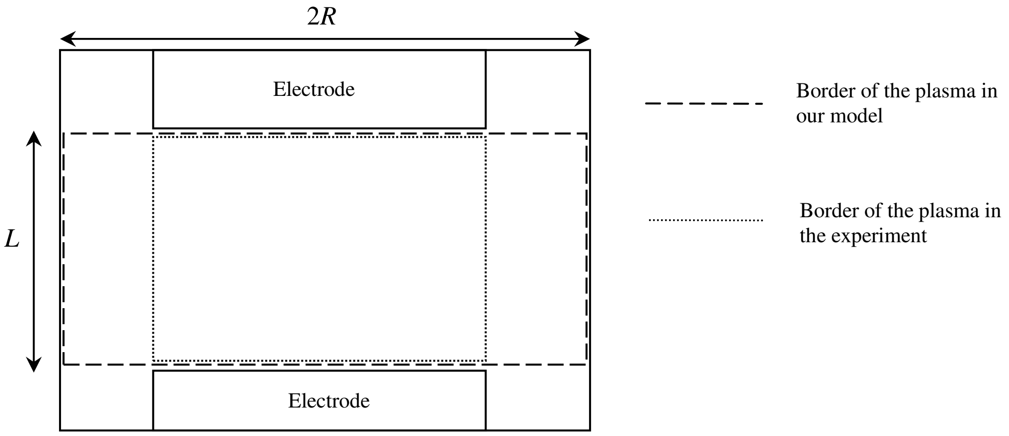

Figure 10 Demonstration of the plasma confinement in our model and Kechkar *et al.'s* experiment [10].

First, let's compare my model's simulation results with a recently published paper by Samir Kechkar *et al.* [10] from our group in the NCPST, DCU. Their work carried out in a cylindrical aluminium capacitively coupled rf discharge source chamber (Oxford instruments Plasmalab System 100). Their chamber dimensions were: chamber radius = 0.38/2 m, chamber length = 0.15 m. The two electrodes where power was coupled into the plasma were 0.045 m apart. The driven electrode was 0.205 m in diameter, the grounded electrode was 0.295 m in diameter. The feedstock gas input rate of their chamber was 50 sccm (for pure O_2 and SF_6/O_2 mixture), and the input power was 100 W. They allowed the throttle position of their chamber's exhaust pump to vary, thus maintained a fixed chamber pressure of 100 mTorr (13.3 Pa). There are three fundamental difficulties my model has to face: First, the electron energy distribution functions (EEDFs) vary with the gas mixture's composition, and can't be simply deemed as Maxwellian or Druyvesteyn [10] (see Figure 11). Second, the exact geometry of the plasma is not clear, it's either confined between the two electrodes [10], or diffuses to some extent to the chamber wall. Third, the chamber's internal geometry is not exactly cylindrical. A question was raised as what chamber dimensions should I use for my model? In my model, I set $R = 0.19$ m, $L = 0.045$ m (see Figure 10). Moreover, this does not reflect the second problem I am facing. My model's results are shown in Table 13.

Comparison of my simulated and Kechkar *et al.*'s experimentally measured [10] [O]s are shown in Figure 12.

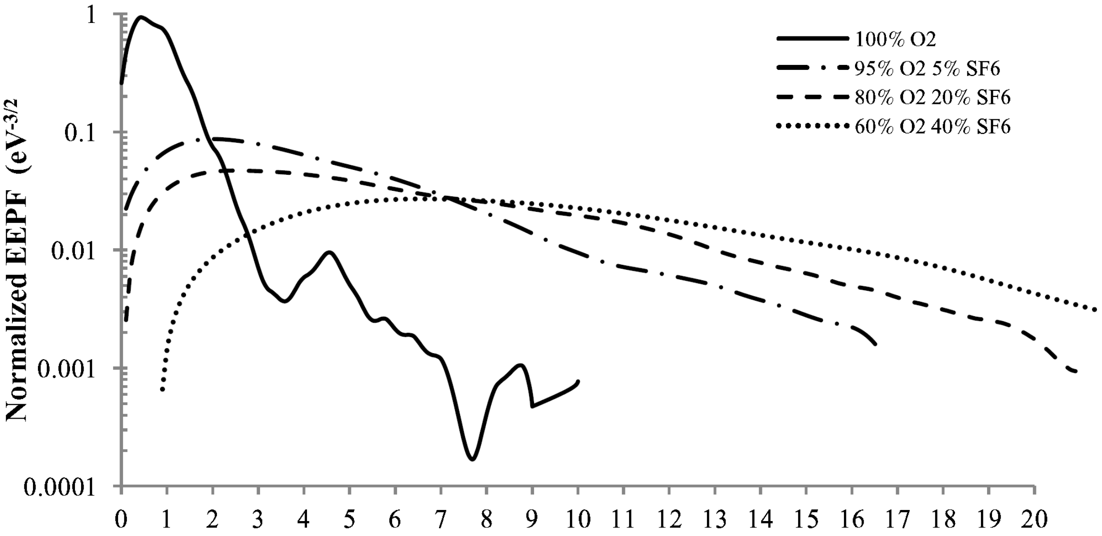

Figure 11 EEPFs for different O_2 to SF_6 feed composition ratios.
The figure shows the normalized electron energy probability functions (EEPFs) for different O_2 to SF_6 feed composition ratios in Kechkar *et al.*'s work [10]. Figure is from Kechkar *et al.*'s work Ref. [10]. The pressure and input power of their experiment was 100 mTorr (13.3 Pa) and 100W.

In Figure 12, the trend of the [O] profile vs. O_2 feed composition well agrees with Kechkar *et al.*'s experimental work [10]. Here, we see a factor of 2.49 increase in [O] when 5% SF_6 is added to the O_2 feed composition in my simulated result. This large increase verifies my proposed chemical kinetics in section 4.2. As mentioned above, one of the difficulties my model has to face is that the EEDF of the plasma in Kechkar *et al.*'s work can not be simply deemed Maxwellian or Druyvesteyn. Here I assume a Maxwellian EEDF for the pure O_2 plasma [14], and a Druyvesteyn EEDF for the pure SF_6 plasma [4]. As SF_6 has great influence on the SF_6/O_2 plasma's electronegativity [10], I assume a Druyvesteyn EEDF for the SF_6/O_2 plasma. Which is notable is the large differences between my simulated and the experimental [O]. This is mainly due to the fact that the experimental results were obtained at the chamber's geometry center, which had the peak value for the neutral density. See Figure 16 for the comparison with the volume averaged [O] calculated for Kechkar *et al.*'s results.

My initial model results showed large differences in terms of [e] (electron density) with respect to the experiment. I believe this is mainly due to the well known fact that the input power coupled into the electron population of a plasma discharge in a

CCP plasma chamber is only a fraction of the total input power. As the techniques for measuring electron density have been well established (Langmuir probe and hairpin probe were used in Kechkar *et al.*'s work [10]), I expect the electron density values reported by Kechkar *et al.* are accurate. Therefore, it makes more sense to generate my results by matching my model's simulated [e] values to that reported in the experiment [see Figure 13 (a)]. One exception for my result is [e] for the pure O_2 plasma. As I have discussed below, the maximum input power of our model is 343.605 W (which gives the same power density as the ideal scenario for the experiment that 100% input power is coupled into the plasma and all the plasma is confined between the electrodes). Because the electron density [e] is proportional to the input power, for the pure O_2 plasma, even this maximum input power gives me an [e] value smaller than (but close to) the experimental value, thus it won't make sense to increase the input power beyond the maximum possible value to match my [e] to that of the experiment. It is worth pointing out that in Table 13, from 95% to 60% O_2 feed composition, we see a decrease in [e] although the input power increases. This is because when more SF_6 is in the feed composition, the plasma becomes more electronegative [10], and the low energy electron loss due to the electron attachment dominates the [e] increase caused by the power increase, thus we see a decrease in [e].

As mentioned above, for the pure O_2 plasma, I assume the plasma in my model extends to most of the chamber's surface, and the plasma in the experiment is assumed to be confined between the two electrodes (see Figure 10). I found with these assumptions my simulated results had better correspondence with the experimental data for the pure O_2 plasma. The important consequence of these assumptions is the maximum power coupled into my model is not 100 W (as in the experiment) any more. In a plasma global model, it is the power density that is being used in the energy balance equation. Thus for the pure O_2 plasma model, to match [e] of the experiment, I equated the power density of the model to that of the experiment, with the above assumptions and assume an ideal condition of 100% power coupled into the plasma, which gives the maximum power for the model:

$$\frac{P}{V_{\text{model}}} = \frac{100}{V_{\text{between electrodes}}}$$

$$\frac{P}{\pi \cdot 0.19^2 \cdot 0.045} = \frac{100}{\pi \cdot 0.1025^2 \cdot 0.045}$$

$$\Rightarrow P = \frac{100 \cdot 0.19^2}{0.1025^2} = 343.6050\,(\mathrm{W}).$$

Furthermore, as I have discussed in section 2.2.1, I assume the gas temperature is 600 K, as suggested by Gudmundsson and Thorsteinsson [14].

Table 13 Compare the SF_6/O_2 plasma simulation with Kechkar *et al.*'s experiment.

This table lists my simulation results compared with the experimental results in Kechkar *et al.*'s work [10] for the SF_6/O_2 plasma. The total input power was 100 W in the experiment. Total feedstock gas flow rate = 50 sccm. The model's steady state chamber pressure was controlled to be constantly 100 mTorr (13.3 Pa) (as in the experiment) by varying the residence time τ_{res}. See Figure 12 for the model's setup. Maxwellian EEDF was assumed for the pure O_2 plasma; Druyvesteyn EEDF was assumed for the SF_6/O_2 plasma.

$\%O_2$	O_2 Flow Rate (sccm)	θ_O (%)	θ_F (%)	θ_{SF5} (%)	Input Power in Our Model (W)	[e] (10^{15} m^{-3})		T_e (V)		[O] (10^{20} m^{-3})		[F] (10^{19} m^{-3})
		Our Model	Our Model	Our Model		Our Model	Kechkar *et al.*	Our Model	Kechkar *et al.*	Our Model	Kechkar *et al.*	Our Model
100	50	86.20	—	—	343.605	8.07	11	3.49	0.8	0.338	1.4	—
95	47.5	71.85	7.78	2.33	27	1.03	1	5.08	3.6	0.842	6.15	2.91
90	45	71.39	7.78	3.10	27.2	0.704	0.7	5.11	4.3	0.762	6.2	3.60
80	40	70.71	7.77	3.77	29.6	0.501	0.5	5.14	5.5	0.681	5.3	4.11
60	30	69.45	7.72	4.53	34.1	0.442	0.44	5.17	7.6	0.564	3.5	4.52
40	20	68.09	7.57	5.43	40.7	0.480	0.48	5.19	7.8	0.420	2.2	4.95

From Table 13, we see θ_O decreases with decreasing O_2 composition in the feedstock gas (this is not always the case, see my discussion in the second paragraph below Figure 18 in section 5.4). Which is notable is that when 5% SF_6 is added to the feed composition, we see a large decrease in θ_O compared to that of the pure O_2 plasma. As discussed in section 5.1, for pure O_2 plasma, θ_O is mainly contributed from O and $O(^1D)$ chemisorptions; for SF_6/O_2 plasma, θ_O is mainly contributed from the abstractive adsorptions of O_2 and its excited species. I have shown in section 5.1 that the difference in θ_O in the pure O_2 and in the SF_6/O_2 plasmas is due to the switch of the main contributor of the chemisorbed $O_{(s)}$. From Table 13, it seems like θ_F decreases with increasing SF_6 feed composition, however, the sum of θ_F and θ_{SF5} increases from 10.11% (at 95% O_2 feed) to 13% (at 40% O_2 feed), which suggests competition between SF_5 and F for the surface sites. Recall that chemisorbed O can only be removed from the surface by directional ion bombardment [6] or by O surface recombinations [8] (see section 2.1), thus my model doesn't have direct surface reactions between SF_6 and O_2's neutral child species. Because the surface is not fully covered in my model's results, both O and F will have empty surface sites available when they reach the chamber wall, therefore there's no sign of competition for surface sites between O and F. On the other hand, θ_{SF4} increases from 0.04% at 95% O_2 feed composition to 0.16% at 40% O_2 feed composition, θ_{SF3} is well below 0.1% for all O_2 feed compositions, thus they have little influence on the surface processes. In any feed composition for the SF_6/O_2 plasma, we see around 20% empty surface sites, as I have discussed in section 4.2.2, these surface sites are likely either fluorinated or oxidised, which can not be described explicitly by my model.

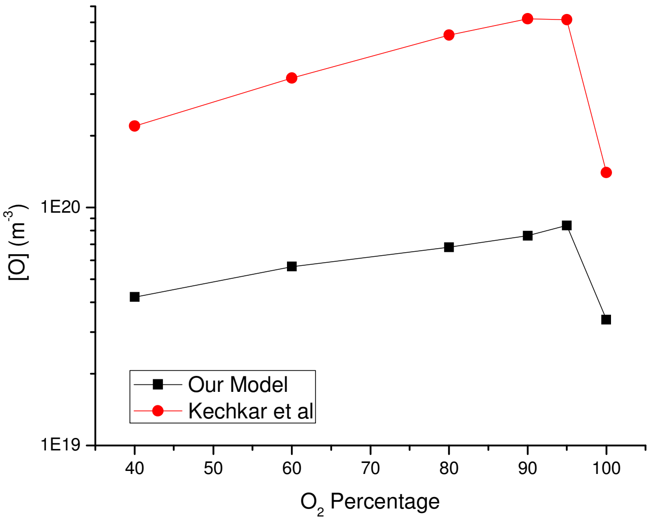

Figure 12 [O] vs. O_2 feed composition in the SF_6/O_2 plasma. ■ my simulated results, ● Kechkar *et al.*'s [10] experimental results. The data is listed in Table 13. The simulated results were obtained by matching [e] to that reported in Kechkar *et al.*'s work. All simulated values were obtained in steady state. Simulated chamber dimensions: R = 0.19 m, L = 0.045 m; total SF_6/O_2 feedstock gas input rate = 50 sccm; the gas temperature T_g = 600 K was assumed constant for the model; chamber pressure at steady state = 100 mTorr (13.3 Pa). Maxwellian EEDF was assumed for the pure O_2 plasma; Druyvesteyn EEDF was assumed for the SF_6/O_2 plasma. Large differences present because the experimental results were obtained at the chamber's geometry centre, which had the peak value for the neutral density. See Figure 16 for comparison with the volume averaged [O] calculated for Kechkar *et al.*'s results.

Figure 13 (b) shows the comparison of our simulated results and Kechkar *et al.*'s [10] experimental results for the electron temperature T_e. There're large differences between the two results, I attribute the differences to the irregular EEDFs as seen in

Kechkar *et al.*'s experiment (see Figure 11). Nevertheless, the trend of our simulated T_e's variations agree with Kechkar *et al.*'s work.

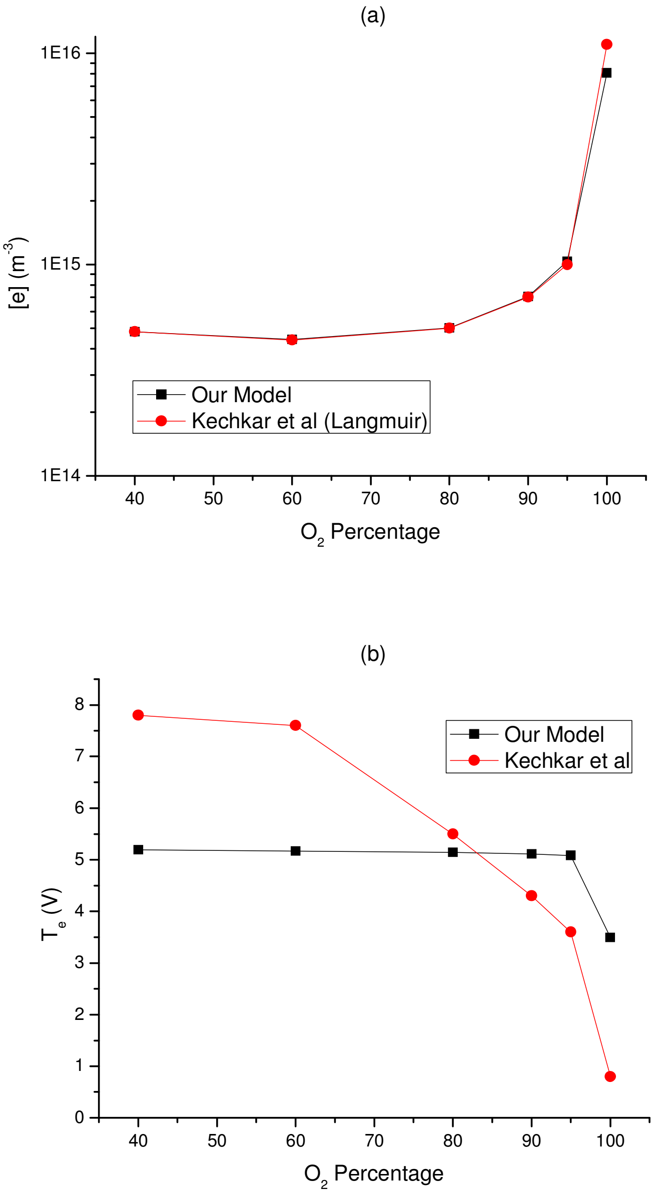

Figure 13 [e] [figure (a)] and T_e [figure (b)] vs. O_2 feed composition in the SF_6/O_2 plasma. ■ my simulated results, ● Kechkar *et al.*'s [10] experimental results, where [e] was obtained by Langmuir probe. I matched our [e] values to that of Kechkar *et al.*'s work. The data is listed in Table 13. All simulated values were obtained in steady state. Simulated chamber dimensions: $R = 0.19$ m, $L = 0.045$ m; total SF_6/O_2 feedstock gas input rate = 50 sccm; the gas temperature $T_g = 600$ K was assumed constant for the model; chamber pressure at steady state = 100 mTorr (13.3 Pa). Maxwellian EEDF was assumed for the pure O_2 plasma; Druyvesteyn EEDF was assumed for the SF_6/O_2 plasma.

Figure 14 shows my simulated [F] vs. O_2 feed composition under Kechkar *et al.*'s experiment conditions, which are not reported in Kechkar *et al.*'s work [10]. In Figure 14 we see an increasing [F] with the increasing SF_6 feed composition, which agrees with experimental works Refs. [12], [13].

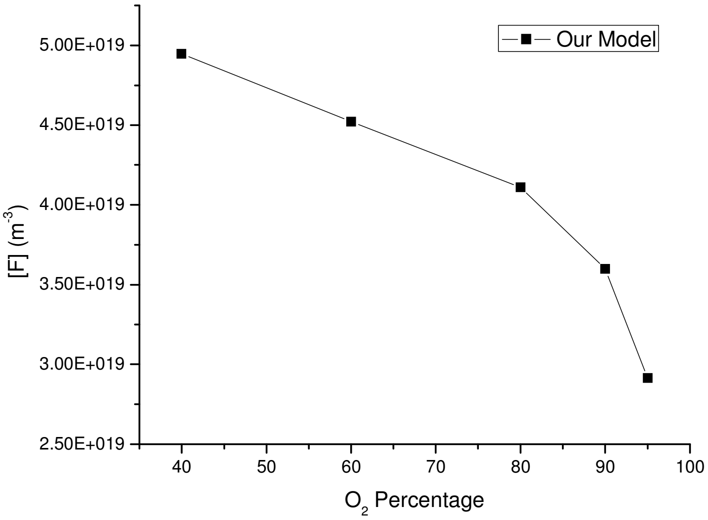

Figure 14 Simulated [F] vs. O_2 feed composition in the SF_6/O_2 plasma.

The result was not reported by Kechkar *et al.* [10]. The data is listed in Table 13. All simulated values were obtained in steady state. Simulated chamber dimensions: R = 0.19 m, L = 0.045 m; total SF_6/O_2 feedstock gas input rate = 50 sccm; the gas temperature T_g = 600 K was assumed constant for the model; chamber pressure at steady state = 100 mTorr (13.3 Pa). Druyvesteyn EEDF was assumed for the SF_6/O_2 plasma.

5.3 The Volume Averaged Neutral Density vs. the Peak Neutral Density

As we can see in Table 13, my simulated atomic oxygen densities have large differences with respect to Kechkar *et al.*'s [10] experimental results. An important point is that a plasma global model is a 0-dimension model, which means its outputs are all volume averaged quantities. In a plasma global model, one assumes the background neutral gas has uniform density across the cylindrical chamber. However, this is far from accurate. In this work, to explain the large differences in terms of [O] between my simulated results and Kechkar *et al.*'s experimental results, I use a crude method proposed by Lieberman and Lichtenberg [1] to calculate the peak to volume averaged neutral density ratio (the value obtained at the cylindrical chamber's geometry centre over the value obtained by averaging over the chamber's volume). In this section, I show that the experimental neutral density obtained at the cylindrical chamber's geometry center is much larger than the volume averaged value.

Lieberman and Lichtenberg [1] showed that for a cylindrical geometry, when azimuthal symmetry is assumed, the neutral density in cylindrical coordinates can be written as:

$$n(r,z) = n_0 \mathrm{J}_0(\chi_{01} r / R) \cos(\pi \cdot z / L)\,, \tag{88}$$

where L is the distance between the two electrodes of the CCP chamber, R is the chamber radius; $n(r, z)$ is the neutral density at location (r, z) in cylindrical coordinates, r is the position along the radius of the chamber, which ranges from 0 to R, z is the position along the distance between the two electrodes, which ranges from $-L/2$ to $L/2$; n_0 is the neutral density at the geometry center of the cylindrical chamber; J_0 is the zero-order Bessel function, $\chi_{01} \approx 2.405$ is the first zero of J_0. A plot of $n(r, z)/n_0$ is shown in Figure 15 for the chamber in Kechkar *et al.*'s [10] work. From Eq. (88), I calculated the neutral density obtained at the cylindrical chamber's geometry center to the volume averaged neutral density ratio, which is

$$\frac{n_{\mathrm{avg}}}{n_0} = 0.275\,, \tag{89}$$

where n_{avg} is the volume averaged neutral density.

Although the neutral density ratio of the peak value at the chamber's geometry center to the volume averaged value in Eq. (89) is very crude (e.g., the density profile along r may not be simply described by a zero-order Bessel function, and the dissociation rate of the neutral gas may not be uniform across the chamber), it gives us a useful approximation. By using the ratio, the volume averaged [O]s of Kechkar *et al.*'s [10] work are listed in Table 14, and are ploted in Figure 16. From Table 14 we can see that the largest difference between the experimental and my simulated values in [O] is by a factor of 2.24 when there's 90% O_2 in the SF_6/O_2 plasma feedstock gas; the minimum difference is by a factor of 1.14 when there's 100% O_2 in the feed composition, which are quite reasonable for a global model.

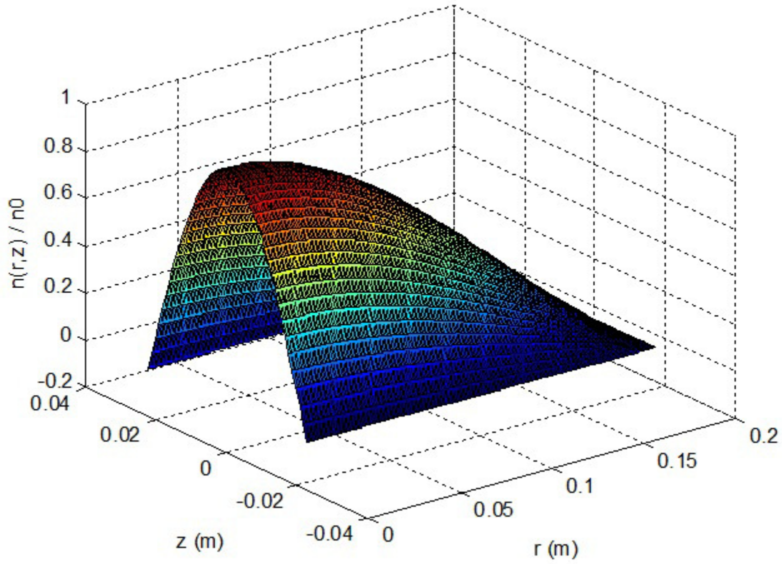

Figure 15 $n(r, z)/n_0$ plot by using Eq. (88) for the CCP plasma chamber in Kechkar *et al.*'s [10] work.

Table 14 [O]s of the SF_6/O_2 plasma simulation and Kechkar *et al.*'s experiment (volume averaged).

This table lists my simulated [O]s compared with the volume averaged [O]s calculated for Kechkar *et al.*'s results [10] by using the peak to volume averaged neutral density ratio of Eq. (89). The total input power was 100 W in the experiment. See Figure 12 for the model's setup. The model's steady state chamber pressure was controlled to be constantly 100 mTorr (13.3 Pa) (as in the experiment) by varying the residence time τ_{res}. Maxwellian EEDF was assumed for the pure O_2 plasma; Druyvesteyn EEDF was assumed for the SF_6/O_2 plasma.

%O_2	O_2 Flow Rate (sccm)	SF_6 Flow Rate (sccm)	[O] (10^{20} m^{-3})		Difference Factor (volume averaged [O] of Kechkar *et al.*'s work / [O] of Our Model)
			Our Model	Kechkar *et al.* (volume averaged)	
100	50	0	0.338	0.3850	1.14
95	47.5	2.5	0.842	1.69	2.01
90	45	5	0.762	1.71	2.24
80	40	10	0.681	1.46	2.14
60	30	20	0.564	0.963	1.71
40	20	30	0.420	0.605	1.44

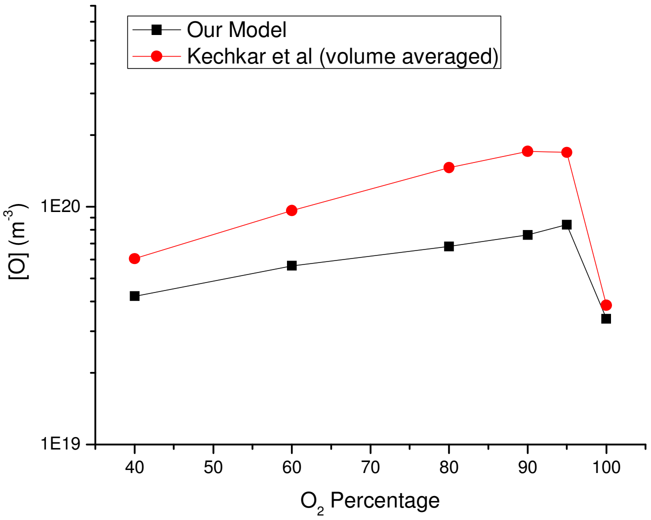

Figure 16 [O] vs. O_2 feed composition in the SF_6/O_2 plasma.

■ my simulated results, ● the volume averaged results calculated for Kechkar *et al.*'s experimental results from Ref. [10]. The data is listed in Table 14. See Figure 12 for the simulation and experiment conditions.

5.3.1 Possible Reason for the Differences in [O] between My Model and Kechkar *et al.*'s Experiment

Although the differences between my model's simulated [O]s and the volume averaged [O]s of Kechkar *et al.*'s experiment are in an acceptable range for a plasma global model. One valid question can still be raised as why with the more sophisticated surface chemical kinetics implemented in my SF_6/O_2 plasma model, there're still differneces of factors ranging from 1.44 to 2.24 in [O] (Table 14) between my model and the experiment (I'm only concerned about non-zero SF_6 feed compositions)? During the study of increasing the O_2 gas phase dissociation rate coefficients in section 5.1, I found a possible explanation for this scenario, that the power coupled into the plasma in the experiment was much higher than that in my model.

In my model, in the transition from pure O_2 plasma to SF_6/O_2 plasma (5% SF_6 in the feed composition), the electron temperature increases from 3.490 V to 5.084 V. According to Figure 4, the rate coefficient of the O_2 gas phase dissociation reaction R7K2 increases from 8.942×10^{-16} m^3s^{-1} (Maxwellian EEDF Ref. [43]) to 1.829 ×

10^{-15} m^3s^{-1} (Druyvesteyn EEDF Ref. [43]), which is a factor of 2.05 increase; in the experiment, the electron temperature increases from 0.8 V to 3.6 V, the rate coefficient of reaction R7K2 increases from 1.808 × 10^{-18} m^3s^{-1} (Maxwellian EEDF Ref. [43]) to 1.129 × 10^{-15} m^3s^{-1} (Druyvesteyn EEDF Ref. [43]), which is a factor of 624.17 increase. Of course, the EEDF of the plasma in the experiment is quite irregular (Figure 11), thus I don't expect such a large increase in the experiment, nevertheless, it shows that the rate coefficients increase of the O_2 gas phase dissociation reactions listed in Table 12 in the experiment is far more significant than what I have implemented in my model. In my test for 5% SF_6 in the SF_6/O_2 plasma feed composition, to reflect this large increase, I manually multiplied the rate coefficients of the reactions listed in Table 12 by a modest factor of 10. As I have discussed in section 5.1 (see Figure 9), the increase of the O_2 gas phase dissociation reaction rate coefficients won't increase [O] directly, but it decreases [e]. To match [e] reported by the experiment, I had to increase the input power of my model from 27 W to 210 W, and I saw [O] increased from 8.42 × 10^{19} m^{-3} to 1.85 × 10^{20} m^{-3}, which is much closer to the volume averaged [O] of the experiment 1.69 × 10^{20} m^{-3} (Table 14). This test indicates that due to the irregular EEDF in the experiment, in the transition from pure O_2 plasma to SF_6/O_2 plasma, the O_2 gas phase dissociation rate coefficients in the experiment have much higher increase than that in my model, which significantly decreases [e]. Thus to have the same [e] as in my model, the power coupled into the SF_6/O_2 plasma in the experiment must be significantly higher than the value I use in my model, which explains why the volume averaged [O]s of Kechkar *et al.*'s experiment have factors ranging from 1.44 to 2.24 (Table 14) higher than that of my model's simulation results.

Another important factor may cause the [O] differences between my results and the experiment is that in my model, I use the volume of almost the whole plasma chamber as the volume of the plasma (see Figure 10), whereas in Kechkar *et al.*'s work, the volume of the plasma was not so clearly defined, which was more likely being confined between the two electrodes (as we have seen for the pure O_2 plasma model's results in Table 14), thus had no chamber wall along the radial direction. In the next section, section 5.4, we will see that when the plasma confinement is better agreed with my model, the experimentally measured [F]s have better correspondence to my simulated results.

5.4 SF_6/O_2 Plasma Model Validation by Pessoa *et al.*'s Experimental Work

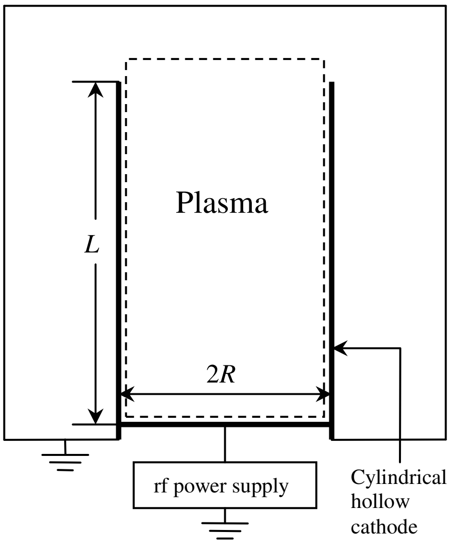

Figure 17 The radio-frequency (rf) self-biased hollow cathode reactive ion etching (HCRIE) reactor in Pessoa *et al.*'s work [13].

To validate my model's simulation result for [F] and to test the model for the full spectrum of O_2 feed composition in the SF_6/O_2 plasma, I also compared my model's results with Pessoa *et al.*'s work [13]. Pessoa *et al.* measured [F] with respect to the O_2 composition in the SF_6/O_2 plasma's feedstock gas for a hollow cathode reactive ion etching (HCRIE) reactor. A radio-frequency (rf) self-biased HCRIE reactor (Figure 17) converts a conventional plane geometry to a hollow configuration, which essentially has a reversed “chamber radius to distance between electrodes ratio” compared to a CCP plasma chamber, which significantly enhances the ionization efficiency at lower pressures [13]. The chamber wall material in the experiment was aluminium, and the chamber dimensions were $R = 0.1/2$ m, $L = 0.147$ m. In the experiment, the total SF_6/O_2 feedstock gas input rate was 10 sccm and kept constant. The total input power was 50 W, and the pressure of the chamber was allowed to vary between 18 to 20.2 mTorr. In my model, the gas temperature $T_g = 600$ K is assumed constant; the chamber pressure at steady state is 20 mTorr (2.66 Pa) and is kept constant for all tests. As explained in section 5.2, Maxwellian EEDF is assumed for the pure O_2 plasma; Druyvesteyn EEDF is assumed for the pure SF_6 plasma and the SF_6/O_2 plasma.

The comparison between my simulated results and the experimental results reported by Pessoa *et al.* [13] is shown in Table 15. I assume the power coupled into the electron population of the plasma is again only a fraction of the total input power, thus I used the same strategy for the simulation, in which I matched my simulated [e]s to the values reported in Pessoa *et al.*'s work [13] (see Figure 19). Similar to my comparison with Kechkar *et al.*'s [10] work, the problems my model faced before still linger now (see the first paragraph of section 5.2), but the second and third problems have been mitigated significantly, that is, the plasma's confinement is better defined in Pessoa *et al.*'s chamber and the internal geometry of their chamber is much closer to a cylinder (see Figure 17). We see large differences in T_e in Figure 20, I attribute the reason to the fact that the EEDFs in Pessoa *et al.*'s work can not be deemed as Maxwellian or Druyvesteyn, just as we have seen in Kechkar *et al.*'s work [10] (Figure 11). We also see large differences in [F]. As I have pointed out in section 5.3, this is mainly due to the fact that the experimental results were obtained at the chamber's geometry centre, which had the peak value for the neutral density.

Table 15 Compare the SF_6/O_2 plasma simulation with Pessoa *et al.*'s experiment.

This table lists my simulation results compared with the experimental results in Pessoa *et al.*'s work [13]. In the experiment, the total input power was 50 W, and the pressure of the chamber was allowed to vary between 18 to 20.2 mTorr. The total feed rate was 10 sccm. See Figure 18 for the model's setup. The model's steady state chamber pressure was controlled to be constantly 20 mTorr (2.66 Pa) by varying the residence time τ_{res}. Maxwellian EEDF was assumed for the pure O_2 plasma; Druyvesteyn EEDF was assumed for the pure SF_6 plasma and the SF_6/O_2 plasma.

$\%O_2$	O_2 Flow Rate (sccm)	θ_O (%)	θ_F (%)	θ_{SF5} (%)	Input Power of Our Model (W)	[e] (10^{15} m^{-3})		T_e (V)		[F] (10^{19} m^{-3})		[O] (10^{19} m^{-3})
		Our Model	Our Model	Our Model		Our Model	Pessoa *et al.*	Our Model	Pessoa *et al.*	Our Model	Pessoa *et al.*	Our Model
100	10	86.93	—	—	15.1	7.41	7.4	3.091	8.1	—	—	0.566
90	9	64.47	0.897	3.14	31.4	10.31	10	4.842	6.6	1.36	4.5	13.83
80	8	68.55	1.33	3.38	20.1	6.04	6	5.004	7.8	3.14	8.2	10.47
60	6	68.66	1.62	4.65	14.2	4.21	4.2	5.135	8.9	4.84	14.8	7.20
50	5	67.76	1.64	5.41	13.4	4.04	4	5.152	9.45	5.39	16.6	6.06
40	4	66.56	1.62	6.31	13.1	4.02	4	5.164	9.3	5.90	18.25	4.95
30	3	65.80	1.53	7.39	12.32	3.70	3.7	5.188	9	6.22	17.6	3.61
20	2	64.70	1.38	8.83	11.9	3.41	3.4	5.213	9.3	6.39	15.5	2.31
10	1	61.56	1.24	11.10	12.5	3.41	3.4	5.228	10.3	6.57	12.1	1.11
0	0	—	3.38	67.34	14.7	3.02	3	5.345	12.8	0.90	8.5	—

Table 16 [F]s of the SF_6/O_2 plasma simulation and Pessoa *et al.*'s experiment (volume averaged).

This table lists the simulated [F] compared with the volume averaged results calculated for Pessoa *et al.*'s experimental results [13]. In the experiment, the total input power was 50 W, and the pressure of the chamber was allowed to vary between 18 to 20.2 mTorr. The total feed rate was 10 sccm. See Figure 18 for the model's setup. The model's steady state chamber pressure was controlled to be constantly 20 mTorr (2.66 Pa) by varying the residence time τ_{res}. Maxwellian EEDF was assumed for the pure O_2 plasma; Druyvesteyn EEDF was assumed for the pure SF_6 plasma and the SF_6/O_2 plasma.

$\%O_2$	O_2 Flow Rate (sccm)	SF_6 Flow Rate (sccm)	[F] (10^{19} m^{-3})		Difference Factor (Volume averaged [F] of Pessoa *et al.* / [F] in Our Model)
			Our Model	Pessoa *et al.* (volume averaged)	
90	9	1	1.36	1.24	0.91
80	8	2	3.14	2.26	0.72
60	6	4	4.84	4.07	0.84
50	5	5	5.39	4.57	0.85
40	4	6	5.90	5.02	0.85
30	3	7	6.22	4.84	0.78
20	2	8	6.39	4.26	0.67
10	1	9	6.57	3.33	0.51
0	0	10	0.90	2.34	2.6

My [F] values compared with the volume averaged values calculated for Pessoa *et al.*'s results are listed in Table 16, and are plotted in Figure 18. The largest difference between the two results in [F] appears at 100% SF_6 in the feed composition, where a factor of 2.6 in difference presents; and the minimum difference is by a factor of 0.91 when there's 90% O_2 in the feed composition. Here we see improved results in terms of difference factors in Table 16 than that in Table 14 for the SF_6/O_2 mixtures (when neither SF_6 nor O_2 has zero composition in the feedstock gas). I think this is due to the fact that the plasma's volume was better defined in Pessoa *et al.*'s work [13] (Figure 17) compared to Kechkar *et al.*'s work [10] (Figure 10). In Pessoa *et al.*'s work, the plasma was approximately occupying the whole chamber, which is the same condition as in my model. In Kechkar *et al.*'s work, the volume of the plasma was not so clearly defined, which was more likely being confined between the two electrodes (as we have seen for the pure O_2 plasma model's results in Table 14), thus had no chamber wall along the radial direction. As we have seen in section 5.1 that at the same input power and pressure, the atomic oxygen and atomic fluorine's densities are dictated by the surface conditions, therefore as the surface area in Pessoa *et al.*'s work is better agreed with my model, their atomic oxygen and atomic fluorine's densities should be better agreed with my model's results too.

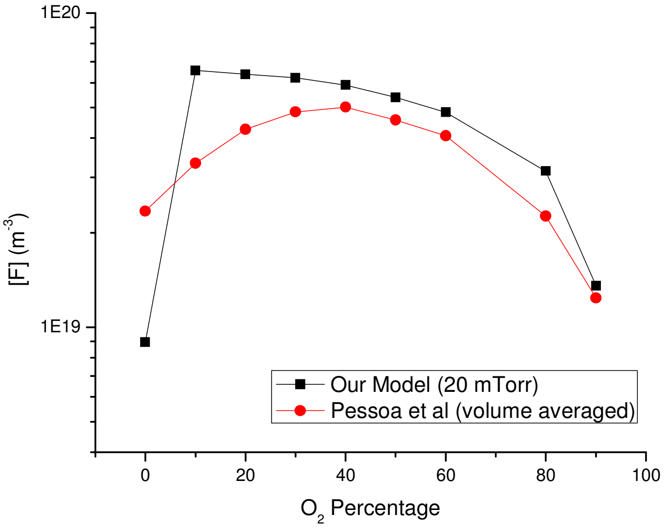

Figure 18 [F] vs. O_2 feed composition in the SF_6/O_2 plasma. ■ my simulated results, ● volume averaged results calculated for Pessoa *et al.*'s [10] experimental results. The data is listed in Table 16. In the experiment, the total input power was 50 W, and the pressure of the chamber was allowed to vary between 18 to 20.2 mTorr. The simulated results were obtained by matching [e] to that reported in Pessoa *et al.*'s work. All simulated values were obtained in steady state. Simulated chamber dimensions: $R = 0.1/2$ m, $L = 0.147$ m; total SF_6/O_2 feedstock gas input rate = 10 sccm; the gas temperature $T_g = 600$ K was assumed constant for the model; chamber pressure at steady state = 20 mTorr (2.66 Pa) was kept constant for all tests. Maxwellian EEDF was assumed for the pure O_2 plasma; Druyvesteyn EEDF was assumed for the pure SF_6 plasma and the SF_6/O_2 plasma.

In Figure 18, for the O_2 feed composition between 10% and 40%, we see a different trend of [F] variation between my results and the experimental results. This is due to the fact that I use fixed initial sticking coefficients for the F and F_2 surface chemisorptions (R1S1 and R41S1) for all the non-zero O_2 feed composition. Therefore the profile of [F] vs. O_2 feed composition in my model is similar to that of [O], but is reversed with respect to the O_2 feed composition, i.e., we see a sharp increase in [F] when a small O_2 feed composition is added to the pure SF_6 plasma's feedstock gas. The profile of [F] obtained from the experiment indicates that there's a gradual change in the initial sticking coefficients of F and F_2's surface adsorptions for the O_2 feed composition between 10% and 40%, as oppose to a sharp 100 times decrease/increase as I implemented in my model. From Figure 18 we can see that the initial sticking coefficients of F and F_2's surface adsorptions gradually change with increasing O_2 feed composition, they reach my proposed values at 40% O_2 feed composition and remain constant for higher O_2 feed compositions.

One notable scenario we see in Table 15 is that θ_O at 90% through 60% O_2 feed composition is increasing (θ_O = 64.47% at 90% O_2, = 68.55 at 80% O_2, = 68.66 at 60% O_2), which is against my interpretation that the smaller O_2 feed composition, the smaller θ_O (see section 5.2 below Table 13). This is due to the fact that the sharply decreased input power (31.4 W at 90% O_2 feed, 20.1 W at 80% O_2 feed, 14.2 W at 60% O_2 feed) makes the positive ion densities smaller, thus at the surface, there are less positive ions competing with neutral species for adsorption surface sites, and we see an increase in the surface coverage for $O_{(s)}$. I tested the SF_6/O_2 model by applying the 90% O_2 model's input power (31.4 W) to the 80% O_2 model, and applying the 80% O_2 model's input power (20.1 W) to the 60% O_2 model while kept all the models' steady state pressure to 20 mTorr (2.66 Pa). For the 80% O_2 test model, I got θ_O = 63.31%, [O] = 1.30×10^{20} m^{-3}, compared to θ_O = 64.47% and [O] = 1.38×10^{20} m^{-3} from the original 90% O_2 model. For the 60% O_2 test model, I got θ_O = 65.39%, [O] = 8.77×10^{19} m^{-3}, compared to θ_O = 68.55%, [O] = 1.05×10^{20} m^{-3} from the original 80% O_2 model. I.e., both θ_O and [O] were smaller for the test models, which was as expected. Same to my comparison with Kechkar *et al.*'s work [10], we see increase in the sum of θ_F and θ_{SF5} with decreasing O_2 feed composition, which is as expected. With that said, the trend of the surface coverage variation is essentially the same as we see in my simulation for Kechkar *et al.*'s work [10]. We see strong competition between F and SF_5 for surface sites, and there's no sign of competition between O and F on the surface due to the lack of neutral SF_6-O_2 surface cross-reactions (see section 5.2 below Table 13). Recall that chemisorbed O can only be removed from the surface by directional ion bombardment [6] or by O surface recombinations [8] (see section 2.1).

My simulated [O] vs. O_2 feed composition is listed in Table 15, and plotted in Figure 21, which was not reported in Pessoa *et al.*'s work [13]. Here we see a much larger increase in [O] when SF_6 is added to the pure O_2 plasma's feed composition compared to that observed from my model for simulating Kechkar *et al.*'s work [10]. This is owning to the fact that in order to match the [e] reported in Pessoa *et al.*'s work for the pure O_2 plasma, I used a much smaller fraction of the total input power than I did in simulating Kechkar *et al.*'s work. In Kechkar *et al.*'s work, [e] measured at 100% O_2 feed

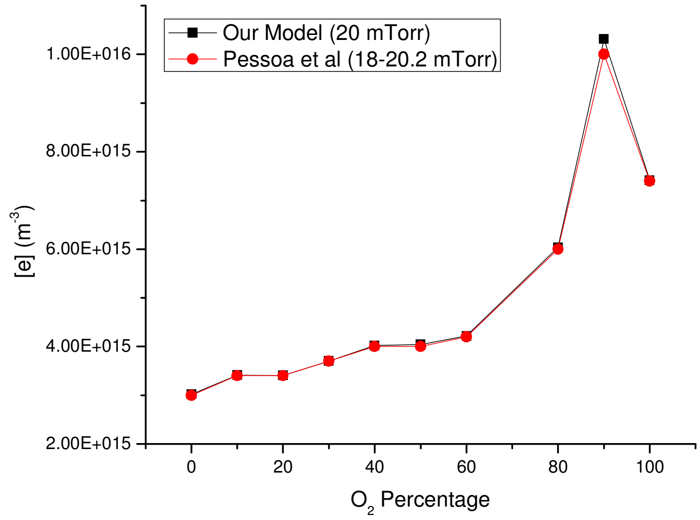

Figure 19 [e] vs. O_2 feed composition in the SF_6/O_2 plasma.

I assume the power coupled into the plasma is only a fraction of the total input power, therefore I matched my simulated [e] to the values reported in Pessoa *et al.*'s work [13]. See Figure 18 for the model's setup.

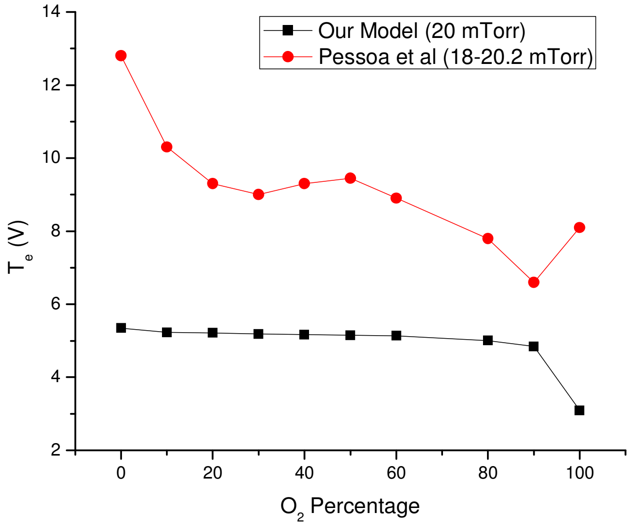

Figure 20 T_e vs. O_2 feed composition in the SF_6/O_2 plasma.

■ my simulated results, ● Pessoa *et al.*'s [13] experimental results. Large differences present due to the irregular EEDFs in an SF_6/O_2 plasma as reported in Kechkar *et al.*'s [10] work (Figure 11). See Figure 18 for the model's setup.

composition is much larger than [e] measured at 90% O_2 feed composition [Figure 13 (a)]; however in Pessoa *et al.*'s work, [e] measured at 100% O_2 feed composition is smaller than [e] measured at 90% O_2 feed composition (Figure 19). To match [e] at

100% O_2 feed composition of Pessoa *et al.*'s work, I had to use a much smaller fraction of the total input power, which led to a much smaller [O] in the pure O_2 plasma.

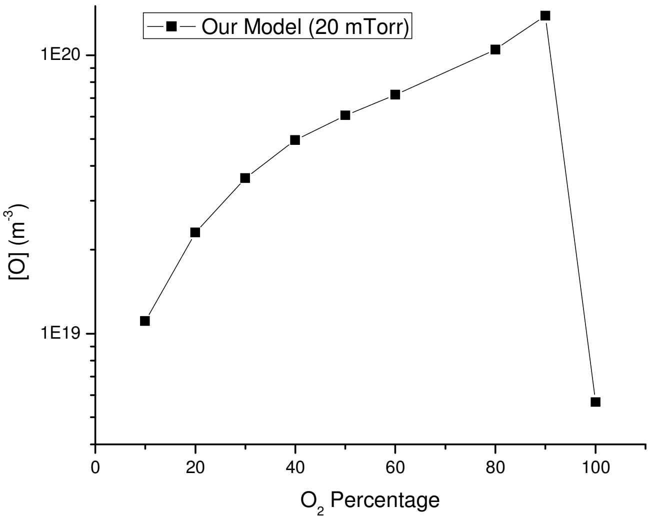

Figure 21 Simulated [O] vs. O_2 feed composition in the SF_6/O_2 plasma, which is not reported in Pessoa *et al.*'s work [13]. The data is listed in Table 15. The simulated results were obtained by matching [e] to that reported in Pessoa *et al.*'s work. All simulated values were obtained in steady state. Simulated chamber dimensions: R = 0.1/2 m, L = 0.147 m; total SF_6/O_2 feedstock gas input rate = 10 sccm; the gas temperature T_g = 600 K was assumed constant for the model; chamber pressure at steady state = 20 mTorr (2.66 Pa). Maxwellian EEDF was assumed for the pure O_2 plasma; Druyvesteyn EEDF was assumed for the SF_6/O_2 plasma.

5.5 Conclusion

In this chapter, I developed an SF_6/O_2 plasma global model with heterogeneous surface model. By validating the model with two experimental works (Kechkar *et al.* [10], sections 5.2 and 5.3; and Pessoa *et al.* [13] section 5.4), I have shown that as an important tool for plasma study, plasma global models still have their places when dealing with plasmas of fluorine containing gas and O_2 mixtures.

I proposed the surface chemical kinetics that govern the several times increase in atomic oxygen density when small SF_6 (e.g. 5% in the feed composition) is added to a pure O_2 plasma's feedstock gas (section 4.2). I found the chemisorptions of oxygen and fluorine's atomic and diatomic species almost dictate the profile of [O] and [F] with respect to the O_2 feed composition. I had three main findings regarding this scenario (section 5.1): (1) The reason for the above mentioned several times increase in [O] is due to a sharp decrease (a factor of 10^2 in my model) in the initial sticking coefficients of O and $O(^1D)$ chamber wall chemisorptions, plus a sharp increase (a factor of 10^2 in my model) in the initial sticking coefficients of O_2 and its excited species chamber wall chemisorptions when SF_6 is added to the pure O_2 plasma's feedstock gas, which effectively switches the main contribution channels of $O_{(s)}$ surface coverage from O and $O(^1D)$ chemisorptions (as in the pure O_2 plasma) to O_2 and its excited species chemisorptions (as in the SF_6/O_2 plasma). In an SF_6/O_2 plasma, comparing to a pure O_2 plasma, the smaller $O_{(s)}$ surface coverage reduces atomic O surface recombination, thus increases [O]. The atomic O produced by the enhanced abstractive adsorptions of the oxygen molecules in the SF_6/O_2 plasma further increases [O]. (2) The increase of O_2's gas-phase dissociation rate coefficient is not the reason for the above mentioned large increase in [O]. (3) The main surface loss channel of the atomic oxygen in O_2 and SF_6/O_2 plasmas is the O surface recombination.

As my models use the macroscopic initial sticking coefficients, the underlying reasons for the above mentioned initial sticking coefficient variations can not be revealed by my models. The most common explanation for the decrease in the initial sticking coefficients of O and $O(^1D)$'s chamber wall chemisorptions is that the surface sites that favourable to O and $O(^1D)$ chemisorptions are either occupied by chemisorbed $F_{(s)}/SF_{5(s)}$ or being fluorinated [3], [10] (section 4.2.2). The fluoro-sulfur films (section 4.2.1) might have impact on the O and $O(^1D)$ initial sticking coefficients too. The reason for the increased O_2 and its excited species abstractive adsorptions is likely due to the surface defects introduced by the fluorination/oxidation processes or the fluoro-sulfur films generated by the SF_6 plasma surface processes. The gas temperature rise as reported in Kechkar *et al.*'s work [10] might play a role here too. (section 4.2.2)

I simulated the density variations of the two most important species in an SF_6/O_2 plasma: atomic O and atomic F, as well as the above mentioned large [O] increase scenario (sections 5.2 to 5.4). When taking the volume averaged [O] and [F] into account (section 5.3), the largest difference in [O] between my simulation and Kechkar *et al.*'s [10] experiment is by a factor of 2.24 (volume averaged [O] of Kechkar *et al.*'s work / [O] of my model) when there's 90% O_2 in the feed composition; and the minimum difference is by a factor of 1.14 when there's 100% O_2 in the feed composition (section 5.3). The largest difference in [F] between my simulation and Pessoa *et al.*'s [13] experiment is by a factor of 2.6 (volume averaged [F] of Pessoa *et al.* / [F] in my model) when there's 100% SF_6 in the feed composition; and the minimum difference is by a factor of 0.91 when there's 90% O_2 in the feed composition (section 5.4). These results are quite reasonable for a global model. Averaging the difference factors in Table 14 for simulating Kechkar *et al.*'s work gives us 1.780; averaging the difference factors in Table 16 for simulating Pessoa *et al.*'s work give us 0.970. The later simulation has an average difference factor much closer to 1, thus has much better correspondence to the experimental results. This is due to the fact that the plasma's volume was better defined in Pessoa *et al.*'s work [13] (Figure 17) compared to Kechkar *et al.*'s work [10] (Figure 10). In Pessoa *et al.*'s work, the plasma was approximately occupying the whole chamber, which is the same condition as in my model. In Kechkar *et al.*'s work, the volume of the plasma was not so clearly defined, which was more likely being confined between the two electrodes (as we have seen for the pure O_2 plasma model's results in Table 14), thus had no chamber wall along the radial direction. As we have seen that at the same input power and pressure, the atomic oxygen and atomic fluorine's densities are dictated by the surface conditions, therefore as the surface area in Pessoa *et al.*'s work is better agreed with my model, their atomic oxygen and atomic fluorine's densities should be better agreed with my model's results too. A possible explanation for the differences in [O] of my model and the volume averaged [O] of Kechkar *et al.*'s experiment [10] is that the power coupled into the SF_6/O_2 plasma (when the SF_6 feed composition is non-zero) in the experiment is much higher than the value I use in my model (section 5.3.1). In the simulation for Pessoa *et al.*'s experiment, compare the simulated [F] with that of the experiment shown in Figure 18 we can see that in the experiment, the initial sticking coefficients of F and F_2's surface adsorptions gradually change with increasing O_2 feed composition, as oppose to a sharp 100 times decrease/increase as I have implemented in my model. They reach my proposed values at 40% O_2 feed composition and remain constant for higher O_2 feed compositions.

For all my simulations, I matched my model's simulated [e] values to that reported in the experiments due to the well known fact that the input power coupled into the electron population of a CCP plasma is only a fraction of the total input power (section 5.2 and section 5.4). As the techniques for measuring electron density have been well established (Langmuir probe and hairpin probe were used in Kechkar *et al.*'s work [10]), I expect the electron density values reported by the experimental works are accurate.

6 Fluctuations of the Plasma Global Model's Outputs Due to the Reaction Rate Coefficients' Statistical Variations

In chapter 5, I've discussed several sources of error in modelling a low pressure rf plasma discharge, such as the uncertainty of the exact volume where the plasma is confined in the chamber, the EEDF variations with the composition of the feedstock gas mixtures, the geometrical gas density variations and the inefficiency in coupling the input power to the electron population (see sections 5.2 and 5.3). Another source of plasma model inaccuracy could stem from the cross section data uncertainties in their measurements, which in turn causes fluctuations of the reaction rate coefficients of plasma models. To my best knowledge, the fluctuations of plasma models' outputs due to these variations haven't been well studied. In this chapter, I'm going to discuss the method I used to study the aforementioned fluctuations of the plasma models' outputs, and show the results of applying the method to my SF_6 plasma global model with heterogeneous surface model.

As we have seen in section 5.1, the variations in the neutral species surface reactions' initial sticking coefficients can alter some of the simulated densities by several times. Kokkoris *et al.* [4], section 5.4 tested the sensitivity of their SF_6 plasma model's outputs on the initial sticking coefficients of some of the neutral species surface reactions. They gave a factor of 10 variation to certain initial sticking coefficients, and they saw a factor of 2 difference in some of the simulated neutral densities. Because in low pressure processing plasma discharges, due to their small densities compared to the neutral's, the charged species usually have little influence on these neutral species surface reactions, thus the neutral species surface reactions can be considered as neutral-neutral reactions when dealing with the rate coefficient uncertainties. Therefore, I can not simply investigate the variation of my plasma model's outputs caused by the neutral-neutral reactions' cross section uncertainties without considering the uncertainties of the neutral species surface reactions' initial sticking coefficients. Unfortunately, Kokkoris *et al.* [4] didn't give the uncertainties of their surface reaction initial sticking coefficients, and pursuing the method of calculating these initial sticking coefficients and deduce their uncertainties is beyond the scope of this work. Thus in this work, only the uncertainties of the electron-involving reactions cross sections are considered.

6.1 The Method

The rate coefficient of an electron-involving reaction can be calculated as $<\sigma v>$ [62], p.12 (the average of σv for all v above the electron threshold energy of the reaction), where σ is commonly denoted by $\sigma(\varepsilon)$, and is the cross section measured at every electron energy ε for an electron-involving reaction, v is the electron speed. In practice, the rate coefficient of an electron-involving reaction can be obtained by averaging σv for v from the reaction's electron threshold energy to infinity as:

$$k = \langle \sigma v \rangle = \int_{E_{\mathrm{th}}}^{\infty} \sigma(\varepsilon) v(\varepsilon) f(\varepsilon) d\varepsilon, \tag{90}$$

where ε is the electron energy; $f(\varepsilon)$ is the EEDF (electron energy distribution function); $v(\varepsilon) = \sqrt{(2\varepsilon/m)}$ is the electron speed expressed in ε, where m is the electron mass in kg; E_{th} is the electron threshold energy of the reaction.

Let the fractional uncertainty of a certain reaction's cross section measurement to be denoted by ξ, and let R denote the random fractional factor that describes how much a reported cross section deviates from the accurate value, $R \in [1 - \xi, 1 + \xi]$. If we assume the Rs of $\sigma(\varepsilon)$ (the cross section of the reaction) are the same at each value of ε, then Eq. (90) can be written as:

$$k_{\mathrm{rdm}} = \langle R \sigma v \rangle = R \int_{E_{\mathrm{th}}}^{\infty} \sigma(\varepsilon) v(\varepsilon) f(\varepsilon) d\varepsilon = Rk, \tag{91}$$

where k_{rdm} is a random rate coefficient in the range of $[k\ (1 - \xi), k\ (1 + \xi)]$, assuming $\xi < 1$, and k is the rate coefficient calculated from a cross section reported by the referenced work.

In this work, I assume the randomly generated R values of an electron-involving reaction follow a normal distribution whose mean value is 1, and fall within the range $[1 - \xi, 1 + \xi]$, thus ξ equals to 3 times the standard deviation of the randomly generated R values. I assume the cross section data was reasonably accurately measured, thus any R values outside the range $[1 - \xi, 1 + \xi]$ are cut off. To evaluate the output fluctuations of the SF_6 plasma global model with heterogeneous surface model, each of the chosen electron-involving reactions is given its own R value. By using Eq. (91), a set of randomly generated rate coefficients k_{rdm1} ($k_{\mathrm{rdm1}} \in [k_1 (1 - \xi_1), k_1 (1 + \xi_1)]$), k_{rdm2} ($k_{\mathrm{rdm2}} \in [k_2 (1 - \xi_2), k_2 (1 + \xi_2)]$) ... (where the subscripts 1, 2, ... represent Reaction 1, Reaction 2, ...) are used for a single run of the model. The model is then repeatedly run by 1000 times, each time with a different set of randomly generated k_{rdm}s.

6.2 The Uncertainties

The reaction set of the gas phase reactions of the SF_6 plasma global with heterogeneous surface model is given in Table 1. The selected electron-involving reactions of the SF_6 plasma for investigating the fluctuations of the model's outputs are listed in Table 17, along with their rate coefficients' uncertainties.

Table 17 Cross section uncertainties of the selected reactions.

Selected electron-involving reactions and their cross section measurement uncertainties of the SF_6 plasma global model with heterogeneous surface model for investigating the fluctuations of the model's outputs.

No. in Table 1	Reaction	Uncertainty ξ	Reference
R1K1	$SF_6 + e \rightarrow SF_5 + F + e$	11 %	Based on Ref. [63], the uncertainty of the reactions R1K1, R2K1 and R3K1 is equal to the uncertainty of $\sigma_{\mathrm{dis,neut,t}}(\varepsilon)$ (the total cross section for electron impact dissociation into neutrals), but $\sigma_{\mathrm{dis,neut,t}}(\varepsilon) \approx [\sigma_{\mathrm{sc,t}}(\varepsilon) - \sigma_{\mathrm{e,int}}(\varepsilon)] - \sigma_{\mathrm{i,t}}(\varepsilon)$, thus I assume the uncertainty is equal to the largest uncertainty among $\sigma_{\mathrm{sc,t}}(\varepsilon)$, $\sigma_{\mathrm{e,int}}(\varepsilon)$ and $\sigma_{\mathrm{i,t}}(\varepsilon)$, to avoid possible negative R values for these reactions [$\sigma_{\mathrm{sc,t}}(\varepsilon)$: the total electron scattering cross section; $\sigma_{\mathrm{e,int}}(\varepsilon)$: the elastic integral electron scattering cross section; $\sigma_{\mathrm{i,t}}(\varepsilon)$: the total ionization cross section].
R2K1	$SF_6 + e \rightarrow SF_4 + 2F + e$	11 %	
R3K1	$SF_6 + e \rightarrow SF_3 + 3F + e$	11 %	
R4K1	$SF_5 + e \rightarrow SF_4 + F + e$	Same as R1K1	
R5K1	$SF_4 + e \rightarrow SF_3 + F + e$	Same as R1K1	
R8K1	$SF_6 + e \rightarrow SF_5^+ + 2e + F$	7 %	Uncertainties of R8K1, R9K1 and R10K1 are obtained based on the discussion in Section 4.2 of Ref. [63].
R9K1	$SF_6 + e \rightarrow SF_4^+ + 2e + 2F$	7 %	
R10K1	$SF_6 + e \rightarrow SF_3^+ + 2e + 3F$	7 %	
R11K1	$SF_5 + e \rightarrow SF_5^+ + 2e$	15 %	[64]
R12K1	$SF_5 + e \rightarrow SF_4^+ + F + 2e$	18 %	[64]
R13K1	$SF_4 + e \rightarrow SF_4^+ + 2e$	15 %	Same as R11K1 as suggested by Ref. [4].
R14K1	$SF_4 + e \rightarrow SF_3^+ + F + 2e$	18 %	Same as R12K1 as suggested by Ref. [4].
R15K1	$SF_3 + e \rightarrow SF_3^+ + 2e$	15 %	[64]
R18K1	$SF_6 + e \rightarrow SF_6^-$	10 %	Section 6.1.1 of Ref. [63].

6.3 The Results

The results of running the SF_6 plasma global model with heterogeneous surface model for 1000 times, each time with randomly generated rate coefficients for the electron-involving reactions listed in Table 17, are given in Table 18. The model's setup is the same for simulating Pessoa *et al.*'s work in section 5.4, its input parameters are: SF_6 feedstock gas input rate: 10 sccm; input power: 14.7 W; residence time: 0.0946 s; the gas temperature is 600 k and assumed to be constant (see section 2.2.1); cylindrical chamber length: 0.147 m, diameter: 0.1 m (see Figure 2).

Table 18 Effect of the rate coefficient variations on a low pressure SF_6 plasma model's outputs.

This table lists the fluctuations of the SF_6 plasma global model with heterogeneous model's outputs by running the model with randomly generated rate coefficients for the electron-involving reactions listed in Table 17 for 1000 times. The method is described in section 6.1. The model's input parameters are listed in section 6.3. Druyvesteyn EEDF was assumed for the model. All results were obtained in steady state.

Model Outputs	min	max	Diff. [(max−min)/min × 100%]
[e]	2.84511×10^{15} (m^{-3})	3.21424×10^{15} (m^{-3})	12.9743 %
T_e	5.29355 (V)	5.4001 (V)	2.01273 %
[SF_6]	2.2622×10^{20} (m^{-3})	2.31947×10^{20} (m^{-3})	2.53186 %
[SF_5]	1.27598×10^{19} (m^{-3})	1.33794×10^{19} (m^{-3})	4.85574 %
[SF_4]	2.93921×10^{18} (m^{-3})	3.23257×10^{18} (m^{-3})	9.98081 %
[SF_3]	7.15694×10^{17} (m^{-3})	8.2873×10^{17} (m^{-3})	15.7939 %
[F_2]	6.50581×10^{19} (m^{-3})	6.79533×10^{19} (m^{-3})	4.45017 %
[F]	8.8713×10^{18} (m^{-3})	9.06643×10^{18} (m^{-3})	2.19956 %
[SF_5^+]	5.37146×10^{16} (m^{-3})	5.93646×10^{16} (m^{-3})	10.5184 %
[SF_4^+]	3.13853×10^{15} (m^{-3})	3.77844×10^{15} (m^{-3})	20.3889 %
[SF_3^+]	8.72502×10^{15} (m^{-3})	9.50181×10^{15} (m^{-3})	8.90306 %
[F_2^+]	1.81424×10^{15} (m^{-3})	2.02294×10^{15} (m^{-3})	11.5035 %
[SF_6^-]	2.10649×10^{16} (m^{-3})	2.49785×10^{16} (m^{-3})	18.5789 %
[F^-]	4.29294×10^{16} (m^{-3})	4.66546×10^{16} (m^{-3})	8.67757 %
θ_{SF5}	0.671975	0.675084	0.462706 %
θ_{SF4}	0.0262965	0.0282781	7.53552 %
θ_{SF3}	0.00318984	0.00359365	12.6593 %
θ_F	0.033423	0.0340689	1.93261 %

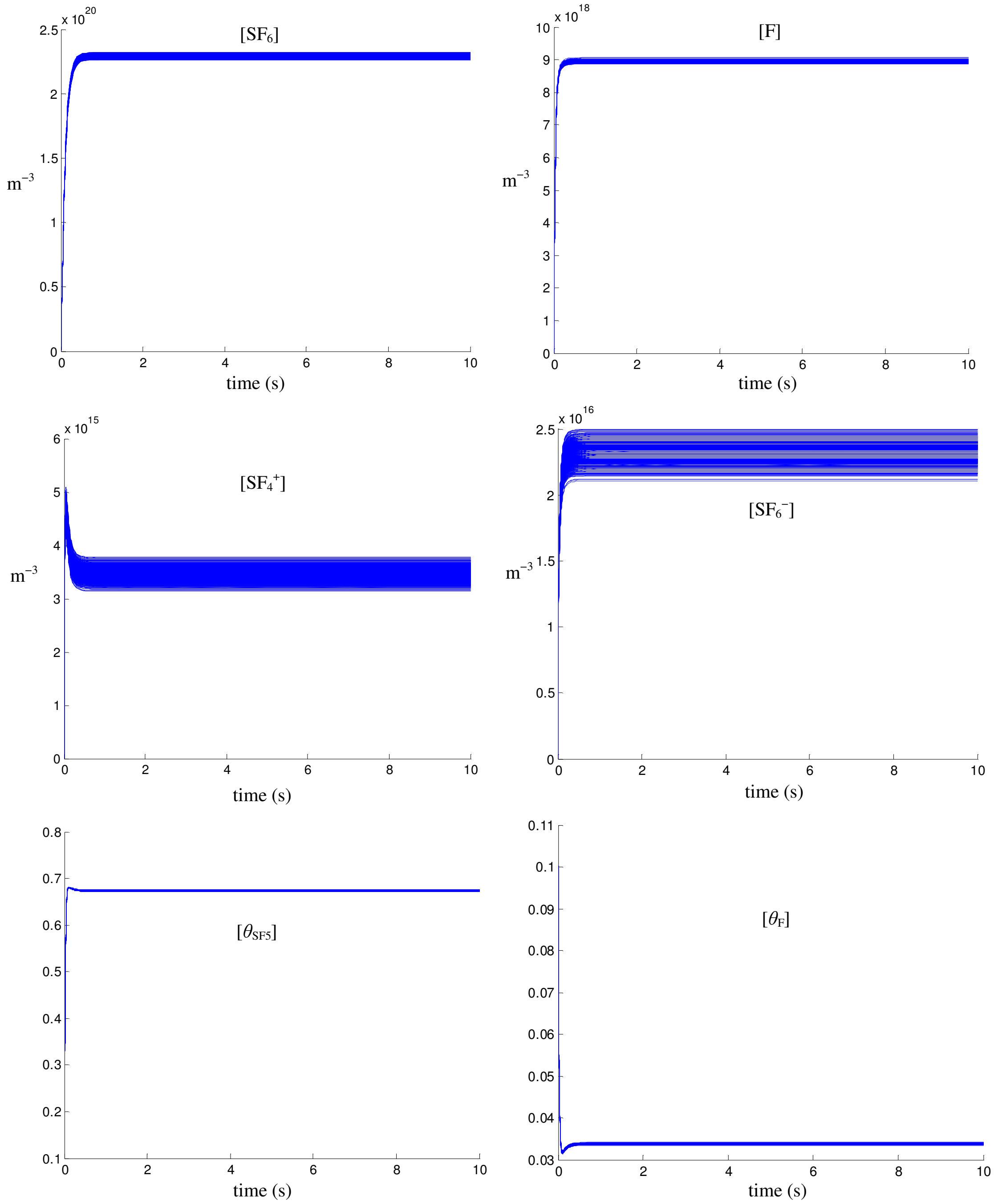

Figure 22 Selected results of the SF_6 plasma model with randomly generated rate coefficients. The results were obtained by running the SF_6 plasma global model with heterogeneous surface model with randomly generated rate coefficients for the electron-involving reactions listed in Table 17 for 1000 times. The full results are listed in Table 18.

From the results listed in Table 18 we can see that the largest fluctuation for the densities is 20.39 % from [SF_4^+]. The electron temperature T_e (2.01 %) and the surface coverage of the dominating adsorbate on the chamber wall $SF_{5(s)}$ (0.46 % for θ_{SF5}) are almost not affected. Thus the uncertainties in the measured cross section data of the electron-involving reactions in my SF_6 plasma global model with heterogeneous surface model are not the cause of a large fluctuation (such as a several-times increase) in a species' density.

Some of the selected simulation results for this work are shown in Figure 22.

7 Electron Heating in ECR Plasma Discharges

One crucial problem of the rf source plasmas is that the ion-bombarding flux and the ions' bombarding energy can not be controlled independently [1], p.17. For practical operations with reasonable ion flux, the high sheath voltage at the driven electrode can cause damage to the wafer placed on it, or over-etch surface structures and loss the linewith control. The low ion flux and high ion energy also limit the viability of the rf discharge plasmas for many applications. One problem the microelectronic manufacturing industry faces today is the wafer to wafer variations in plasma processes. The relatively low ion density of the rf source plasmas results in low processing rate, thus requires multi-wafer processing for industry level production, however, this generally hinders the wafer-to-wafer reproducibility, and lowers the yield rate. To overcome this problem, single-wafer processing is desired, and plasma discharge with higher ion flux and reasonable ion bombarding energy is required. (see Ref. [1])

To overcome the limitations of the rf source plasmas, ECR (electron cyclotron resonance) plasma sources have been widely used by the microelectronic manufacturing industry. In ECR plasma source chambers, the key to achieve low sheath potential is to couple a microwave power through a dielectric window [1], p. 18.

In terms of modelling, for an rf discharge, one normally assumes that all the input power is used to heat the electrons, however in practice, significant amount of power is coupled to the ions, which could be a source of inaccuracy of the model. For an ECR discharge, the microwave more effectively heats the electrons, thus in theory, the model's simulation result will be more accurate. Therefore, it's important to have a good understanding of the electron heating in ECR plasmas.

In this chapter, I'm going to follow the discussion in Lieberman and Lichtenberg's work, Ref. [1], chapter 13 to discuss a way to calculate the electron heating in ECR discharges. In Lieberman and Lichtenberg's work, most of the equations were not given derivations, here I give derivations to most of the equations listed in their work. I also give additional discussions to make the material as clear as possible.

7.1 ECR Plasma Source Configurations

A simple ECR source plasma chamber is shown in Figure 23. For an ECR source chamber, the coils surrounding the chamber generate strong axially varying dc (time-independent) magnetic field ($B \approx 875$ G [4]). A microwave (typically $f = 2450$ MHz) is injected axially through a dielectric window. As the dc magnetic field varies axially, at some point along the axial direction of the chamber, the Lorentz force induced gyration of the electrons has the same frequency as the electric field of the microwave's right-hand circularly polarized (RHP) wave. If an electron's gyration is in phase with the electric field of the RHP wave, the electron will be continuously accelerated within the dish-shaped resonance zone. As pointed out by Lieberman and Lichtenberg, “the fate of the LHP (left-hand polarized) wave is unclear, but it is probably inefficiently converted to a RHP wave” [1], p.494. The dc magnetic field normally has a monotonically decreasing profile, with stronger field near the dielectric window where the microwave is injected. In practice, additional magnetic coils could be used down the chamber's axial direction to enhance the dc magnetic field, and creates multiply resonance zones along the axial direction. Interested readers can refer to Ref. [1], chapter 13 for more information.

---

[4] Note B is measured in teslas in SI units, where 1 tesla = 10,000 gauss.

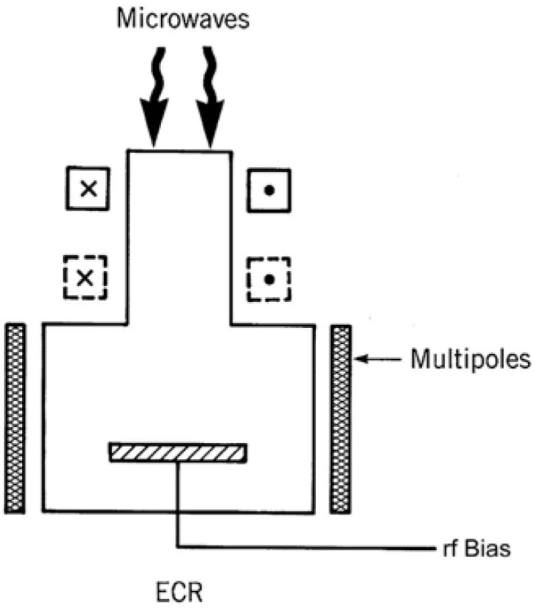

Figure 23 A simple ECR source chamber configuration.
(from Ref. [1], page 19)

7.2 Electron Heating

We can decompose a linearly polarized microwave into the sum of two counter-rotating circularly polarized waves. Assume the linearly polarized microwave has *x* polarization, as shown in Figure 24, we have

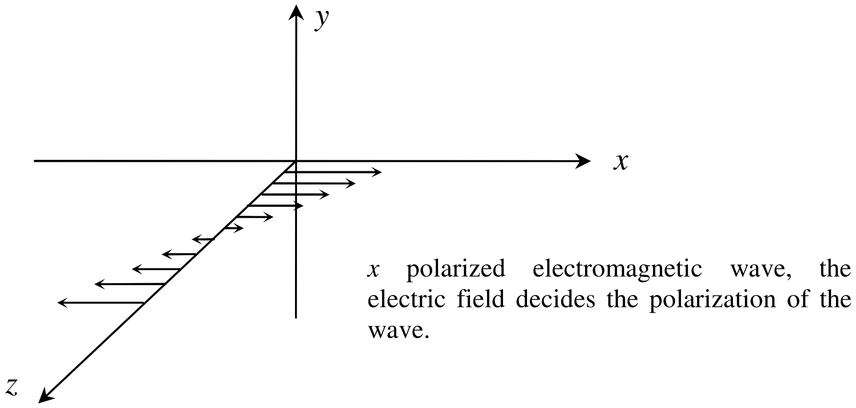

Figure 24 The electric field of the linearly polarized microwave.

$$\mathbf{E}(\mathbf{r},t) = \mathrm{Re}\left\{ \hat{x}E_x(\mathbf{r})\mathrm{e}^{j\omega t} \right\}, \tag{92}$$

where $E_x(\mathbf{r})$ is taken to be pure real. Then we have

$$\hat{x}E_x = (\hat{x} - j\hat{y})E_\mathrm{r} + (\hat{x} + j\hat{y})E_\mathrm{l}, \tag{93}$$

where $\hat{x}$ and $\hat{y}$ are unit vectors, E_r and E_l are the amplitudes of the RHP and LHP waves, with $E_\mathrm{r} = E_\mathrm{l} = E_x/2$. We can consider each of the terms in Eq. (93) as a **phasor**. Generally, a sinusoidal complex quantity can be written as $A\exp[j(\omega t + \phi)]$, we call $A\exp(j\phi)$ a phasor, which is *complex*, some books write it as $A\angle\phi$. However, when we use a phasor for calculation, we have to write the full form of it, i.e., we have to explicitly write out $A\exp[j(\omega t + \phi)]$. From this we can see that if E_x is real, we can consider E_x as a phasor with $\phi = 0$. The terms $\pm j$ can be written as

$$\pm j = \exp\left(\pm\frac{\pi}{2}j\right). \tag{94}$$

Therefore, the purpose of multiplying $\pm j$ to $\hat{y}$ in Eq. (93) is to indicate the phase difference between $\mathbf{E}_\mathrm{r}$ and $\mathbf{E}_\mathrm{l}$'s y-components, which has nothing to do with the directions of $\mathbf{E}_\mathrm{r}$ and $\mathbf{E}_\mathrm{l}$; as vectors, their directions are only decided by the unit vectors $\hat{x}$ and $\hat{y}$. Eq. (93) tells us that the x-components of $\mathbf{E}_\mathrm{r}$ and $\mathbf{E}_\mathrm{l}$ are exactly the same, while the y-components of $\mathbf{E}_\mathrm{r}$ and $\mathbf{E}_\mathrm{l}$ are 180° out of phase (that is when the y-component of $\mathbf{E}_\mathrm{r}$ points to the $+y$ direction, the y-component of $\mathbf{E}_\mathrm{l}$ points to the $-y$ direction) and have the same magnitude.

The electric field vector of the RHP (right-hand polarized) wave rotates by the right-hand rule [5] at frequency ω. We now apply a uniform magnetic field $\mathbf{B}_0$ as shown in Figure 25. An electron travelling in the plane parallel to the electric field but perpendicular to $\mathbf{B}_0$ also gyrates by the right-hand rule at frequency ω_ce. As shown by the four figures in the top row of Figure 25, for the RHP wave, if $\omega_\mathrm{ce} = \omega$, and the electron's gyration is in phase with the electric field of the RHP wave, the force $-eE$ accelerates the electron at every moment in its gyrating cycle, and the electron continuously gain energy, we say the electron is in **resonance** with the electric field; for the LHP (left-hand polarized) wave, however, as shown by the four figures in the

---

[5] Point the thumb of the right hand to the direction of wave propagation, the winding direction of the other fingers gives the direction of rotation.

bottom row of Figure 25, after one cycle, the energy gained and lost by the electron cancel each other, therefore no net energy gain for the electron in this case.

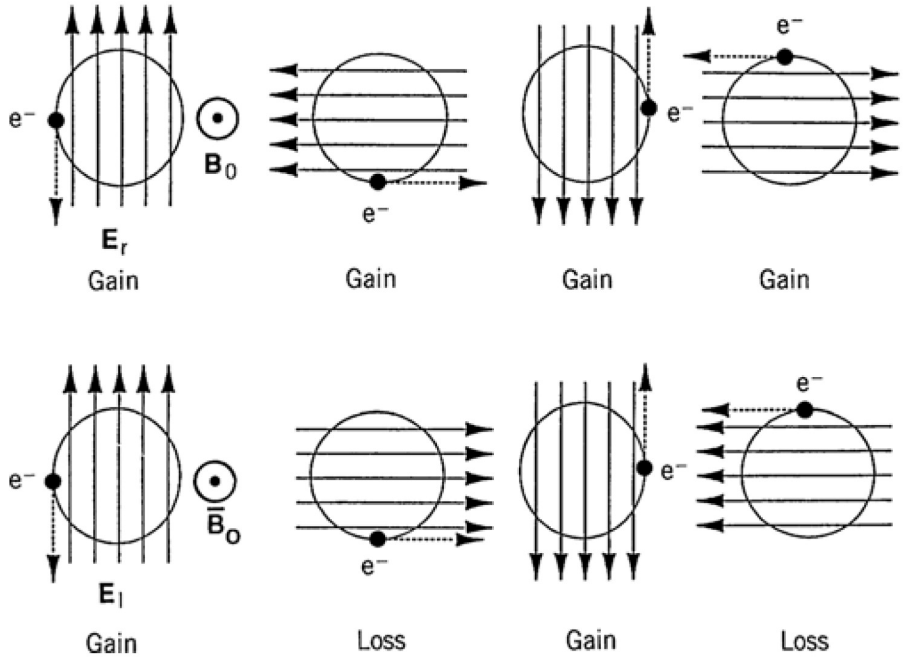

Figure 25 Electron acceleration in ECR plasmas.
The four figures in the top row shows an electron in resonance with the electric field of the RHP wave in one cycle; the four figures in the bottom row shows an electron's interaction with the electric field of the LHP wave in one cycle, the energy gained and lost by the electron cancels each other, thus the electron is not accelerated. (from Ref. [1], page 497)

I point out here that if we assume the electrons are in uniform circular motion (which is the case when there's no microwave applied to an ECR plasma chamber), we can equate the outward centrifugal force to the inward Lorentz force

$$m\frac{v^2}{R} = qvB_0, \tag{95}$$

where v is the electron's linear gyration speed, R is the gyration radius, m is the mass of the electron. Substitute the relation $v = \omega R$ into Eq. (95), we have

$$m\frac{(\omega R)^2}{R} = q\omega RB_0 \Rightarrow \omega = \frac{qB_0}{m}. \tag{96}$$

Thus the electron's gyration frequency only depends on B_0, which implies the locations of the resonance zones only depends on the geometry of B_0. Furthermore, as pointed out by Chen and Chang [62], p. 47, when in resonance with the electric field, "those electrons moving in the wrong direction (see the first paragraph of section 7.2.1 for more details) will be decelerated by the field, but will eventually be turned around and be accelerated in phase with the field." Although the resonance electrons only gain energies within their gyration plane perpendicular to $\mathbf{B}_0$, their velocity distribution makes their motion isotropic, and the energies they gained rapidly transfer between electrons through collisions and heat the entire electron population. "Since a thermal electron can lose only its small thermal energy while an electron in the right phase can gain 100s of eV of energy while it is in resonance, there is a net gain of energy by the distribution as a whole.".

7.2.1 Collisionless Heating

As discussed at the end of section 7.2, the nonuniformity of the magnetic field $B(z)$ is important when calculating the heating power. For $\omega_{\mathrm{ce}} \neq \omega$, the energy of the electron oscillates in a frequency of $\omega_{\mathrm{ce}} - \omega$. When an electron passes the resonance zone, it may gain or lose energy, depending on if its gyration is in the right direction. I point out here that all electrons gyrate same-clockwisely perpendicular to a magnetic field. If the electron's gyration is out of phase with the electric field's gyration, the electric field will keep altering the electron's gyration path, which may either accelerate or decelerate the electron, thus keep altering the phase difference between the electron and the electric field's gyrations. If the electron stays in the resonance zone long enough, it will be ultimately in phase with the electric field and gain energy. Here "in phase" means "the velocity of the electron is in opposite direction to the RHP electric field at all times" (or the phase angles of the electron and the electric field's gyrations are the same at all times), as shown by the four figures in the top row of Figure 25. If an electron in the resonance zone is in the wrong direction and the electron's speed along the z axis is large enough, it can pass the resonance zone before it is in phase with the electric field. In this case, the electron can lose energy in this pass (small thermal energy) if the electric field's deceleration dominates its acceleration on the electron, or gain small energy vice versa. If the electron still remains in the resonance zone when it's in phase with the electric field, it can gain 100s of eV of energy.

We now estimate the electron heating for low power absorption [6], where the electric field at the resonance zone is known. The magnetic field near resonance can be expanded as

$$\omega_{\mathrm{ce}}(z') = \omega(1+\alpha\, z')\,. \tag{97}$$

where $z' = z - z_{\mathrm{res}}$ is the distance from exact resonance. Differentiate Eq. (97), we have

$$\begin{aligned}\frac{\partial\omega_{\mathrm{ce}}(z')}{\partial z'} &= \frac{\partial\omega(1+\alpha\; z')}{\partial z'}\\ &= \omega\frac{\partial(1+\alpha\; z')}{\partial z'} = \omega\alpha\\ &\Rightarrow \alpha = \frac{1}{\omega}\frac{\partial\omega_{\mathrm{ce}}(z')}{\partial z'}\,.\end{aligned}$$

At resonance, $\omega = \omega_{\mathrm{ce}}$, therefore we can write α at resonance as

$$\alpha = \left(\frac{1}{\omega_{\mathrm{ce}}}\right)\left(\frac{\partial\omega_{\mathrm{ce}}}{\partial z'}\right)_{\mathrm{res}}, \tag{98}$$

which is proportional to the gradient in $B(z)$ near the resonance zone. I point out that Eq. (97) can be rearranged to get

$$\omega\alpha\, z' = \omega_{\mathrm{ce}} - \omega\,, \tag{99}$$

thus $z'\omega\alpha$ gives the difference between the resonance frequency and the electron's gyration frequency when the electron is z' away from the exact resonance. And we approximate $z'(t) \approx v_{\mathrm{res}}t$, where v_{res} is the electron speed parallel to the z axis at resonance. For ease of calculation, we let $z = 0$ and $t = 0$ at the exact resonance.

Let the transverse velocity of the electron's right-hand gyration, which points from the gyration centre to the electron, be $v_{\mathrm{r}} = v_x + jv_y$ (the velocity perpendicular to $B(z)$), or write it in phasor form:

---

[6] For low power absorption, the electric field within the resonance zone can be assumed constant and can be deduced from the input power. In strong power absorption, however, attenuation of the microwave in the resonance zone occurs, and the value of E_{r} in the resonance zone is much smaller than its incident value. See Ref. [1], pp. 501 – 507 for the treatment of strong power absorption in an ECR plasma.

$$v_{\mathrm{r}} = \tilde{v}_{\mathrm{r}} \mathrm{e}^{j\omega t}. \tag{100}$$

The complex force equation for the electron is

$$\frac{d(\tilde{v}_{\mathrm{r}} \mathrm{e}^{j\omega t})}{dt} - j\omega_{\mathrm{ce}}(z)\tilde{v}_{\mathrm{r}} \mathrm{e}^{j\omega t} = -\frac{e}{m} E_{\mathrm{r}} \mathrm{e}^{j\omega t}, \tag{101}$$

where E_{r} is the amplitude of the RHP wave and

$$\mathbf{E} = \mathrm{Re}\{(\hat{x} - j\hat{y})E_{\mathrm{r}} \mathrm{e}^{j\omega t}\}, \tag{102}$$

where $(\hat{x} - j\hat{y})E_{\mathrm{r}}$ is the RHP electric field with E_{r} in phasor form as I've discussed for Eq. (93). Although here E_{r} is a real number, we can still consider it as a phasor with a phase of 0: $E_{\mathrm{r}} = E_{\mathrm{r}} \mathrm{e}^{j0}$.

It's a little tricky to understand this equation, so I'm going to pause and give some insights in Eq. (101). In the resonance zone, the electron's acceleration caused by the RHP wave's electric field can be decomposed to two components: one is tangential to it's gyration radius (the first term on the LHS of Eq. (101)) and the other is along its gyration radius (the second term on the LHS of Eq. (101)). As I have discussed at the beginning of this section, an electron in the resonance zone may not in phase with the electric field, but the electric field will eventually turn the electron around and make it in phase with it. Eq. (101) represents the acceleration or deceleration of an electron in the resonance zone by the electric field. Incidentally, the motion described by the left hand side of Eq. (101) is not a uniform circular motion, for example when the electron is in resonance with the electric field of the RHP wave, the component of the $-eE_{\mathrm{r}}$ force tangential to the gyration radius accelerates the electron's linear gyration speed. As the linear gyration speed increases with time, to keep $\omega_{\mathrm{ce}} = \omega = \mathrm{const}$ within the resonance zone, the electron's gyration radius must be larger and larger.

Now for the second term on the left hand side of Eq. (101). The angular velocity ϕ is defined as

$$\phi = \frac{v}{r} = \frac{2\pi}{T} = \omega, \tag{103}$$

where v is the linear velocity of a gyrating object, r is the gyration radius, T is the gyration period, ω is the angular frequency of the gyration.

The angular acceleration a_ϕ is defined as

$$a_\phi = \frac{v^2}{r} = \phi^2 r\,, \tag{104}$$

substitute $\phi = \omega = v/r$ into the Eq. (104), we have

$$a_\phi = \omega v\,. \tag{105}$$

Compare Eq. (105) and the second term on the left hand side of Eq. (101), we can see that $\omega_{\mathrm{ce}}(z)\tilde{v}_{\mathrm{r}}$ is the angular acceleration along the electron's gyration radius. The $-j$ multiplied to $\omega_{\mathrm{ce}}(z)\tilde{v}_{\mathrm{r}}$ is the phase difference as I've discussed for Eq. (94). The reason for this is that although the electron in the resonance zone under the $-eE_{\mathrm{r}}$ force won't travel in uniform circular motion, the frequency of its circular motion ω_{ce} has to be constant and equal to ω. At any moment, the electron in the resonance zone has a linear acceleration that tangential to its gyration radius, as well as an angular acceleration that perpendicular to its linear acceleration. Although the linear acceleration and angular acceleration of the electron have to change at every moment, at any instantaneous time t, because the gyration frequency ω is kept constant, no matter what value v_{r} is at time t, if we stop the time at t, pause any other motions and only allow the angular acceleration to rotate, it has to rotate back a period of $D/4$ (where D is the electron gyration period at the instantaneous time t) in order to be pointing to the same direction as the linear acceleration at that moment (time t). That is, the angular acceleration is $\pi/2$ behind the linear acceleration in phase, which corresponds to a phase factor of $-j$.

Now come back to our mission of calculating the electron heating. Solve the time derivative in Eq. (101), we have (note from Eq. (100) that the magnitude of $\tilde{v}_{\mathrm{r}}$ changes with time):

$$\frac{d(\tilde{v}_{\mathrm{r}}\mathrm{e}^{j\omega t})}{dt} - j\omega_{\mathrm{ce}}(z)\tilde{v}_{\mathrm{r}}\mathrm{e}^{j\omega t} = -\frac{e}{m}E_{\mathrm{r}}\mathrm{e}^{j\omega t}$$

$$\Rightarrow \mathrm{e}^{j\omega t}\frac{d\,\tilde{v}_{\mathrm{r}}}{dt}+\tilde{v}_{\mathrm{r}}\,j\omega\mathrm{e}^{j\omega t}-j\omega_{\mathrm{ce}}\tilde{v}_{\mathrm{r}}\mathrm{e}^{j\omega t}=-\frac{e}{m}E_{\mathrm{r}}\mathrm{e}^{j\omega t}$$

$$\Rightarrow \frac{d\,\tilde{v}_{\mathrm{r}}}{dt}+\tilde{v}_{\mathrm{r}}\,j(\omega-\omega_{\mathrm{ce}})=-\frac{e}{m}E_{\mathrm{r}}\,. \tag{106}$$

From Eq. (97) $\omega_{\mathrm{ce}}(z')=\omega(1+\alpha\,z')$, we have

$$\omega-\omega_{ce}=-\omega\alpha\,z'\,. \tag{107}$$

Substitute Eq. (107) into Eq. (106), and use $z'\approx v_{\mathrm{res}}t$ as stated below Eq. (97), we have

$$\frac{d\,\tilde{v}_{\mathrm{r}}}{dt}-j\omega\alpha\,v_{\mathrm{res}}t\,\tilde{v}_{\mathrm{r}}=-\frac{e}{m}E_{\mathrm{r}}\,. \tag{108}$$

We now introduce a phase angle $\theta(t)$:

$$\theta(t)=\omega\alpha\,v_{\mathrm{res}}t^{2}/2\,,\qquad(-T\le t\le T) \tag{109}$$

where T denotes the time interval between the electron's initial and final time when it travels near the resonance zone. Let $t=-T$ denote the initial time that the electron travels along the z axis near the resonance zone (recall from the discussion below Eq. (99), at the exact resonance, $z=0$ and $t=0$.); let $t=T$ denote the final time that the electron travels along the z axis near the resonance zone [65], p. 1079. I now give some insights of the meaning of $\theta(t)$. Based on the discussion below Eq. (99), $v_{\mathrm{res}}t\approx z'$, thus Eq. (109) can be written as

$$\theta(t)=z'\omega\alpha\,t/2\,, \tag{110}$$

as I have discussed below Eq. (99), $z'\omega\alpha$ gives the difference between the resonance frequency and the electron's gyration frequency when the electron is z' away from the exact resonance. Use Eq. (99), we have:

$$\omega\alpha\,z't=t(\omega_{\mathrm{ce}}-\omega)\,,$$

i.e., $z'\omega\alpha t$ gives the phase difference of the electron when it's time t away from the exact resonance and when it's at the exact resonance ($t=0$). Thus,

$$\theta(t) = (\omega_{\mathrm{ce}} - \omega)\frac{t}{2}. \tag{111}$$

Eq. (111) shows that $\theta(t)$ in Eq. (109) represents the phase difference of an electron when it's time t away from the exact resonance and when it's at the exact resonance ($t = 0$). I point out here that the factor 1/2 in Eq. (109) is only there for the ease of later calculations. Because due to the fact that the phase difference of a electron when it's time t away from the exact resonance and when it's at the exact resonance ($t = 0$) could take any value, depending on how many circles it has gyrated when it reaches the exact resonance (say, for example, 100π, assume T is large enough, see footnote 7 in page 129). Therefore, multiplying 1/2 to $\theta(t)$ won't introduce any effect to the calculations.

Now substitute Eq. (109) in the complex rotation term for the phasors,

$$\mathrm{e}^{-j\theta(t)} = \mathrm{e}^{-j\omega\alpha\, v_{\mathrm{res}} t^2/2}, \tag{112}$$

and multiply Eq. (112) to Eq. (108), we have

$$\frac{d\,\tilde{v}_{\mathrm{r}}}{dt}\mathrm{e}^{-j\omega\alpha\, v_{\mathrm{res}} t^2/2} - j\omega\alpha\, v_{\mathrm{res}} t\, \tilde{v}_{\mathrm{r}}\mathrm{e}^{-j\omega\alpha\, v_{\mathrm{res}} t^2/2} = -\frac{e}{m}E_{\mathrm{r}}\mathrm{e}^{-j\omega\alpha\, v_{\mathrm{res}} t^2/2}. \tag{113}$$

Integrate Eq. (113) for all the possible t values from $t = -T$ to $t = T$, we obtain (here I assume v_{res} is independent of time because we're dealing with the collisionless case)

$$\begin{aligned}&\int_{-T}^{T}\frac{d\,\tilde{v}_r}{dt}\mathrm{e}^{-j\omega\alpha\, v_{\mathrm{res}} t^2/2}dt - j\omega v_{\mathrm{res}}\alpha\int_{-T}^{T}\tilde{v}_{\mathrm{r}} t\mathrm{e}^{-j\omega\alpha\, v_{\mathrm{res}} t^2/2}dt \\ &= -\frac{e}{m}E_{\mathrm{r}}\int_{-T}^{T}\mathrm{e}^{-j\omega\alpha\, v_{\mathrm{res}} t^2/2}dt.\end{aligned} \tag{114}$$

Apply integral by parts to the first term on the left hand, we have

$$\begin{aligned}\int_{-T}^{T}\frac{d\,\tilde{v}_r}{dt}\mathrm{e}^{-j\omega\alpha\, v_{\mathrm{res}} t^2/2}dt &= \tilde{v}_r\mathrm{e}^{-j\omega\alpha\, v_{\mathrm{res}} t^2/2}\Big|_{-T}^{T} - \int_{-T}^{T}\frac{d\mathrm{e}^{-j\omega\alpha\, v_{\mathrm{res}} t^2/2}}{dt}\tilde{v}_r dt \\ &= \tilde{v}_r(T)\mathrm{e}^{-j\omega\alpha\, v_{\mathrm{res}} T^2/2} - \tilde{v}_r(-T)\mathrm{e}^{-j\omega\alpha\, v_{res}(-T)^2/2} + j\omega v_{res}\alpha\int_{-T}^{T}\tilde{v}_r t\mathrm{e}^{-j\omega\alpha\, v_{\mathrm{res}} t^2/2}dt \\ &= \tilde{v}_r(T)\mathrm{e}^{-j\theta(T)} - \tilde{v}_r(-T)\mathrm{e}^{-j\theta(-T)} + j\omega v_{\mathrm{res}}\alpha\int_{-T}^{T}\tilde{v}_{\mathrm{r}} t\mathrm{e}^{-j\theta(t)}dt.\end{aligned} \tag{115}$$

Substitute Eq. (115) into Eq. (114), we have

$$\tilde{v}_{\mathrm{r}}(T)\mathrm{e}^{-j\theta(T)} - \tilde{v}_{\mathrm{r}}(-T)\mathrm{e}^{-j\theta(-T)} + j\omega v_{\mathrm{res}}\alpha\int_{-T}^{T}\tilde{v}_{\mathrm{r}} t\mathrm{e}^{-j\theta(t)}dt$$

$$- j\omega v_{\mathrm{res}}\alpha\int_{-T}^{T}\tilde{v}_{\mathrm{r}} t\mathrm{e}^{-j\theta(t)}dt = -\frac{e}{m}E_{\mathrm{r}}\int_{-T}^{T}\mathrm{e}^{-j\theta(t)}dt$$

$$\Rightarrow \tilde{v}_{\mathrm{r}}(T)\mathrm{e}^{-j\theta(T)} = \tilde{v}_{\mathrm{r}}(-T)\mathrm{e}^{-j\theta(-T)} - \frac{e}{m}E_{\mathrm{r}}\int_{-T}^{T}\mathrm{e}^{-j\theta(t)}dt\,. \tag{116}$$

As pointed out by Lieberman and Lichtenberg [1], p. 499, in the limit $T >> (2\pi/\omega|\alpha|v_{\mathrm{res}})^{1/2}$,[7] the integral in Eq. (116) is "the integral of a Gaussian of complex argument", the standard solution is:

$$\int_{-T}^{T}\mathrm{e}^{-j\theta(t')}dt' = (1-j)\left(\frac{\pi}{\omega|\alpha|v_{\mathrm{res}}}\right)^{1/2}. \tag{117}$$

Substitute Eq. (117) into Eq. (116), we have

$$\tilde{v}_{\mathrm{r}}(T)\mathrm{e}^{-j\theta(T)} = \tilde{v}_{\mathrm{r}}(-T)\mathrm{e}^{-j\theta(-T)} - (1-j)\frac{e}{m}E_{\mathrm{r}}\left(\frac{\pi}{\omega|\alpha|v_{\mathrm{res}}}\right)^{1/2}. \tag{118}$$

The complex conjugate of Eq. (118) is

$$\tilde{v}_{\mathrm{r}}^{*}(T)\mathrm{e}^{j\theta(T)} = \tilde{v}_{\mathrm{r}}^{*}(-T)\mathrm{e}^{j\theta(-T)} - (1+j)\frac{e}{m}E_{\mathrm{r}}\left(\frac{\pi}{\omega|\alpha|v_{\mathrm{res}}}\right)^{1/2}. \tag{119}$$

Multiply Eq. (119) to Eq. (118), we have

$$\left|\tilde{v}_{\mathrm{r}}(T)\right|^{2} = \left[\tilde{v}_{\mathrm{r}}(-T)\mathrm{e}^{-j\theta(-T)} - (1-j)\frac{e}{m}E_{\mathrm{r}}\left(\frac{\pi}{\omega|\alpha|v_{\mathrm{res}}}\right)^{1/2}\right]$$

$$\cdot\left[\tilde{v}_{\mathrm{r}}^{*}(-T)\mathrm{e}^{j\theta(-T)} - (1+j)\frac{e}{m}E_{\mathrm{r}}\left(\frac{\pi}{\omega|\alpha|v_{\mathrm{res}}}\right)^{1/2}\right]$$

$$= \left|\tilde{v}_{\mathrm{r}}(-T)\right|^{2} - (1+j)\tilde{v}_{\mathrm{r}}(-T)\mathrm{e}^{-j\theta(-T)}\frac{e}{m}E_{\mathrm{r}}\left(\frac{\pi}{\omega|\alpha|v_{\mathrm{res}}}\right)^{1/2} \tag{120}$$

---

[7] From Eq. (125) we can see $(2\pi/\omega|\alpha|v_{\mathrm{res}})^{1/2}$ is the effective time in resonance zone. The limit says the electron's travel time taken into account in our calculation is much larger than the time the electron remains in the resonance zone.

$$-(1-j)\tilde{v}_{\mathrm{r}}^{*}(-T)\mathrm{e}^{j\theta(-T)}\frac{e}{m}E_{\mathrm{r}}\left(\frac{\pi}{\omega|\alpha|v_{\mathrm{res}}}\right)^{1/2}+\left(\frac{eE_{\mathrm{r}}}{m}\right)^{2}\frac{2\pi}{\omega|\alpha|v_{\mathrm{res}}}.$$

Based on the discussion below Eq. (111), the initial "random" phase $\theta(-T)$ is the phase difference between the electron's gyration at the initial time $-T$ and at the exact resonance. Thus the initial "random" phase $\theta(-T)$ can take any value between 0 to 2π (any values larger than 2π can be reduced to an equivalent value within 0 to 2π). Averaging over $\theta(-T)$ will average the exponential terms in Eq. (120) over one period, which yields zero. With that said, Eq. (120) can be written as

$$\left|\tilde{v}_{\mathrm{r}}(T)\right|^{2}=\left|\tilde{v}_{\mathrm{r}}(-T)\right|^{2}+\left(\frac{eE_{\mathrm{r}}}{m}\right)^{2}\left(\frac{2\pi}{\omega|\alpha|v_{\mathrm{res}}}\right). \tag{121}$$

Eq. (121) can be rearranged to get the average speed gain per electron pass through the resonance zone:

$$(\Delta v)^{2}=\left|\tilde{v}_{\mathrm{r}}(T)\right|^{2}-\left|\tilde{v}_{\mathrm{r}}(-T)\right|^{2}=\left(\frac{eE_{\mathrm{r}}}{m}\right)^{2}\left(\frac{2\pi}{\omega|\alpha|v_{\mathrm{res}}}\right). \tag{122}$$

The average **electron energy gain per pass** is then

$$W_{\mathrm{ecr}}=\frac{1}{2}m(\Delta v)^{2}=\frac{1}{2}m\left(\frac{eE_{\mathrm{r}}}{m}\right)^{2}\left(\frac{2\pi}{\omega|\alpha|v_{\mathrm{res}}}\right)=\frac{e^{2}E_{\mathrm{r}}^{2}\pi}{m\omega|\alpha|v_{\mathrm{res}}}. \tag{123}$$

We also have the simple relation

$$\Delta v=\frac{eE_{\mathrm{r}}}{m}\Delta t_{\mathrm{res}}. \tag{124}$$

Substitute the expression for Δv from Eq. (122) to Eq. (124) we have

$$\Delta t_{\mathrm{res}}=\left(\frac{2\pi}{\omega|\alpha|v_{\mathrm{res}}}\right)^{1/2}, \tag{125}$$

the **effective time in resonance**.

The **effective resonance zone width** is

$$\Delta z_{\mathrm{res}} = v_{\mathrm{res}} \Delta t_{\mathrm{res}} = \left(\frac{2\pi\, v_{\mathrm{res}}}{\omega |\alpha|} \right)^{1/2} . \tag{126}$$

For typical ECR parameters, $\Delta z_{\mathrm{res}} \sim 0.5$ cm [1], p. 500.

The **absorbed power per area**, or **energy flux** can be obtained by multiplying the flux of the electrons passing the resonance zone $n v_{\mathrm{res}}$ with the energy gain per electron per pass obtained in Eq. (123):

$$S_{\mathrm{ecr}} = \frac{\pi\, n e^2 E_{\mathrm{r}}^2}{m \omega |\alpha|} . \tag{127}$$

Because within the resonance zone, the electron gyration and the RHP wave's electric field are in phase for the distance Δz_{res}, and time Δt_{res} the electron travelled within the resonance zone, thus we have

$$(\omega - \omega_{\mathrm{ce}}|_{v_{\mathrm{res}} \Delta t_{\mathrm{res}}}) \Delta t_{\mathrm{res}} \approx 0 . \tag{128}$$

As pointed out by Lieberman and Lichtenberg [1], p. 500, the absorbed energy S_{ecr} calculated here is proportional to the electron density and the square of the RHP wave's electric field magnitude. The fact that we assumed a constant v_{res} in our calculation made S_{ecr} also proportional to α^{-1} and independent of v_{res}, however, these won't be true if v_{res} is non-constant.

7.2.2 Collisional Heating

As I have discussed at the end of section 7.2.1, S_{ecr} is independent of v_{res} for constant v_{res}, which suggests us to take into account the collisions by setting a $v_{\mathrm{res}} \to 0$ limit.

The force equation for electron in the resonance zone can be written as [1], p. 87:

$$m\frac{d\,\mathbf{v}}{dt}=q[\mathbf{E}(\mathbf{r},t)+\mathbf{v}\times\mathbf{B}(\mathbf{r},t)].$$

Add collision terms $-f_{\mathrm{m}}\tilde{v}_x$ and $-f_{\mathrm{m}}\tilde{v}_y$ to the complex force equations in the *x* and *y* directions by using Eq. (101), with f_{m} the electron momentum transfer frequency, we have

$$j\omega\tilde{v}_x=-\frac{e}{m}\tilde{E}_x+j\omega_{\mathrm{ce}}\tilde{v}_y-f_{\mathrm{m}}\tilde{v}_x. \qquad (129)$$

$$j\omega\tilde{v}_y=-\frac{e}{m}\tilde{E}_y+j\omega_{\mathrm{ce}}\tilde{v}_x-f_{\mathrm{m}}\tilde{v}_y. \qquad (130)$$

where $\omega_{\mathrm{ce}}\tilde{v}_y$ and $\omega_{\mathrm{ce}}\tilde{v}_x$ are the angular acceleration as derived in Eq. (105).

Add Eqs. (129) and (130) together, we have

$$j\omega\left(\tilde{v}_x+\tilde{v}_y\right)=-\frac{e}{m}\left(\tilde{E}_x+\tilde{E}_y\right)+j\omega_{\mathrm{ce}}\left(\tilde{v}_x+\tilde{v}_y\right)-f_{\mathrm{m}}\left(\tilde{v}_x+\tilde{v}_y\right)$$

$$\Rightarrow\tilde{v}_x+\tilde{v}_y=\frac{-\frac{e}{m}\left(\tilde{E}_x+\tilde{E}_y\right)}{j\omega+f_{\mathrm{m}}-j\omega_{\mathrm{ce}}}. \qquad (131)$$

Eq. (129) subtracts Eq. (130), we have

$$j\omega\left(\tilde{v}_x-\tilde{v}_y\right)=-\frac{e}{m}\left(\tilde{E}_x-\tilde{E}_y\right)-j\omega_{\mathrm{ce}}\left(\tilde{v}_x-\tilde{v}_y\right)-f_m\left(\tilde{v}_x-\tilde{v}_y\right)$$

$$\Rightarrow\tilde{v}_x-\tilde{v}_y=\frac{-\frac{e}{m}\left(\tilde{E}_x-\tilde{E}_y\right)}{j\omega+f_{\mathrm{m}}+j\omega_{\mathrm{ce}}}. \qquad (132)$$

Add Eq. (131) to Eq. (132), we have:

$$\tilde{v}_x=-\frac{e}{2m}\left(\frac{\tilde{E}_x-\tilde{E}_y}{j\omega+f_{\mathrm{m}}+j\omega_{\mathrm{ce}}}+\frac{\tilde{E}_x+\tilde{E}_y}{j\omega+f_{\mathrm{m}}-j\omega_{\mathrm{ce}}}\right).$$

Eq. (131) subtracts Eq. (132), we have:

$$\tilde{v}_y = -\frac{e}{2m}\left(\frac{\tilde{E}_x + \tilde{E}_y}{j\omega + f_\mathrm{m} - j\omega_\mathrm{ce}} - \frac{\tilde{E}_x - \tilde{E}_y}{j\omega + f_\mathrm{m} + j\omega_\mathrm{ce}}\right).$$

Now we have

$$\tilde{v}_x + j\tilde{v}_y = -\frac{e}{2m}\left(\frac{\tilde{E}_x - \tilde{E}_y}{j\omega + f_\mathrm{m} + j\omega_\mathrm{ce}} + \frac{\tilde{E}_x + \tilde{E}_y}{j\omega + f_\mathrm{m} - j\omega_\mathrm{ce}}\right.$$
$$\left. + \frac{j\tilde{E}_x + j\tilde{E}_y}{j\omega + f_\mathrm{m} - j\omega_\mathrm{ce}} - \frac{j\tilde{E}_x - j\tilde{E}_y}{j\omega + f_\mathrm{m} + j\omega_\mathrm{ce}}\right).$$

Substitute $\tilde{E}_x = E_\mathrm{r}$, $\tilde{E}_y = -jE_\mathrm{r}$ from Eq. (102) into the above equation, we have

$$\tilde{v}_x + j\tilde{v}_y = -\frac{e}{2m}\left(\frac{E_\mathrm{r} + jE_\mathrm{r}}{j\omega + f_\mathrm{m} + j\omega_\mathrm{ce}} + \frac{E_\mathrm{r} - jE_\mathrm{r}}{j\omega + f_\mathrm{m} - j\omega_\mathrm{ce}}\right.$$
$$\left. + \frac{jE_\mathrm{r} + E_\mathrm{r}}{j\omega + f_\mathrm{m} - j\omega_\mathrm{ce}} - \frac{jE_\mathrm{r} - E_\mathrm{r}}{j\omega + f_\mathrm{m} + j\omega_\mathrm{ce}}\right)$$

$$= -\frac{e}{2m}\left(\frac{2E_r}{j\omega + f_\mathrm{m} - j\omega_\mathrm{ce}} + \frac{2E_r}{j\omega + f_\mathrm{m} + j\omega_\mathrm{ce}}\right)$$

$$= -\frac{eE_\mathrm{r}}{m}\frac{j\omega - j\omega_\mathrm{ce} + f_\mathrm{m} + j\omega + j\omega_\mathrm{ce} + f_\mathrm{m}}{(j\omega + f_\mathrm{m} - j\omega_\mathrm{ce})(j\omega + f_\mathrm{m} + j\omega_\mathrm{ce})}$$

$$= -\frac{2eE_\mathrm{r}}{m}\frac{j\omega + f_\mathrm{m}}{(j\omega + f_\mathrm{m})^2 + \omega_\mathrm{ce}{}^2}$$

$$= -\frac{2eE_\mathrm{r}}{m}\frac{1}{j\omega + f_\mathrm{m} + \dfrac{\omega_\mathrm{ce}{}^2}{j\omega + f_\mathrm{m}}}.$$

But $f_\mathrm{m} << \omega$, and $\omega \rightarrow \omega_\mathrm{ce}$ at resonance, thus the above equation can be written as

$$\tilde{v}_x + j\tilde{v}_y \approx -\frac{2eE_\mathrm{r}}{m}\frac{1}{j\omega + f_\mathrm{m} + \dfrac{\omega_\mathrm{ce}}{j + \dfrac{f_\mathrm{m}}{\omega}}} \approx -\frac{2eE_\mathrm{r}}{m}\frac{1}{j\omega + f_\mathrm{m} + \dfrac{\omega_\mathrm{ce}}{j}}$$

$$= -\frac{2eE_\mathrm{r}}{m}\frac{1}{f_\mathrm{m} + j(\omega - \omega_\mathrm{ce})}. \tag{133}$$

Now the **time-average power absorbed per electron** can be obtained by using the formula $P_{\text{avg}} = Fv$:

$$\overline{P}_{\text{ecr}} = \frac{1}{2}\text{Re}\left\{- e\tilde{E}_x \tilde{v}_x^* - e\tilde{E}_y \tilde{v}_y^*\right\}, \tag{134}$$

where the factor 1/2 is due to the fact that both positive and negative speeds (which should not be distinguished when considering kinetic energy) of an electron contribute the same power, thus doubles the power it absorbs.

Substitute $\tilde{E}_x = E_\text{r}$, $\tilde{E}_y = -jE_\text{r}$ into Eq. (134), we have

$$\begin{aligned}\overline{P}_{\text{ecr}} &= \frac{1}{2}\text{Re}(-e\tilde{E}_x \tilde{v}_x^* - e\tilde{E}_y \tilde{v}_y^*) = \frac{1}{2}\text{Re}(-eE_\text{r}\tilde{v}_x^* + ejE_\text{r}\tilde{v}_y^*)\\ &= \frac{1}{2}\text{Re}[-eE_\text{r}(\tilde{v}_x^* + j^*\tilde{v}_x^*)] = \frac{1}{2}\text{Re}[-eE_\text{r}(\tilde{v}_x^* + (j\tilde{v}_x)^*)]\\ &= \frac{1}{2}\text{Re}[-eE_\text{r}(\tilde{v}_x + j\tilde{v}_y)^*].\end{aligned} \tag{135}$$

From Eq. (133), we have

$$(\tilde{v}_x + j\tilde{v}_y)^* = -\frac{2eE_\text{r}}{m}\frac{1}{f_\text{m} - j(\omega - \omega_\text{ce})}. \tag{136}$$

Multiply $f_\text{m} + j(\omega - \omega_\text{ce})$ to both numerator and denominator of Eq. (136), we have

$$(\tilde{v}_x + j\tilde{v}_y)^* = -\frac{2eE_\text{r}}{m}\frac{f_\text{m} + j(\omega - \omega_\text{ce})}{f_\text{m}^2 + (\omega - \omega_\text{ce})^2},$$

thus

$$\text{Re}\left\{(\tilde{v}_x + j\tilde{v}_y)^*\right\} = -\frac{2eE_\text{r}}{m}\frac{f_\text{m}}{f_\text{m}^2 + (\omega - \omega_\text{ce})^2}. \tag{137}$$

Substitute Eq. (137) into Eq. (135) we have

$$\overline{P}_{\text{ecr}} = m\left(\frac{eE_\text{r}}{m}\right)^2 \frac{f_\text{m}}{f_\text{m}^2 + (\omega - \omega_\text{ce})^2}. \tag{138}$$

We see that at the exact resonance, $\omega \rightarrow \omega_{\mathrm{ce}}$,

$$\overline{P}_{\mathrm{ecr}} \rightarrow \frac{e^2 E_{\mathrm{r}}{}^2}{m f_{\mathrm{m}}}.$$

This implies $\overline{P}_{\mathrm{ecr}} \rightarrow \infty$ as $f_{\mathrm{m}} \rightarrow 0$, and can only occur at exact resonance [1], p.501. The total power can be obtained by averaging Eq. (138) over the distribution of electrons, then integrating over the electron population near the resonance zone. First, substitute the relation for ω_{ce} near the resonance zone Eq. (99) in Eq. (138):

$$\overline{P}_{\mathrm{ecr}} = m\left(\frac{eE_{\mathrm{r}}}{m}\right)^2 \frac{f_{\mathrm{m}}}{f_{\mathrm{m}}{}^2 + (\omega\alpha\, z')^2}. \tag{139}$$

To integrate over the electron population near the resonance zone, multiply Eq. (139) by $n\,\mathrm{d}z$ and integrating from $z = -z_0$ to $z = z_0$, we have

$$\overline{S}_{\mathrm{ecr}} = \frac{2e^2 E_{\mathrm{r}}^2 n}{m\omega|\alpha|} \tan^{-1}\left(\frac{\omega|\alpha|z_0}{f_{\mathrm{m}}}\right). \tag{140}$$

Let $z_0 \rightarrow \infty$ to include all electron population in its distribution, we obtain the total power absorbed. When $z_0 \rightarrow \infty$, we have $\tan^{-1} \rightarrow \pi/2$ and the absorbed power in collisional heating Eq. (140) reduces to Eq. (127), the absorbed power for collisionless heating. As pointed out by Lieberman and Lichtenberg [1], p. 501, if we let $z_0 = \Delta z_{\mathrm{res}}$, the effective resonance zone width defined in Eq. (126), since $f_{\mathrm{m}} << \omega\alpha\,\Delta z_{\mathrm{res}}$, the equation reduces to the collisionless heating power, "almost all of the power is absorbed by collisionless heating within the resonance zone." which is the "usual regime" for ECR processing plasmas.

8 Conclusion

In this work, both theoretical and practical aspects for low pressure plasma modelling (via plasma global models) are discussed. The problems that this work were trying to solve are as follows:

1. Find the method of modelling heterogeneous surface processes and coupling the surface model to a classic plasma global model.

2. Successfully develop an SF_6/O_2 plasma global model with heterogeneous surface model, which should be capable of simulating a scenario that was only reported by experimental works: when small SF_6 (e.g. 5% in the feed composition) is added to a pure O_2 plasma's feedstock gas, there is a several times increase in the atomic oxygen density. Show that plasma global models still have their places when dealing with plasmas of fluorine containing gas and O_2 mixtures.

3. Propose the surface chemical kinetics for the SF_6/O_2 plasma. Reveal the mechanisms that govern the large increase in [O] as stated above.

4. Validate the model with published experimental works.

5. Investigate the fluctuations of a plasma model's outputs due to the statistical variations of the model's reaction rate coefficients.

6. Develop an ECR plasma global model with heterogeneous surface model.

In this PhD program, I developed the following models: I developed an SF_6 plasma global model with heterogeneous surface model, then expanded the method into the development of an O_2 plasma global model with heterogeneous surface model. An SF_6/O_2 plasma global model with heterogeneous surface model, which is the main focus of this work, was then developed based on the experience and knowledge obtained in developing the previous two models. I also developed an ECR SF_6 plasma global model with heterogeneous surface model, however, due to the fact that the model was not fully validated with experimental works, it's not shown in this thesis. Two papers are going to be published based on this work: Ref. [5] and Ref. [18].

To solve problem 1, I showed my efforts in finding the method of modelling heterogeneous surface processes and coupling the surface model to a classic plasma global model in chapter 2 and chapter 3. I showed how a surface coverage balance equation can be derived for a surface reaction in the transition state theory (chapter 3).

To solve problems 2, 3 and 4, I developed an SF_6/O_2 plasma global model with heterogeneous surface model. By validating the model with two experimental works (Kechkar *et al.* [10], sections 5.2 and 5.3; and Pessoa *et al.* [13], section 5.4), I have shown that as an important tool for plasma study, plasma global models still have their places when dealing with plasmas of fluorine containing gas and O_2 mixtures.

I proposed the surface chemical kinetics that govern the several times increase in atomic oxygen density when small SF_6 (e.g. 5% in the feed composition) is added to a pure O_2 plasma's feedstock gas (section 4.2). I found the chemisorptions of oxygen and fluorine's atomic and diatomic species almost dictate the profile of [O] and [F] with respect to the O_2 feed composition. I had three main findings regarding this scenario (section 5.1): (1) The reason for the above mentioned several times increase in [O] is due to a sharp decrease (a factor of 10^2 in my model) in the initial sticking coefficients of O and $O(^1D)$ chamber wall chemisorptions, plus a sharp increase (a factor of 10^2 in my model) in the initial sticking coefficients of O_2 and its excited species chamber wall chemisorptions when SF_6 is added to the pure O_2 plasma's feedstock gas, which effectively switches the main contribution channels of $O_{(s)}$ surface coverage from O and $O(^1D)$ chemisorptions (as in the pure O_2 plasma) to O_2 and its excited species chemisorptions (as in the SF_6/O_2 plasma). In an SF_6/O_2 plasma, comparing to a pure O_2 plasma, the smaller $O_{(s)}$ surface coverage reduces atomic O surface recombination, thus increases [O]. The atomic O produced by the enhanced abstractive adsorptions of the oxygen molecules in the SF_6/O_2 plasma further increases [O]. (2) The increase of O_2's gas-phase dissociation rate coefficient is not the reason for the above mentioned large increase in [O]. (3) The main surface loss channel of the atomic oxygen in O_2 and SF_6/O_2 plasmas is the O surface recombination.

As my models use the macroscopic initial sticking coefficients, the underlying reasons for the above mentioned initial sticking coefficient variations can not be revealed by my models. The most common explanation for the decrease in the initial sticking coefficients of O and O(^{1}D)'s chamber wall chemisorptions is that the surface sites that favourable to O and O(^{1}D) chemisorptions are either occupied by chemisorbed $F_{(s)}/SF_{5(s)}$ or being fluorinated [3], [10] (section 4.2.2). The fluoro-sulfur films (section 4.2.1) might have impact on O and O(^{1}D)'s initial sticking coefficients too. The reason for the increased O_2 and its excited species abstractive adsorptions is likely due to the surface defects introduced by the fluorination/oxidation processes or the fluoro-sulfur films generated by the SF_6 plasma surface processes. The gas temperature rise as reported in Kechkar *et al.*'s work [10] might play a role here too. (section 4.2.2)

I simulated the density variations of the two most important species in an SF_6/O_2 plasma: atomic O and atomic F as well as the above mentioned large [O] increase scenario (sections 5.2 to 5.4). There are three fundamental difficulties my models have to face: First, the electron energy distribution functions (EEDFs) vary with the gas mixture's composition, and can't be simply deemed as Maxwellian or Druyvesteyn [10] (see Figure 11). Second, the exact geometry of the plasma is not clear, it's either confined between the two electrodes [10], or diffuses to some extent to the chamber wall. Third, the chamber's internal geometry is not exactly cylindrical. The second problem was mitigated when validating the models with Pessoa *et al.*'s experimental work [13].

When taking the volume averaged [O] and [F] into account (section 5.3), the largest difference in [O] between my simulation and Kechkar *et al.*'s [10] experiment is by a factor of 2.24 (volume averaged [O] of Kechkar *et al.*'s work / [O] of Our Model) when there's 90% O_2 in the feed composition (section 5.3), and the minimum difference is by a factor of 1.14 when there's 100% O_2 in the feed composition; the largest difference in [F] between my simulation and Pessoa *et al.*'s [13] experiment is by a factor of 2.6 (Volume averaged [F] of Pessoa *et al.* / [F] in Our Model) when there's 100% SF_6 in the feed composition (section 5.4), and the minimum difference is by a factor of 0.91 when there's 90% O_2 in the feed composition. These results are quite reasonable for a global model. Averaging the difference factors in Table 14 for simulating Kechkar *et al.*'s work gives us 1.780; averaging the difference factors in Table 16 for simulating Pessoa *et al.*'s work gives us 0.970. The later simulation has an average difference factor much closer to 1, thus has much better correspondence to the experimental results. This is due to the fact that the plasma's volume was better defined in Pessoa *et al.*'s work [13] (Figure 17) compared to Kechkar *et al.*'s work [10] (Figure 10). In Pessoa *et al.*'s work, the plasma was approximately occupying the whole chamber, which is the same condition as in my model. In Kechkar *et al.*'s work, the volume of the plasma was not so clearly defined, which was more likely being confined between the two electrodes (as we have seen for the pure O_2 plasma model's results in Table 14), thus had no chamber wall along the radial direction. As we have seen that at the same input power and pressure, the atomic oxygen and atomic fluorine's densities are dictated by the surface conditions, therefore as the surface area in Pessoa *et al.*'s work is better agreed with my model, their atomic oxygen and atomic fluorine's densities should be better agreed with my model's results too.

A possible explanation for the differences in [O] of my model and the volume averaged [O] of Kechkar *et al.*'s experiment [10] is that the power coupled into the SF_6/O_2 plasma (when the SF_6 feed composition was non-zero) in the experiment was much higher than the value I used in my model (section 5.3.1). In the simulation for Pessoa *et al.*'s experiment, compare the simulated [F] with that of the experiment shown in Figure 18 we can see that in the experiment, the initial sticking coefficients of F and F_2's surface adsorptions gradually change with increasing O_2 feed composition, as oppose to a sharp 100 times decrease/increase as I have implemented in my model. They reach my proposed values at 40% O_2 feed composition and remain constant for higher O_2 feed compositions.

For all my simulations, I matched my model's simulated [e] values to that reported in the experiments due to the well known fact that the input power coupled into a CCP plasma is only a fraction of the total input power (section 5.2 and section 5.4). As the techniques for measuring electron density have been well established (Langmuir probe and hairpin probe were used in Kechkar *et al.*'s work [10]), I expect the electron density values reported by the experimental works are accurate.

To solve problem 5, I investigated the fluctuations of a plasma model's outputs due to the statistical variations of the model's reaction rate coefficients (chapter 6). By applying the method described in section 6.1 to my SF_6 plasma global model with heterogeneous surface model, and running the model for 1000 tims, each time with a different set of randomly generated rate coefficents for the selected electron-involving reactions, I found the uncertainties in the measured cross section data of the electron-involving reactions in my SF_6 plasma model with heterogeneous model won't cause a large fluctuation (such as a several-times increase in the density) in a species' density.

Problem 6 hasn't been fully solved, as the ECR plasma model hasn't been fully validated with experimental works. In this thesis, I showed a method to calculate the electron heating in an ECR discharge by following Lieberman and Lichtenberg's work [1] in chapter 7, which can be used as the corner stone for future works in this field. I have developed an SF_6 plasma global model with heterogeneous surface model for ECR plasma discharge. However, this model hasn't be validated with experimental works, therefore it's not discussed in this thesis. Future works will be devoted to the validation of this model.

The reaction probability $S_0(T)$ of a surface reaction is a tricky quantity. From my derivation in chapter 3 we can see it is temperature dependent, and is a function of the activation energy E_a, and is proportional to the ratio of the reactants' partition functions in transition state and gas phase. In practice, the reaction probability $S_0(T)$ can be measured experimentally. As stated by Kolasinski [35]: “the study of sticking coefficients (another name of $S_0(T)$) and their dependence on various experimental parameters is itself a study of the validity of CTST (classic transition state theory) and its corrections” (Ref. [35], page 230). On the other hand, ΔE (or The activation energy E_a, see Appendix A.1) can be calculated from PES (potential energy surface) analysis, or obtained from experiments (Ref. [36], page 6). These two quantities are essential to surface process modelling. Future works can also be devoted to this field.

Appendix A Concepts in Statistical Thermodynamics

A.1 Arrhenius Equation

A commonly accepted expression [36] for the rate coefficient of an elementary reaction [8] is described by **Arrhenius equation**:

$$k(T) = v\mathrm{e}^{-E_\mathrm{a}/RT} \tag{141}$$

where v is the **pre-exponential factor** or the **frequency factor**, E_a is the activation energy in kJ mol^{-1}. When E_a is in the unit of Joules per particle, Eq. (141) can be written as

$$k(T) = v\mathrm{e}^{-E_\mathrm{a}/k_\mathrm{B}T} \tag{142}$$

where k_B is Boltzmann's constant. As we will see later in the transition state theory, v can have a “weakly” [36] temperature dependence.

Arrhenius equation is a good demonstration on how reactions occur (Figure 26). In Figure 26, the reaction between two particles A and B will occur only if their potential energy with respect to each other are higher than the energy barrier ΔE at the moment of their collision. This simple, yet important picture is the basis of the reaction rate theory. Generally, higher activation energy corresponds to stronger temperature dependence of the reaction rate coefficient. A reaction with zero activation energy will have its rate coefficient independent of temperature [66], p.808. In the transition state theory, the activation energy E_a is the same as the potential energy barrier ΔE [66], p.809.

---

[8] An elementary reaction in chemistry is a reaction that occurs in a non-dividable single step, i.e. no substeps involved.

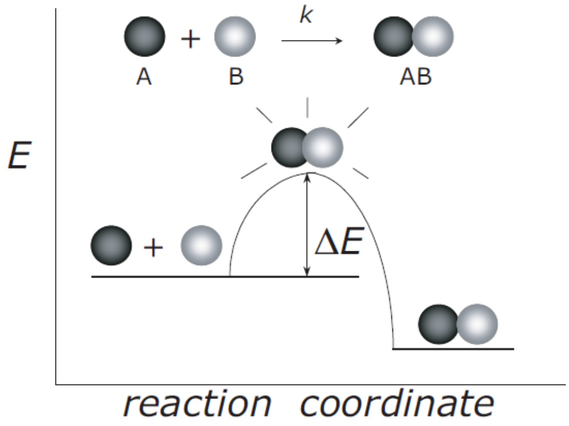

Figure 26 Demonstration on how chemical reactions occur.
In terms of surface reactions, the reaction coordinate is usually the vibration of the gaseous particle at the surface. (From Ref. [27], page 80)

Nowadays, the activation energies can be calculated from PES (potential energy surface) analysis (see, for example, Ref. [36], chapter 1), however the detailed discussion is beyond the scope of this work.

A.2 Partition Function

Partition function is an important concept in statistical thermodynamics. In transition state theory, collision is not the only event that plays a role to excite the reacting particles to the “transition state”, the vibration and rotation modes of the reacting particles also do so. The reaction then occurs at this transition state.

The Boltzmann distribution can be written as (Ref. [66], section 16.2)

$$p_i = \frac{n_i}{N} = \frac{\mathrm{e}^{-\beta \varepsilon_i}}{q} \tag{143}$$

where p_i is the fraction of molecules in the state i (or the probability of finding a molecule with energy state ε_i), $p_i = n_i / N$. N is the number of molecules in the system, n_i is the number of molecules in state i. For Boltzmann distribution, we have

$$\beta = \frac{1}{k_{\mathrm{B}}T} \tag{144}$$

where $k_{\mathrm{B}} = 1.381 \times 10^{-23}$ J/K is the Boltzmann constant, T is the absolute temperature in kelvin. q is the molecular partition function, which can be written in a general form as

$$q = \sum_j \mathrm{e}^{-\beta\varepsilon_j} \tag{145}$$

where j is the total number of states. Or equivalently, we can write the partition function in energy levels, where a group of states with the same energy form an energy level (now j is the total number of the energy levels). If energy level j has g_j states of the same energy ε_j, in which case we say energy level j is **g_j -fold degenerate**, the partition function can be written as:

$$q = \sum_{\text{levels } j} g_j \mathrm{e}^{-\beta\varepsilon_j} \tag{146}$$

Essentially, partition function is an indication of the number of accessible energy states that *one single* particle can have at a certain temperature T. From the definition of the partition function [Eq. (146)] we can see that when $T \to 0$, $\beta \to \infty$, $\exp(-\beta\varepsilon_j) \to 0$ except for $\varepsilon_0 = 0$, $\exp(-\beta\varepsilon_j) = 1$ so in this case, $q = g_0$, the degeneracy of the ground state of the particle, which is the number of accessible energy states at $T = 0$. In the other extreme, when $T \to \infty$, $\beta \to 0$, $\exp(-\beta\varepsilon_j) \to 1$, from Eq. (146), $q = g_0 + g_1 + \ldots\ldots = \infty$, which is the number of accessible energy states at infinitely high temperature.

Partition function is an important concept in statistical thermodynamics. It plays a role analogous to that of Schrödinger equation in quantum mechanics. As soon as a particle's partition function is known to us, we can obtain all thermodynamic quantities from it.

One example is the average energy of a particle. In general, the average energy of a collection of N particles can be written as

$$\bar{\varepsilon} = \frac{E_{tot}}{N} = \frac{\varepsilon_0 n_0 + \varepsilon_1 n_1 + \ldots\ldots}{N} = \varepsilon_0 p_0 + \varepsilon_1 p_1 + \ldots\ldots$$

where ε_i, i = 0, 1, 2, ... is the energy of particle in each state i. E_{tot} is the total energy these N particles possess. Substitute Eq. (143) into the above equation, we have

$$\bar{\varepsilon} = \frac{\varepsilon_0 \mathrm{e}^{-\varepsilon_0/k_\mathrm{B}T}}{q} + \frac{\varepsilon_1 \mathrm{e}^{-\varepsilon_1/k_\mathrm{B}T}}{q} + \ldots\ldots = \frac{\sum\limits_{i=0}^{\infty} \varepsilon_i \mathrm{e}^{-\varepsilon_i/k_\mathrm{B}T}}{q}$$

$$= k_\mathrm{B}T^2 \frac{1}{q} \sum_{i=0}^{\infty} \frac{\varepsilon_i}{k_\mathrm{B}T^2} \mathrm{e}^{-\varepsilon_i/k_\mathrm{B}T}$$

by recognizing that $\sum\limits_{i=0}^{\infty} \frac{\varepsilon_i}{k_\mathrm{B}T^2} \mathrm{e}^{-\varepsilon_i/k_\mathrm{B}T} = \frac{\partial q}{\partial T}$ (see Eq. (145)), we can write the above equation as

$$\bar{\varepsilon} = k_\mathrm{B}T^2 \frac{1}{q} \frac{\partial q}{\partial T}$$

but $\frac{1}{q} \frac{\partial q}{\partial T} = \frac{\partial \ln q}{\partial T}$, therefore

$$\bar{\varepsilon} = k_\mathrm{B}T^2 \frac{\partial \ln q}{\partial T} \tag{147}$$

Eq. (147) represents any kinds of energy a particle can possess. E.g. when q is the translational partition function, Eq. (147) gives the average kinetic energy of a particle.

Two important models are worthwhile mentioning for our latter discussion: one is the two-level system model, the other is the infinite ladder model. The first model is a good demonstration that the partition function is a indicator of number of accessible energy states for a particle. The second model is the case for a simple harmonic oscillator, which can be considered as the approximated vibration mode of a molecule.

Let's first take a look at the two-level system model. A typical example of a two-level system is an electron in a magnetic field. The electron have two possible spin magnetic quantum numbers: m_s = ±1/2, which correspond to two spin orientation: parallel or anti-parallel to the magnetic field. We let the particle's ground state energy to be $\varepsilon_0 = 0$, and its excited state energy to be $\Delta\varepsilon$, the partition function can be obtained from Eq. (146)

$$q = \sum_{i=0,1} g_i \mathrm{e}^{-\beta\varepsilon_i}$$

with $g_0 = g_1 = 1$, we have

$$q = e^{-\varepsilon_0/k_B T} + e^{-\Delta\varepsilon/k_B T} = 1 + e^{-\Delta\varepsilon/k_B T} \qquad (148)$$

We can see that q has the value of 1 when $T \rightarrow 0$, which agrees with our expectation that at low temperatures, the system is in its ground state and $q = g_0$. When T is high, $q = 2$. Both levels are equally occupied. This agrees with the thermodynamics result that only ground energy state of a particle is occupied at $T = 0$; more energy states are accessible when T is increased; when $T = \infty$, all possible states are equally populated (Ref. [66] "Molecular interpretation 3.1"). The state occupation and temperature relationship is shown in Figure 27.

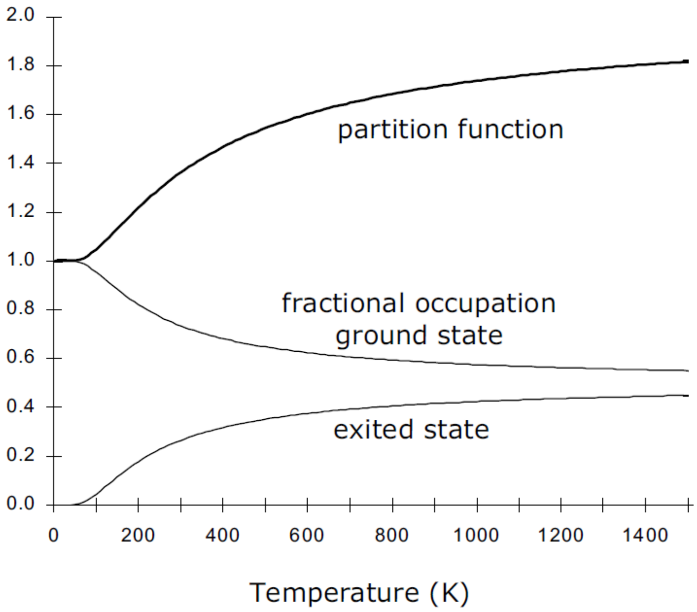

Figure 27 Partition function vs. temperature for a two-level system.
As T increases, the ground state and excited state are equally possibly occupied (the "fractional occupation" of both states approach 0.5) (figure from Ref. [27], page 82)

Now lets take a look at the infinite ladder model. This is a model of particle with infinite energy states each separated by the same energy $\Delta\varepsilon$, each energy level is monodegenerated. The partition function can be obtained from Eq. (145).

$$q=\sum_i \mathrm{e}^{-\beta\varepsilon_i}=1+\mathrm{e}^{-\frac{1}{k_\mathrm{B}T}\Delta\varepsilon}+\mathrm{e}^{-\frac{1}{k_\mathrm{B}T}2\Delta\varepsilon}+\mathrm{e}^{-\frac{1}{k_\mathrm{B}T}3\Delta\varepsilon}+\ldots\ldots$$

but we have

$$1+\mathrm{e}^{-1}+\mathrm{e}^{-2}+\ldots.+\mathrm{e}^{-i}=\frac{1}{1-\mathrm{e}^{-1}}$$

so the above equation can be written as

$$q=\frac{1}{1-\mathrm{e}^{-\frac{1}{k_\mathrm{B}T}\Delta\varepsilon}} \tag{149}$$

when $T \to 0$, the exponential term approaches 0, and $q = 1$; when $T \to \infty$, $-\beta\Delta\varepsilon \to 0$, the exponential term approaches 1, and $q = \infty$.

A.3 Partition Functions of Various Degrees of Freedom

As a partition function is an indication of the number of accessible energy states of a particle, different degrees of freedom contribute to the number of total accessible energy states, so we can naturally conclude that the overall partition function of a particle is the product of the partition functions of various degrees of freedom. This can be mathematically demonstrated as follows: suppose the total energy of a particle arises from three degrees of freedom, the total energy of the particle is

$$E_\mathrm{tot} = E_a + E_b + E_c$$

where E_a, E_b, E_c are the energy associated to each degree of freedom. The particle's total partition function can be obtained from Eq. (145) as

$$q_\mathrm{tot}=\sum_i \mathrm{e}^{-\beta(E_a+E_b+E_c)_i}=\sum_{i_c}\sum_{i_b}\sum_{i_a}\mathrm{e}^{-\beta E_{i_a}}\mathrm{e}^{-\beta E_{i_b}}\mathrm{e}^{-\beta E_{i_c}}$$

$$= \left(\sum_{i_a} \mathrm{e}^{-\beta E_{i_a}} \right) \left(\sum_{i_b} \mathrm{e}^{-\beta E_{i_b}} \right) \left(\sum_{i_c} \mathrm{e}^{-\beta E_{i_c}} \right) = q_a q_b q_c \tag{150}$$

which proves my statement at the beginning of this section that the overall partition function of a particle is the product of the partition functions of various degrees of freedom.

For atoms, the total partition function can be written as

$$q = q_{\mathrm{trans}}\, q_{\mathrm{elec}}\, q_{\mathrm{nucl}} \tag{151}$$

where q_{trans} is the translation partition function arising from the translational freedom; q_{elec} and q_{nucl} are the electronic and nuclear partition functions related to electrons and nuclei. For molecules, there are two additional degrees of freedom: rotation and vibration, so the partition function for a molecule is

$$q = q_{\mathrm{trans}}\, q_{\mathrm{rot}}\, q_{\mathrm{vib}}\, q_{\mathrm{elec}}\, q_{\mathrm{nucl}} \tag{152}$$

where q_{rot} and q_{vib} are the rotational and vibrational partition functions respectively.

In this section, I'm going to derive the partition functions for various degrees of freedom. We are going to see that these partition functions are necessary for the derivation of the rate coefficients of surface reactions in transition state theory.

A.3.1 Translational Partition Function

The translational partition function of a particle is obtained from an **infinite square well model** (a more detailed discussion can be found in Ref. [67] section 2.2 for the infinite square well model) or **particle in box model**. The model assumes a potential

$$V(x) = \begin{cases} 0, & \text{if } 0 < x < l \\ \infty, & \text{otherwise} \end{cases} \tag{153}$$

where l is the length of the well. In this model, a particle is free to move along the x axis, except at $x = 0$ and $x = l$, the infinite potentials exert infinite forces on the particle to prevent it from escaping from the well. It can also be approximated to a scenario that a particle bounces back and forth forever in a one-dimensional track of length l.

The time independent Schrödinger equation inside the well (where $V = 0$) is

$$-\frac{\hbar^2}{2m}\frac{d^2\psi}{dx^2} = E\psi \tag{154}$$

where E is the possible energy levels of the molecule (for simplicity purpose I assume ψ is time-independent). Rearrange we have

$$\frac{d^2\psi}{dx^2} = -k^2\psi \text{, where } k = \frac{\sqrt{2mE}}{\hbar} \tag{155}$$

We recognise Eq. (155) is a simple harmonic oscillator with a solution of

$$\psi(x) = A \sin kx + B \cos kx \tag{156}$$

where A and B are arbitrary constants. As the probability of finding the particle at $x = 0$ and $x = l$ is zero, we have

$$\psi(0) = A \sin 0 + B \cos 0 = 0$$
$$\psi(l) = A \sin kl + B \cos kl = 0$$

From the first equation, we get $B = 0$. From the second equation, we have

$$A \sin kl = 0$$

As A can not be 0, otherwise ψ is 0 for all x, so we have $\sin kl = 0$, which leads to

$$kl = n\pi, \qquad \text{where } n = 1, 2, \ldots$$

here n can not be zero because $n = 0$ makes $k = 0$, which in turn makes ψ equal to 0 for all x; n can as well be negative, but as $\sin(-x) = -\sin(x)$, we can let A absorb the minus sign. We now have the value of k:

$$k = \frac{n\pi}{l}, \text{ where } n = 1, 2, \ldots \tag{157}$$

From Eq. (155) we have $k = (2mE)^{1/2}/\hbar$, substitute Eq. (157) into it, we get the value of E (because E is quantized by n, so I write it as E_n here):

$$E_n = \frac{n^2\pi^2\hbar^2}{2ml^2} = \frac{n^2h^2}{8ml^2}, \text{ where } n = 1, 2, \ldots \tag{158}$$

(where $\hbar = h/2\pi$) I take the ground state $n = 1$ as the lowest energy level, which is

$$\varepsilon_1 = h^2/8ml^2.$$

Denote the energy levels relative to the ground state as ε_n, we have

$$\varepsilon_n = E_n - \varepsilon_1 = \frac{n^2h^2}{8ml^2} - \frac{h^2}{8ml^2} = (n^2 - 1)\varepsilon_1 \tag{159}$$

Substitute Eq. (159) to Eq. (145) $q = \sum_i \mathrm{e}^{-\beta\varepsilon_i}$, we have

$$q_{\text{trans-1D}} = \sum_{n=1}^{\infty} \mathrm{e}^{-\beta\varepsilon_n}$$

At room temperature, particles in a laboratory container have very close translational energy levels such that the sum can be approximated by an integral (Ref. [66], page 569), also note that for large n, $n^2 - 1 \approx n^2$, we have

$$q_{\text{trans-1D}} = \sum_{n=1}^{\infty} \mathrm{e}^{-(n^2-1)\varepsilon_1\beta} \approx \int_1^{\infty} \mathrm{e}^{-(n^2-1)\varepsilon_1\beta} dn \approx \int_0^{\infty} \mathrm{e}^{-n^2\varepsilon_1\beta} dn$$

Let $x^2 = n^2\varepsilon_1\beta$, then $dn = (1/\varepsilon_1\beta)^{1/2}dx$, replace n by x, we have

$$q_{\text{trans-1D}} = \frac{1}{\sqrt{\varepsilon_1\beta}} \int_0^{\infty} \mathrm{e}^{-x^2} dx$$

The integration is the Gaussian integral,

$$\int_0^\infty e^{-ax^2} dx = \frac{1}{2}\sqrt{\frac{\pi}{a}} \tag{160}$$

therefore we have

$$q_{\text{trans-1D}} = \frac{1}{2}\sqrt{\frac{\pi}{\varepsilon\beta}} = \sqrt{\frac{2k_{\text{B}}Tml^2\pi}{h^2}} = \frac{l\sqrt{2\pi k_{\text{B}}mT}}{h} \tag{161}$$

If we assume the motion in each dimension is separable, we can readily have partition functions of a particle travelling on a surface and in a volume, based on Eq. (150):

$$q_{\text{trans-2D}} = A\frac{2\pi k_{\text{B}}mT}{h^2} \tag{162}$$

$$q_{\text{trans-3D}} = V\frac{(2\pi k_{\text{B}}mT)^{3/2}}{h^3} \tag{163}$$

where A and V are the area and volume in which the particle travels. Translational partition functions normally have large values.

Eq. (163) can also be written as

$$q_{\text{trans-3D}} = \frac{V}{\Lambda^3} \tag{164}$$

where $\Lambda = h/(2\pi mk_{\text{B}}T)^{1/2}$, is the **thermal wavelength** of the particle in one dimension. At 25°C, Λ = 71 pm for H_2, 18 pm for O_2 (Ref. [66], page 622). Our derivation of the translational partition function for the Boltzmann distribution only valid when $V/\Lambda^3 >> 1$, which, by the meaning of a partition function, requires that the particle has many accessible energy states at the temperature concerns us. It also means that the wavelength of the particle has to be small compared with the dimension of the container. Fortunately, most systems we shall encounter will fulfil this condition, the condition is only breached at extreme situations (where either Bose-Einstein or Fermi-Dirac statistics need to be applied) such as at very low temperatures (i.e. for the super fluid state He at a few K) or very high pressures as in stars (Ref. [27], page 89).

As I have mentioned in section A.2, when the translational partition function is inserted in Eq. (147), we get the average kinetic energy of a particle. To see this, we insert Eq. (163) into Eq. (147) to get

$$\bar{\varepsilon}_{\text{trans}} = k_B T^2 \frac{\partial \ln q}{\partial T} = k_B T^2 \frac{d}{dT} \ln\left[V \frac{(2\pi m k_B T)^{3/2}}{h^3} \right] = \frac{3}{2} k_B T \qquad (165)$$

A.3.2 Vibrational Partition Function

Zero-point Energy (ZPE)

Before we talk about the vibrational partition functions, we need to introduce a concept, the zero-point energy (ZPE). As stated by Arnaut *et. al.* (Ref. [36], page 133.), the ZPE corresponds to the lowest quantized energy mode in quantum mechanics (the ground state). All the energy levels are measured with respect to the ZPE, and thus the ground state energy is 0. As we will see in the transition state theory, the location of the ZPE is sometimes raised to the level of the potential energy barrier of a chemical reaction. ▲

The internal freedom of molecules give rise to vibrational and rotational partition functions. Vibrations are important for surface reactions in the sense that they play the roles of the reaction coordinate. The vibrational motion of a molecule can be approximated as harmonic oscillation if the vibrational excitation is not too great (Ref. [66], page 626).

If the zero-point (potential) energy is taken to be below the ground state of vibration (the absolute zero energy level), the vibrational energy levels of a harmonic oscillator (the total energy within a harmonic oscillator at energy level i, or the **energy of a harmonic oscillator**, with the ground state energy $\varepsilon_0 = 1/2hv$, which is non-zero) is given by (interested readers can refer to Ref. [66], section 13.9)

$$\varepsilon_i = \left(i + \frac{1}{2} \right) h\nu \text{ , } i = 0, 1, 2 \ldots \tag{166}$$

where ν is the frequency of the oscillator. The partition function can be written as

$$q_{\text{vib}} = \sum_i \mathrm{e}^{-\beta\varepsilon_i} = \sum_i \mathrm{e}^{-(i+\frac{1}{2})\beta h\nu} = \mathrm{e}^{-\frac{h\nu}{2k_{\mathrm{B}}T}} \sum_i \mathrm{e}^{-i\beta h\nu} = \frac{\mathrm{e}^{-\frac{h\nu}{2k_{\mathrm{B}}T}}}{1-\mathrm{e}^{-h\nu/k_{\mathrm{B}}T}} \tag{167}$$

On the other hand, if the zero-point energy (ZPE) is set to be at the ground state of vibration (this will make $\varepsilon_0 = 0$), as partition functions are usually given with respect to the lowest occupied state (Ref. [27], page 89), we need to subtract ε_0 from Eq. (166):

$$\varepsilon_i = \left(i + \frac{1}{2} \right) h\nu - \frac{1}{2} h\nu = ih\nu \text{ , } i = 0, 1, 2 \ldots \tag{168}$$

Now we can write the partition function as

$$q_{\text{vib}} = \sum_i \mathrm{e}^{-\beta\varepsilon_i} = \sum_i \mathrm{e}^{-i\beta h\nu} = \frac{1}{1-\mathrm{e}^{-h\nu/k_{\mathrm{B}}T}} \tag{169}$$

which is the same result as we got for the infinite ladder model in Eq. (149).

If we raise the ZPE a further ΔE (e.g., ΔE could be the potential barrier in chemical reactions), the maximum potential energy levels of the harmonic oscillator is:

$$\varepsilon_i = \left(i + \frac{1}{2} \right) h\nu - \frac{1}{2} h\nu - \Delta E = ih\nu - \Delta E \text{ , } i = 0, 1, 2 \ldots$$

and now the partition function is:

$$q_{\text{vib}} = \sum_i \mathrm{e}^{-\beta\varepsilon_i} = \mathrm{e}^{-\beta\Delta E} \sum_i \mathrm{e}^{-i\beta h\nu} = \frac{1}{1-\mathrm{e}^{-h\nu/k_{\mathrm{B}}T}} \mathrm{e}^{-\frac{\Delta E}{k_{\mathrm{B}}T}} \tag{170}$$

Both Eq. (169) and Eq. (170) will be used in our latter discussion. q_{vib} obtained from Eq. (169) is often close to 1, except when the vibrational frequency is low, and approaches the **classical limit** $h\nu << k_{\mathrm{B}}T$ [also see below Eq. (179)] and we can have the approximation that

$$e^{\pm x} \approx 1 \pm x \,,$$

such that

$$e^{-h\nu/k_\mathrm{B}T} \approx 1 - h\nu/k_\mathrm{B}T \quad \text{(when } h\nu/k_\mathrm{B}T << 1\text{)},$$

(Ref. [27], page 90). The partition function in Eq. (169) can be written as

$$q_\mathrm{vib} = \frac{1}{1-e^{-h\nu/k_\mathrm{B}T}} \approx \frac{1}{1-1+h\nu/k_\mathrm{B}T} = \frac{k_\mathrm{B}T}{h\nu} \tag{171}$$

We have seen that when a molecule is adsorbed on a surface, it has several different vibration modes, each with its own partition function and some of which with low frequencies, and becomes the reaction coordinate that leads to the product (Ref. [27], page 90; Ref. [36], page 264; Ref. [35], page 221). The total vibrational partition function becomes the product of the partition function of each vibration mode (use Eq.(167)).

$$q_\mathrm{vib} = \prod_m \frac{e^{-\frac{h\nu_m}{2k_\mathrm{B}T}}}{1-e^{-h\nu_m/k_\mathrm{B}T}} \tag{172}$$

where ν_m is the frequency of each vibration mode.

We can now use the partition function obtained in Eq. (172) to calculate the average vibrational energy just as we did at the end of section A.3.1. Insert Eq. (172) into Eq. (147), we have

$$\bar{\varepsilon}_\mathrm{vib} = k_\mathrm{B}T^2 \frac{\partial \ln q}{\partial T} = k_\mathrm{B}T^2 \frac{\partial}{\partial T} \ln\left[\prod_m \frac{e^{-\frac{h\nu_m}{2k_\mathrm{B}T}}}{1-e^{-h\nu_m/k_\mathrm{B}T}}\right]$$

By noticing that $\ln(\Pi x_i) = \Sigma(\ln x_i)$, we have

$$\bar{\varepsilon}_{\text{vib}} = k_{\text{B}}T^2 \frac{\partial}{\partial T}\sum_m \ln \frac{\mathrm{e}^{-\frac{h\nu_m}{2k_{\text{B}}T}}}{1-\mathrm{e}^{-h\nu_m/k_{\text{B}}T}}$$

$$= k_{\text{B}}T^2 \sum_m \left(\frac{\partial}{\partial T} \ln \frac{\mathrm{e}^{-\frac{h\nu_m}{2k_{\text{B}}T}}}{1-\mathrm{e}^{-h\nu_m/k_{\text{B}}T}} \right)$$

$$= k_{\text{B}}T^2 \sum_m \left[\frac{\partial}{\partial T} \left(\ln \mathrm{e}^{-\frac{h\nu_m}{2k_{\text{B}}T}} - \ln\left(1-\mathrm{e}^{-h\nu_m/k_{\text{B}}T}\right) \right) \right]$$

$$\approx k_{\text{B}}T^2 \sum_m \left[\frac{\partial}{\partial T} \left(-\frac{h\nu_m}{2k_{\text{B}}T} - \ln(1-0) \right) \right]$$ (for not-too-low vibration frequency, i.e. $h\nu$ is reasonably larger than $k_{\text{B}}T$, $\mathrm{e}^{-h\nu/k_BT} \approx 0$, e.g. for $\mathrm{e}^{-6.3} = 0.002$)

$$= k_{\text{B}}T^2 \sum_m \left[\frac{h\nu_m}{2k_{\text{B}}T^2} \right] = \sum_m \left[\frac{1}{2} h\nu_m \right] \tag{173}$$

As seen in the derivation, Eq. (173) is valid for all vibration modes with a not-too-low frequency.

A.3.3 Rotational Partition Function

We now take a look at the rotational partition function for a diatomic molecule. The rotational energy level for such a molecule can be obtained from

$$\varepsilon_l = \frac{l(l+1)h^2}{8\pi^2 I} \tag{174}$$

we measure the energy with respect to the ground state (such that $\varepsilon_0 = 0$). In the above equation, l is the rotational quantum number, and I is the **moment of inertia** around one rotation axis, which is defined as the sum of the product of each atom's mass and the square of the distance from the atom's centre of mass to the rotation axis. The rotation axis has to pass through the molecule's centre of mass. (Ref. [66], section 13.4)

$$I = \sum_i m_i r_i^2 \tag{175}$$

where r_i is the perpendicular distance from atom i's centre of mass to the molecule's one axis of rotation. Each axis of rotation has an I value associated to it. It is a convention to use three mutually perpendicular rotation axes to express the moments of inertia of a molecule, such that the three moments of inertia associated to the three rotation axes have the relation $I_c \geq I_b \geq I_a$. (Figure 28)

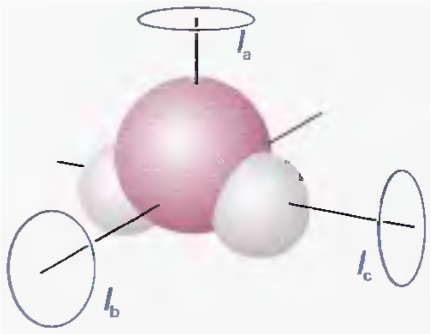

Figure 28 An asymmetric rotor has three different moments of inertia. (figure from Ref. [66], page 441)

For a diatomic atom, we can write

$$I = \mu r^2 \tag{176}$$

with μ the reduced mass and r the distance from the point mass μ to the axis of rotation. The reduced mass μ is defined as

$$\frac{1}{\mu} = \frac{1}{m_1} + \frac{1}{m_2} \tag{177}$$

where m_1 and m_2 are the masses of the atoms in the diatomic molecule.

Now the partition function can be written as (with the degeneracy of rotation levels $2l + 1$ and the symmetry factor σ in account)

$$q_{\mathrm{rot}} = \sum_l \mathrm{e}^{-\beta\varepsilon_l} = \frac{1}{\sigma}\sum_{l=0}^{\infty}(2l+1)\mathrm{e}^{-\frac{l(l+1)h^2}{8\pi^2 I k_{\mathrm{B}} T}}. \tag{178}$$

If $h^2/8\pi^2 I << k_{\mathrm{B}}T$ (i.e., the rotational energy separations between the levels are much smaller than $k_{\mathrm{B}}T$, see Ref. [36], page 149), the sum can be replaced by an integral (Ref. [68], page 357).

$$q_{\mathrm{rot}} = \frac{1}{\sigma}\int_0^{\infty}(2l+1)\mathrm{e}^{-\frac{l(l+1)h^2}{8\pi^2 I k_{\mathrm{B}} T}}dl.$$

Let $x = l(l + 1)$, and $dx/dl = 2l + 1 \rightarrow dx = (2l + 1)\, dl$, and the above equation can be written as

$$\begin{aligned} q_{\mathrm{rot}} &= \frac{1}{\sigma}\int_0^{\infty}\mathrm{e}^{-\frac{xh^2}{8\pi^2 I k_{\mathrm{B}} T}}dx \\ &= \frac{1}{\sigma}\frac{8\pi^2 I k_{\mathrm{B}} T}{h^2} \quad \text{for } k_{\mathrm{B}}T >> \frac{h^2}{8\pi^2 I}. \end{aligned} \tag{179}$$

Here we introduced a classical limit, which is valid above a certain (practically low) critical temperature (e.g., 85 K for H_2, 3 K for CO) (Ref. [27], page 91). If $k_{\mathrm{B}}T$ is less than or in the order of $h^2/8\pi^2 I$ (which means at these values of l, the energy separation is larger than or in the order of $k_{\mathrm{B}}T$), one practical treatment (Ref. [68], page 357) is to calculate the first few terms of the sum in Eq. (178), until we reach a value of $l = l'$ such that $l'(l' + 1) >> k_{\mathrm{B}}T$, which is to pick out the values for energy levels with separations larger than or in the order of $k_{\mathrm{B}}T$, and integrate the remaining terms from l' to infinity. In Eq. (179) σ is the symmetry factor [27].

Again, I give the average rotational energy here (for $k_{\mathrm{B}}T >> \dfrac{h^2}{8\pi^2 I}$).

$$\begin{aligned} \bar{\varepsilon}_{\mathrm{rot}} &= k_{\mathrm{B}}T^2\frac{\partial}{\partial T}\ln\left(\frac{1}{\sigma}\frac{8\pi^2 I k_{\mathrm{B}}}{h^2}T\right) \\ &= k_{\mathrm{B}}T^2\left[\frac{\partial}{\partial T}\ln\left(\frac{1}{\sigma}\frac{8\pi^2 I k_{\mathrm{B}}}{h^2}\right) + \frac{\partial}{\partial T}\ln T\right] \end{aligned}$$

$$= k_{\mathrm{B}} T^2 \left[0 + \frac{\partial}{\partial T} \ln T \right] = k_{\mathrm{B}} T \tag{180}$$

The general form of rotational partition function is (Ref. [27], page 91)

$$q_{\mathrm{rot}} = \frac{1}{\sigma} \left(\frac{8\pi^2 k_{\mathrm{B}} T}{h^2} \right)^{\frac{3}{2}} \sqrt{\pi I_a I_b I_c} \tag{181}$$

where I_a, I_b, I_c are defined above Figure 28.

A.3.4 Electronic and Nuclear Partition Functions

I now follow the discussion in Ref. [69] section 5-2 to have an insight of the electronic and nuclear partition functions.

We now use Eq. (146) to write the electronic partition function as

$$q_{\mathrm{elec}} = \sum_{\text{levels } i} g_i \mathrm{e}^{-\beta \varepsilon_i} , \tag{182}$$

where g_i is the degeneracy of energy level i, ε_i is the energy of the ith electronic energy level. We measure the electronic energy with respect to the ground state, such that $\varepsilon_1 = 0$. We denote all the other energy levels measured relative to the ground state as $\Delta\varepsilon_{11}$, $\Delta\varepsilon_{12}$, ... Now we can write the electronic partition function as

$$q_{\mathrm{elec}} = g_1 + g_2 \mathrm{e}^{-\beta \Delta\varepsilon_{12}} + \ldots \tag{183}$$

$\Delta\varepsilon_{13}$, $\Delta\varepsilon_{14}$, ... are usually of the order of electron volts, and the value of $\beta\Delta\varepsilon$ is quite large at room temperature, which makes the sum of the terms from the second term onwards in Eq. (183) very close to 0. Therefore, at room temperature, $q_{\mathrm{elec}} \approx g_1$ for such cases. There are still exceptions. For halogen atoms, the energy of the first excited state is only a fraction of an electron volt higher than the ground state, so more terms in Eq.

(183) are needed to calculate q_{elec}, but still, the sum converges extremely fast in these cases. (Ref. [69], page 83)

The nuclear partition function can usually be taken as 1. Because nuclear energy levels are separated by millions of electron volts, we have to have a temperature of 10^{10} K to produce excited nuclei. Therefore $q_{\text{necl}} = g_1$, the degeneracy of the ground nuclear state. For all the chemical processes we shall encounter in this work, we can safely assume the particles' nuclear states won't change, and exclude the nuclear partition functions from our calculation.

A.4 Canonical Ensemble

In statistical thermodynamics, ensemble methods are used to describe the behaviour of large number of molecules. Statistical thermodynamics concentrates on the average behaviour of bulk matter, whereas quantum mechanics describes the properties of individual molecules. In this section, I follow Atkins and Paula's work (Chapter 16 of Ref. [66]) to briefly introduce the canonical ensemble concept, which is used to derive the surface reaction rate coefficient in the transition state theory.

A closed system [9] with n particles can be imaginarily replicated $\tilde{N}$ times to form a isolated canonical ensemble. We assume these $\tilde{N}$ closed systems can exchange energy with each other, and they are in thermal equilibrium with each other, so they all have the same temperature T. In other words, n, V, T are constants for each of the constituent closed systems of the ensemble. As the replicated systems can exchange energy with each other through heat, they do not all have the same energy, even they have the same temperature. At certain T, the energy distribution of the particles won't change, thus the energy population of the particles in the canonical ensemble will be constant, i.e., on average, there are n_0 particles in the ensemble in energy state ε_0, n_1 particles in energy ε_1, ..., but the energy state of each particle can change due to collisions (see Ref. [36], Appendix II). "This imaginary collection of replications of the actual system with a

---

[9] As defined in Ref. [66], page 28, an open system can exchange matter and energy with its surroundings; a closed system can exchange energy but not matter with its surroundings; an isolated system can change neither mass nor energy with its surroundings.

common temperature is called the **canonical ensemble**” (Ref. [66], page 577). We introduce the ensemble concept to describe a system of interacting particles. The total energy of all the systems is a constant $\tilde{E}$ because the whole ensemble is isolated. Let $\tilde{n}_i$ denote the number of *systems* of the canonical ensemble having energy E_i. The probability that $\tilde{n}_i$ systems having energy E_i is:

$$\frac{\tilde{n}_i}{\tilde{N}} = \frac{\mathrm{e}^{-\beta E_i}}{Q} \tag{184}$$

where

$$Q = \sum_j \mathrm{e}^{-\beta E_j} \tag{185}$$

Is the **canonical partition function**. It's worthwhile mentioning that as oppose to the molecular partition function, the canonical partition function indicates the number of accessible energy states of a *collection* of particles [i.e. the system for which the canonical ensemble is created, therefore the more duplicated systems we have (i.e. the larger $\tilde{N}$) the better chance we observe all possible energy states of a system].

Now assume we have a system with N particles of the same species. If the particles in the system are **distinguishable** [as in the case for the constituent particles of a crystalline material (Ref. [70], page 30)], the total energy of the system in energy state i is

$$E_i = \varepsilon_i(1) + \varepsilon_i(2) + \ldots + \varepsilon_i(N)$$

where $\varepsilon_i(1)$, $\varepsilon_i(2)$, ..., $\varepsilon_i(N)$ are the energies of molecule 1, 2, ..., N when the system is in energy state i. The canonical partition function then follows Eq. (185):

$$Q = \sum_j \mathrm{e}^{-\beta\varepsilon_j(1) - \beta\varepsilon_j(2) - \ldots - \beta\varepsilon_j(N)}$$

We can equally sum over all possible states j for individual molecules, and have:

$$Q=\sum_j \mathrm{e}^{-\beta\varepsilon_j}\sum_j \mathrm{e}^{-\beta\varepsilon_j}\sum_j \mathrm{e}^{-\beta\varepsilon_j}....=\left(\sum_j \mathrm{e}^{-\beta\varepsilon_j}\right)^N$$

The partition function of a single particle, when there's j different energy levels available, is

$$q=\sum_j \mathrm{e}^{-\beta\varepsilon_j} \tag{186}$$

therefore, the canonical partition function for the ensemble is

$$Q=\sum_j \mathrm{e}^{-\beta\varepsilon_j}\sum_j \mathrm{e}^{-\beta\varepsilon_j}\sum_j \mathrm{e}^{-\beta\varepsilon_j}....=\left(\sum_j \mathrm{e}^{-\beta\varepsilon_j}\right)^N=q^N \tag{187}$$

But for a collection of **indistinguishable** particles, such as a collection of gaseous particles of the same species, imagine these N different energy states as N boxes, the N indistinguishable particles are placed in them, then there are $N!$ permutations to do it, but because the particles are indistinguishable, each way the whole system will have the same total energy. This leads to the canonical partition function for indistinguishable particles:

$$Q=\frac{q^N}{N!} \tag{188}$$

Interested reads can refer to Ref. [69], page 76 for a more rigid derivation of the equation.

A.5 Boltzmann Distribution

As we have seen in section A.2, the **Boltzmann energy distribution** can be written as (Ref. [66], section 16.2)

$$p_i = \frac{n_i}{N} = \frac{\mathrm{e}^{-\frac{\varepsilon_i}{k_\mathrm{B}T}}}{q} \tag{189}$$

where p_i is the fraction of molecules in the energy state i (or the probability of finding a molecule with energy ε_i). N is the number of molecules in the system, n_i is the number of molecules in state i.

For the Boltzmann energy distribution in one dimension, substitute Eq. (161), the translational partition function in one dimension

$$q_\text{trans-1D} = \frac{l\sqrt{2\pi k_\mathrm{B} mT}}{h}$$

into Eq. (189), we have

$$f(\varepsilon_i) = \frac{\mathrm{e}^{-\frac{\varepsilon_i}{k_\mathrm{B}T}}}{q} = \frac{h\mathrm{e}^{-\frac{\varepsilon_i}{k_\mathrm{B}T}}}{l\sqrt{2\pi k_\mathrm{B} mT}} \tag{190}$$

In section A.3.1, I derived the one dimension translational partition function from the infinite square well model. The kinetic energy levels for particles in this model is given in Eq. (158) as

$$\varepsilon_i = \frac{i^2 h^2}{8ml^2}\text{, where } i = 0, 1, 2, \ldots \tag{191}$$

But the Boltzmann distribution has to abbey the constraint:

$$\sum_i p_i = \frac{n_0 + n_1 + \ldots + n_n}{N} = 1 \tag{192}$$

where p_i is the probability that a particle in its ith energy state. In classical limit, the energy levels are very close [27], p.86, we can write the summation to an integral

$$\sum_i p_i = \int_{-\infty}^{\infty} f(p_x)dp_x = \int_0^{\infty} f(\varepsilon_i)di = \int_0^{\infty} \frac{h\mathrm{e}^{-\frac{i^2h^2}{8ml^2k_\mathrm{B}T}}}{l\sqrt{2\pi k_\mathrm{B}mT}}di = 1. \tag{193}$$

But

$$\varepsilon_i = p_x^{\;2}/2m \tag{194}$$

where $p_x = mv$ is the momentum of the particle. then

$$p_x = (2\varepsilon_i m)^{1/2} = ih/2l \quad \Rightarrow \frac{2l}{h}dp_x = di \tag{195}$$

Now we can substitute Eqs. (194) and (195) into Eq. (193), but one thing worth mentioning is that both positive p_x and negative p_x can give the full distribution of translational energy, therefore when we replace di with dp_x and integrate from $-\infty$ to $+\infty$ in Eq. (193), we actually have

$$\int_{-\infty}^{\infty} \frac{h\mathrm{e}^{-\frac{p_x^2}{2mk_\mathrm{B}T}}}{l\sqrt{2\pi k_\mathrm{B}mT}}\frac{2l}{h}dp_x = 2.$$

Thus a factor of 1/2 has to be multiplied to the equation. With that said, we have

$$\int_{-\infty}^{\infty} f(p_x)dp_x = \frac{1}{2}\int_{-\infty}^{\infty} \frac{h\mathrm{e}^{-\frac{p_x^2}{2mk_\mathrm{B}T}}}{l\sqrt{2\pi k_\mathrm{B}mT}}\frac{2l}{h}dp_x = \int_{-\infty}^{\infty} \frac{\mathrm{e}^{-\frac{p_x^2}{2mk_\mathrm{B}T}}}{\sqrt{2\pi k_\mathrm{B}mT}}dp_x$$

$$\Rightarrow f(p_x) = \frac{\mathrm{e}^{-\frac{p_x^2}{2mk_\mathrm{B}T}}}{\sqrt{2\pi k_\mathrm{B}mT}} \tag{196}$$

which is the **Boltzmann momentum distribution**.

We normally assume the distribution is independent in each dimension, and write the three dimensional Boltzmann distribution in Cartesian coordinates as

$$f(p_x, p_y, p_z) = f(p_x)f(p_y)f(p_z) \tag{197}$$

The expression of Eq. (197) can be derived as follows: using Eq. (196)

$$f(p_x)dp_x = \frac{\mathrm{e}^{-\frac{p_x^2}{2mk_\mathrm{B}T}}}{\sqrt{2\pi k_\mathrm{B}mT}}dp_x \tag{198}$$

but

$$p_x = mv_x \rightarrow dp_x = mdv_x \tag{199}$$

Substitute Eq. (199) into Eq. (198), and by using $p_x = mv_x$ to change $f(p_x)$ to $f(v_x)$ we have

$$f(v_x)dv_x = \frac{\mathrm{e}^{-\frac{mv_x^2}{2k_\mathrm{B}T}}}{\sqrt{2\pi mk_\mathrm{B}T}}mdv_x = \sqrt{\frac{m}{2\pi k_\mathrm{B}T}}\mathrm{e}^{-\frac{mv_x^2}{2k_\mathrm{B}T}}dv_x$$

$$\Rightarrow f(v_x) = \sqrt{\frac{m}{2\pi k_\mathrm{B}T}}\mathrm{e}^{-\frac{mv_x^2}{2k_\mathrm{B}T}}, \tag{200}$$

which is the **Boltzmann velocity distribution**. We assume the variables are separable,

$$f(v_x, v_y, v_z) = f(v_x)\, f(v_y)\, f(v_z) = \left(\frac{m}{2\pi k_\mathrm{B}T}\right)^{\frac{3}{2}}\mathrm{e}^{-\frac{m\left(v_x^2+v_y^2+v_z^2\right)}{2k_\mathrm{B}T}}$$

in Cartesian coordinates. $v^2 = v_x^{\ 2} + v_y^{\ 2} + v_z^{\ 2}$, so

$$f(v) = \left(\frac{m}{2\pi k_\mathrm{B}T}\right)^{\frac{3}{2}}\mathrm{e}^{-\frac{mv^2}{2k_\mathrm{B}T}}$$

More often, we express the Boltzmann distribution in spherical coordinates as

$$f(v) = 4\pi\left(\frac{m}{2\pi k_\mathrm{B}T}\right)^{\frac{3}{2}}v^2\mathrm{e}^{-\frac{mv^2}{2k_\mathrm{B}T}} \tag{201}$$

Interested readers can refer to Ref. [70], section 15.2 for the procedure of deriving Boltzmann distribution in spherical coordinates.

Appendix B

Transition State Theory

B.1 Introduction

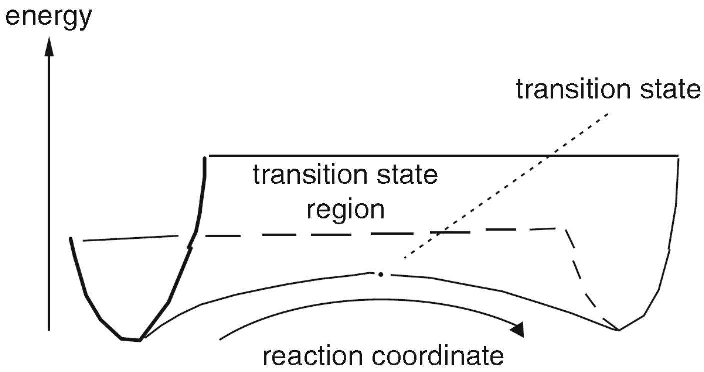

Figure 29 The transition state is a saddle point on the PES (potential energy surface). (figure from Ref. [71], page 17)

Potential energy surface has been an important concept in computational chemistry. As stated by Lewars [71], a **PES** (potential energy surface) is formed by plotting the potential energy against some geometry parameters [a PES can be plotted against one (corresponding to a line), two (corresponding to a plane) or more than two (corresponding to a hyperplane) geometry parameters]. A **reaction coordinate** is the lowest-energy path connecting the reactants and the products on the PES [See Figure 30. In this case the reaction coordinate is also called an **intrinsic reaction coordinate** (IRC). A molecule with sufficient energy can react through a path other than the IRC to some extent (Ref. [71], page 16)]. The horizontal axis of the 2-D "potential energy vs. reaction coordinate" plot (the bottom figure of Figure 30) is usually a composite of two geometry parameters chosen from molecule vibration, bond lengths, bond angles, etc. This horizontal axis is left quantitatively undefined in most discussions if it is a composite of more than one geometry parameters.

Transition state theory (TST, also known as the **activated complex theory**) was developed by Henry Eyring, and independently also by M.G. Evans and Michael

Polanyi around 1935. The theory achieved a way to find reaction rate coefficients based on statistical thermodynamics. Transition state theory has the following main assumptions (Ref. [35], page 219; Ref. [70], page 326):

1. Once the transition state is reached, the system can either carries on to produce the products or reverse back to the direction of reactants along the reaction coordinate.

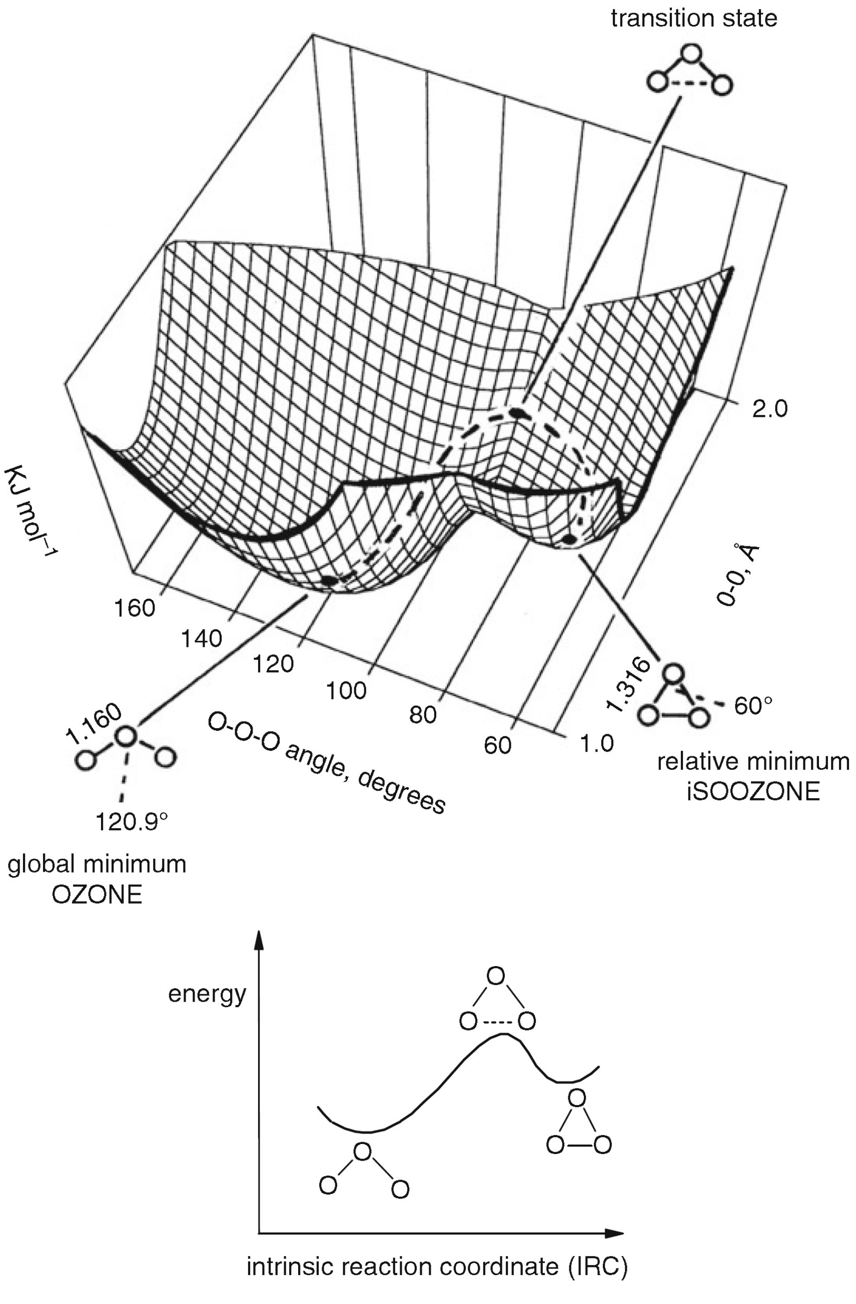

Figure 30 PESes plotted against two geometry parameters (top figure) and the IRC (bottom figure). The ozone/isoozone potential energy surface (PES) (top figure), where the dashed line is the reaction coordinate (intrinsic reaction coordinate, IRC), and the potential energy vs. IRC plot (bottom figure). (figure from Ref. [71], page 15)

2. “The whole system need not be at equilibrium but the concentration of the activated complex can be calculated based on equilibrium theory.” or more specifically, “the concentration of activated complexes converting reactants to products is the same as it would be at chemical equilibrium”.
3. “The motion along the reaction coordinate is separable from other motions of the activated complex.”
4. “Motion is treated classically.”
5. “The total reaction rate can be approximated by the rate at which activated complexes pass along the most probable reaction coordinate.”
6. “The activated complex undergoes conversion to products via the transformation of an unstable vibrational degree of freedom into translational energy,” which is used to form or break the chemical bond.

The second assumption has been proved by the fact that the measured rate coefficients are the same regardless of how far away the reactants and the activated complex [70], p. 326 are from chemical equilibrium. More recent theoretical work suggests that as soon as the mode temperatures among the reactants are in equilibrium, it will suffice to validate this assumption for most purposes; the last two assumptions give the basic procedure for determining reaction rate coefficients from the transition state theory (Ref. [70], page 326).

The potential profile of a reaction is shown in Figure 31, where the reactant species merge to create a metastable **activated complex** (Ref. [70], page 325). The activated complex locates at a saddle point in the PES, where “a saddle point is a maximum along the reaction coordinate and a minimum in all other directions” (Ref. [71], page 16). This preferred reaction coordinate is usually a vibration (Ref. [27], page 108). Chemical reactions could occur upon on each vibration of this weak vibrational bond, thus the reaction rate can be directly related to it (Ref. [70], page 325). If there's no maximum in the PES, the transition state is defined somewhat arbitrarily (Ref. [35], page 219). In Figure 31, on passing the maximum, the potential energy falls with the transition from the activated complex to the products. The transition state is located right at the maximum of the potential curve, which corresponds to the **activation**

energy E_a [10]. The activation energy is the energy required to create the activated complex. For an **elementary reaction** (a reaction that can not be divided into sub-reactions), the reaction coordinate is dominated by the chemical bond (the bond either being formed, e.g. the chemisorption of atomic oxygen on metal surfaces, or broken, e.g. gas phase molecule dissociation, in the reaction) with the lowest energy, which is significantly more likely than other reaction paths, thus the activation energy can only be associated with this single preferred bond (i.e. the reaction coordinate) (Ref. [70], page 325). E.g. for the dissociation reaction of molecules, the reaction coordinate is the stretching vibration between the constituent atoms (Ref. [27], page 108). If the reaction coordinate is the vibrational motion with a frequency v, then the frequency of the formation of the activated complex is also v. (Ref. [66], page 881)

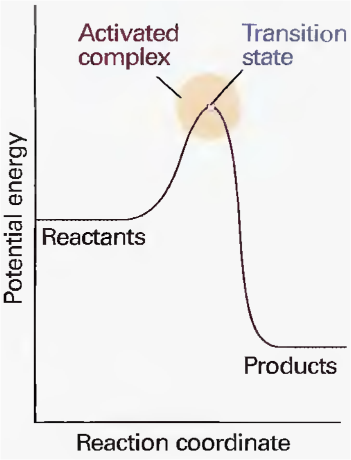

Figure 31 A reaction potential profile.
The activated complex is the highlighted region near the potential maximum, the transition state is located right at the maximum. (from Ref. [66], page 881)

In practice, reacting molecules are excited to activated complex by collisions with surrounding molecules. Although in transition state, the particles might be de-excited to lower energy states without reacting, once they've passed the transition state towards production, there's no turning back. (Ref. [27], page 108) The reaction scheme can therefore be written as

$$R \leftrightarrow R^{\#} \rightarrow P, \tag{202}$$

---

[10] In this work, I treat the activation energy E_a as the same quantity as the potential energy barrier ΔE that separates the reactants and the activated complex in transition state theory. See Ref. [66], page 809.

where R is the reactant, $R^{\#}$ is the activated complex in transition state, and P is the product. Based on the assumption no. 2 we've listed above, R is in equilibrium with $R^{\#}$, and $K^{\#}$ is their equilibrium constant. The associated partition functions of each states are shown in Figure 32.

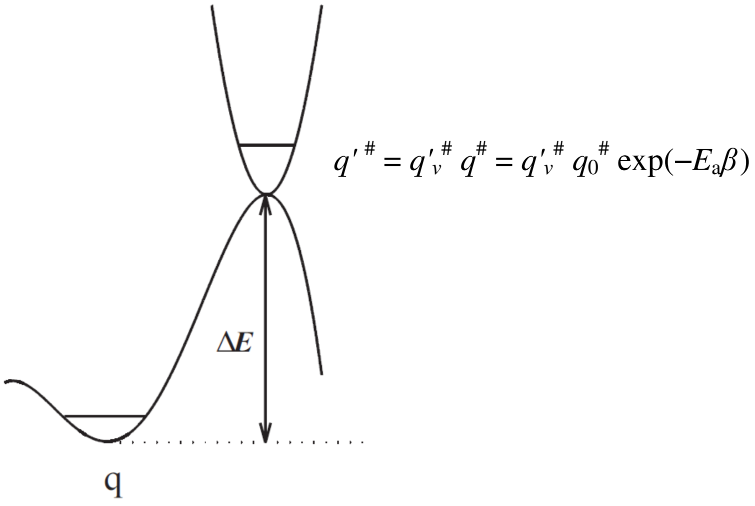

Figure 32 Partition functions in transition state theory, the common zero-point energy to all partition functions (except $q_0^{\#}$, see text below the figure) is at the electronic ground state of q. (from Ref. [27], page 109)

In Figure 32, ΔE is the energy difference between the ZPEs of the transition state and the reactants at $T = 0$, which is also the energy barrier the reactants have to overcome to reach the transition state at 0 K [36], p. 146. In practice, ΔE is often taken as the vibrationally adiabatic barrier [36], p. 151 ("vibrationally adiabatic" means "they occur in the vibrational ground state, with the conservation of the ZPE along the reaction coordinate" [36], p. 156). The common zero-point energy to all partition functions, except $q_0^{\#}$, is at the "ground vibrational level within the ground electronic state" [70], p. 327. In Figure 32, q is the total partition function of the reactants in the electronic ground state; $q'^{\#}$ is the total partition function in the transition state; $q^{\#}$ is the total partition function in the transition state *excludes* the partition function of the reaction coordinate in transition state; $q'^{\#}_v$ is the partition function of the vibration mode corresponding to the reaction coordinate in transition state; $q_0^{\#}$ is defined as $q^{\#}$ with its zero-point energy raised to the transition state. In Figure 32, we see that $q'^{\#} = q'^{\#}_v q^{\#}$. Due to the fact that there's a large energy gap between the electronic ground state and the excited states, we assume the electronic partition function doesn't change in transition state (Ref. [66], page 597; Ref. [35], page 221).

B.1.1 Rate Coefficient in Transition State Theory

Suppose we have a reaction:

$$aA + bB \underset{k_{-1}}{\overset{k_1}{\rightleftarrows}} cC + dD, \tag{203}$$

The equilibrium constant can be written in terms of concentrations, rate coefficients or molecular partition functions (Ref. [35], page 220):

$$K = \frac{[C]^c[D]^d}{[A]^a[B]^b} = \frac{k_1}{k_{-1}} = \frac{q_C^c q_D^d}{q_A^a q_B^b} e^{-\frac{E_a}{k_B T}} \tag{204}$$

where the square brackets represent concentrations, k_1 is the rate coefficient of the forward reaction and k_2 the reverse reaction, the qs are the molecular partition functions, and E_a is the activation energy for the reaction.

I'm going to follow Arnaut *et. al.*'s [36] derivation for the rate constant in transition state theory. As I've mentioned above, one of the main assumptions of the transition state theory is that there's a quasi-equilibrium maintained between the reactants and the transition-state activated complex. If we consider the following reaction coordinate in 1-D as shown in Figure 33, which connects the reactants ($s < 0$) to products ($s > 0$), and has a transition state Δs, we can derive the rate coefficient of the reaction from it.

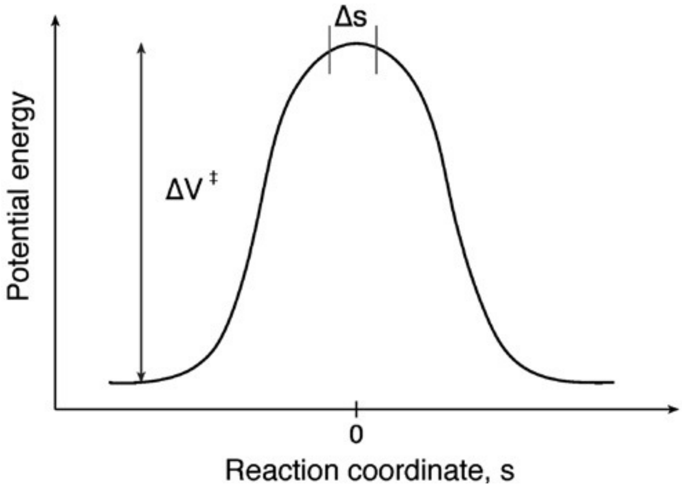

Figure 33 Potential energy vs. reaction coordinate.
s < 0 for reactants, s > 0 for product, Δs is the transition state. (from Ref. [36], page 145)

Let ‡ represents the transition state, for the kinetic mechanism

$$\mathrm{A}+\mathrm{B} \underset{}{\overset{K^{\ddagger}}{\rightleftarrows}} \ddagger \xrightarrow{v^{\ddagger}} \text{products} \tag{205}$$

its rate coefficient with unit of $\mathrm{m}^{-3}\mathrm{s}^{-1}$ can be written as

$$v = v^{\ddagger}[\ddagger] \tag{206}$$

where $v^{\ddagger}$ is the frequency of transition state species converting to the product, with the unit of s^{-1}, [‡] is the density of the activated complex. This process is accompanied by the conversion of an internal degree of freedom (more specifically, one of the vibrational degrees of freedom) along the reaction coordinate into a translational degree of freedom. We know that this converted internal degree of freedom is the reaction coordinate, and therefore the metastable transition state has one degree of freedom less than a stable molecule. The movement along the reaction coordinate is one of the vibration mode of the activated complex $(\mathrm{AB})^{\ddagger}$ with the two atoms having relative displacement in opposite directions. Thus the rate coefficient in Eq. (206) can also be written as

$$v = \frac{\overline{v}_q}{\Delta s}[\ddagger], \tag{207}$$

where $\overline{v}_q$ is the mean speed of the activated complex crossing the transition state, and Δs is the length of the transition state as shown in Figure 33. The one dimensional Maxwell-Boltzmann distribution is obtained in (200) as

$$f(v_q) = \sqrt{\frac{m}{2\pi k_B T}} e^{-\frac{mv_q^2}{2k_B T}},$$

and the mean velocity $\overline{v}_q$ can be obtained from

$$\begin{aligned}
\overline{v}_q &= \int_0^\infty v_q f(v_q) dv_q \\
&= \int_0^\infty v_q \sqrt{\frac{m}{2\pi k_B T}} e^{-\frac{mv_q^2}{2k_B T}} dv_q \\
&= -\frac{k_B T}{m} \sqrt{\frac{m}{2\pi k_B T}} \int_0^\infty \frac{de^{-\frac{mv_q^2}{2k_B T}}}{dv_q} dv_q \\
&= \sqrt{\frac{k_B T}{2\pi m}},
\end{aligned} \tag{208}$$

where m is the mass of the activated complex. The integrate limits are 0 to ∞ because I only care about the activated complex moves towards the product (see Figure 33).

As the reactant and the transition state are in quasi-equilibrium, and based on Eq. (204), $K^{\ddagger}$ is the equilibrium constant of the reactants to activated complex transition:

$$\begin{aligned}
K^{\ddagger} &= \frac{[\ddagger]}{[\mathrm{A}][\mathrm{B}]} \\
\Rightarrow [\ddagger] &= K^{\ddagger}[\mathrm{A}][\mathrm{B}].
\end{aligned} \tag{209}$$

Substitute Eqs. (208) and (209) into Eq. (207), the reaction rate becomes:

$$v = \sqrt{\frac{k_B T}{2\pi m}} \frac{1}{\Delta s} K^{\ddagger}[\mathrm{A}][\mathrm{B}] \tag{210}$$

Now we need to calculate the quasi-equilibrium constant $K^{\ddagger}$. From Eq. (204), we have

$$K^{\ddagger} = \frac{Q_{\ddagger}}{Q_A Q_B} \mathrm{e}^{-\frac{E_a}{k_B T}} . \tag{211}$$

where

$$E_a = E_0^{\ddagger} - E_0^A - E_0^B . \tag{212}$$

The activation energy E_a is the difference between the zero-point energies (ZPEs) of the transition state and the reactants at $T = 0$. E_a is the energy that the reactants have to acquire at 0 K to surmount the energy barrier and reach the transition state. A practical treatment to E_a in TST has been given in the last paragraph of section B.1.

As discussed below Eq. (206), during the transition from the activated complex to the product, one of the vibrational degrees of freedom of the activated complex becomes the reaction coordinate. This degree of freedom can be factored out of the partition function of the transition state, and we denote the stripped off transition state partition function as $Q^{\ddagger}$, we have:

$$Q_{\ddagger} = Q_{\text{trans,q}} Q^{\ddagger} , \tag{213}$$

where $Q_{\text{trans,q}}$ can be obtained from (161) as

$$Q_{\text{trans,q}} = \frac{\Delta s \sqrt{2\pi k_B m T}}{h} . \tag{214}$$

Substitute Eqs. (213) and (214) into (211), we have

$$K^{\ddagger} = \frac{\Delta s \sqrt{2\pi k_B m T}}{h} \frac{Q^{\ddagger}}{Q_A Q_B} \mathrm{e}^{-\frac{E_a}{k_B T}} . \tag{215}$$

Substitute Eq. (215) into Eq (210), we obtain the rate expression in TST as:

$$\begin{aligned} v &= \sqrt{\frac{k_B T}{2\pi m}} \frac{1}{\Delta s} K^{\ddagger} [\mathrm{A}][\mathrm{B}] \\ &= \sqrt{\frac{k_B T}{2\pi m}} \frac{1}{\Delta s} \frac{\Delta s \sqrt{2\pi k_B m T}}{h} \frac{Q^{\ddagger}}{Q_A Q_B} \mathrm{e}^{-\frac{E_a}{k_B T}} [\mathrm{A}][\mathrm{B}] \end{aligned}$$

$$=\frac{k_\mathrm{B}T}{h}\frac{Q^{\ddagger}}{Q_\mathrm{A}Q_\mathrm{B}}[\mathrm{A}][\mathrm{B}]\mathrm{e}^{-\frac{E_\mathrm{a}}{k_\mathrm{B}T}}. \tag{216}$$

Eq. (216) is a general result for reactants and reactions of all types. It is quite remarkable that the classic treatment to the translational property along the reaction coordinate gives rise to the same result as to regarding the reaction coordinate as a vibration. As pointed out by Laurendeau [70], p. 327, a chemical reaction occurs when the "ultraweak" vibrational mode corresponding to the reaction coordinate shows translation behaviour, and this vibration must approach the classical limit:

$$hv << k_\mathrm{B}T,$$

and the partition function of the vibrational mode corresponding to the reaction coordinate can be written as we've shown in Eq. (171):

$$q_\mathrm{vib}=\frac{1}{1-\mathrm{e}^{-hv/k_\mathrm{B}T}}\approx\frac{1}{1-1+hv/k_\mathrm{B}T}=\frac{k_\mathrm{B}T}{hv}$$

This approach has been demonstrated by Chorkendorff and Niemantsverdriet [27] and I'm going show it in one moment. Additionally, the above derivation shows that the length of the transition state Δs is eliminated in the procedure, thus it imposes no restrictions.

In slightly different process, Chorkendorff and Niemantsverdriet [27] derived the TST rate coefficient by treating the reaction coordinate as a weak vibration (the meaning of the symbols used here are listed below Figure 32):

If reaction (202)

$$\mathrm{R}\leftrightarrow\mathrm{R}^{\#}\rightarrow\mathrm{P},$$

is a dissociation of a diatomic molecule, we can imagine that the cause of the dissociation is the stretching vibration between the two atoms in the molecule. The rate of product formation will be the vibration frequency v. The mass balance equation for P can be written as

$$\frac{d[\mathrm{P}]}{dt} = v[\mathrm{R}^{\#}] = vK^{\#}[\mathrm{R}] = v\frac{q'^{\#}}{q}[\mathrm{R}], \tag{217}$$

where v is the frequency of vibration, $K^{\#}$ is the equilibrium constant of the transition R → $\mathrm{R}^{\#}$. As R and $\mathrm{R}^{\#}$ are in equilibrium, we have (see Eq. (204), here the exponential term is missing because we haven't taken into account the ZPE correction for the transition state):

$$K^{\#} = \frac{[R^{\#}]}{[R]} = \frac{q'^{\#}}{q}.$$

By excluding the weak vibrational partition function corresponding to the reaction coordinate from the molecular partition function of the transition state, the mass balance equation of the product P can be written as:

$$\frac{d[\mathrm{P}]}{dt} = v\left[\mathrm{R}^{\#}\right] = vq_v^{\#}\frac{q^{\#}}{q}\left[\mathrm{R}\right] = v\frac{1}{1-\mathrm{e}^{-hv/k_\mathrm{B}T}}\frac{q^{\#}}{q}\left[\mathrm{R}\right] \tag{218}$$

I've talked about the classical limit in section A.3.2, when the vibrational frequency is low and approaches the **classical limit** $hv << k_\mathrm{B}T$ (also see below Eq. (171)), we can have the approximation that $\mathrm{e}^{-hv/k_\mathrm{B}T} \approx 1 - hv/k_\mathrm{B}T$. The partition function of the weak vibration can be written as

$$q_\mathrm{vib} = \frac{1}{1-\mathrm{e}^{-hv/k_\mathrm{B}T}} \approx \frac{1}{1-1+hv/k_\mathrm{B}T} = \frac{k_\mathrm{B}T}{hv}, \tag{219}$$

we arrive at the rate expression in transition state theory:

$$\frac{d[\mathrm{P}]}{dt} = \frac{k_\mathrm{B}T}{h}\frac{q^{\#}}{q}\left[\mathrm{R}\right] = k_\mathrm{TST}\left[\mathrm{R}\right] \tag{220}$$

$$k_\mathrm{TST} \equiv \frac{k_\mathrm{B}T}{h}\frac{q^{\#}}{q} \tag{221}$$

As I've discussed for Eqs. (211) and (212) (also see the discussion for Eq. (170)), define $q_0^{\#}$ as $q^{\#}$ with its zero-point energy set at the transition-state, Eq. (221) can be written as:

$$k_{\mathrm{TST}} \equiv \frac{k_{\mathrm{B}}T}{h}\frac{q_0^{\#}}{q}\mathrm{e}^{-\frac{\Delta E}{k_{\mathrm{B}}T}}. \tag{222}$$

Recall that the term $\mathrm{e}^{-\Delta E/k_{\mathrm{B}}T}$ is the result we raise the zero-point energy (ZPE) of the activated complex from the ground electronic state of the reactants to the transition state. See Eq. (170) for how this term is arisen mathematically.

As pointed out by Arnaut *et. al.* [36], p. 149, in practice, applying TST requires the knowledge of the structure and the vibrational levels of the transition state, which are required for the calculation of the rotational and vibrational partition functions of the transition state. These data and ΔE can be obtained by *ab initio* calculations or PES analysis.

References

[1] Michael A. Lieberman and Allan J. Lichtenberg, “Principles of Plasma Discharges and Materials Processing” 2nd Edition, John Wiley & Sons (2005).

[2] R. J. Belen, S. Gomez, D. Cooperberg, M. Kiehlbauch and E. S. Aydil, “Feature-scale model of Si etching in SF_6/O_2 plasma and comparison with experiments”, J. Vac. Sci. Technol. A **23**(5), 1430 (2005).

[3] J. P. Booth and N. Sadeghi, “Oxygen and fluorine atom kinetics in electron cyclotron resonance plasmas by time-resolved actinometry”, J. Appl. Phys. **70** (2), 611-620 (1991).

[4] G. Kokkoris, A. Panagiotopoulos, A. Goodyear, M. Cooke and E. Gogolides, “A global model for SF_6 plasmas coupling reaction kinetics in the gas phase and on the surface of the reactor walls”, J. Phys. D: Appl. Phys. **42**, 055209, (2009).

[5] Zhenning Su, Miles Turner and Stephen Daniels, “On the Variation of Atomic Oxygen and Fluorine Densities in an SF_6/O_2 Plasma: a Global Model with Heterogeneous Surface Model Approach”, to be published.

[6] M. A. Blauw, E. van der Drift, G. Marcos and A. Rhallabi, “Modeling of fluorine-based high-density plasma etching of anisotropic silicon trenches with oxygen sidewall passivation”, J. Appl. Phys. **94** (10), 6311-6318 (2003).

[7] R. Knizikevicius, “Simulation of anisotropic etching of silicon in $SF_6 + O_2$ plasma”, Sens. Actuators, A **132**, 726–729 (2006).

[8] V. Moron, P. Gamallo, L. Martin-Gondre, C. Crespos, P. Larregaray and R. Sayos, “Recombination and chemical energy accommodation coefficients from chemical dynamics simulations: O/O_2 mixtures reacting over a β-cristobalite (001) surface”, Phys. Chem. Chem. Phys. **13**, 17494–17504 (2011).

[9] M. Binetti, O. Weisse, E. Hasselbrink, A. J. Komrowski and A. C. Kummel, “Abstractive chemisorption of O_2 on Al(111)”, Faraday Discuss. **117**, 313-320 (2000).

[10] S. Kechkar, P. Swift, J. Conway, M. Turner and S. Daniels, “Investigation of atomic oxygen density in a capacitively coupled O_2/SF_6 discharge using two-photon absorption laser-induced fluorescence spectroscopy and a Langmuir probe”, Plasma Sources Sci. Technol. **22**, 045013 (2013).

[11] S. J. Pearton, F. Ren and C. R. Abernathy, “Low bias dry etching of tungsten and dielectric layers on GaAs”, Semicond. Sci. Technol. **8**, 1897-1903 (1993).

[12] Riccardo d'Agostino and Daniel L. Flamm, “Plasma etching of Si and SiO_2 in SF_6-O_2 mixtures”, J. Appl. Phys. **52**(1), 162-167 (1981).

[13] R. S. Pessoa, L. L. Tezani, H. S. Maciel, G. Petraconi and M. Massi, “Study of SF_6 and SF_6/O_2 plasmas in a hollow cathode reactive ion etching reactor using Langmuir probe and optical emission spectroscopy techniques”, Plasma Sources Sci. Technol. **19**, 025013 (2010).

[14] J. T. Gudmundsson and E. G. Thorsteinsson, “Oxygen discharges diluted with argon: dissociation processes”, Plasma Sources Sci. Technol. **16**, 399-412 (2007).

[15] C. Lee, M. A. Lieberman, “Global model of Ar, O_2, Cl_2, and Ar/O_2 high-density plasma discharges”, J. Vac. Sci. Technol. A **13**(2), 368-380 (1995).

[16] J. T. Gudmundsson, “Global model of plasma chemistry in a low-pressure O_2/F_2 discharge”, J. Phys. D: Appl. Phys. **35**, 328–341 (2002).

[17] R. Zorat, J. Goss, D. Boilson and D. Vender, “Global model of a radiofrequency H_2 plasma in DENISE”, Plasma Sources Sci. Technol. **9**, 161–168 (2000).

[18] Zhenning Su, Miles Turner and Stephen Daniels, “O_2 Plasma Global Model with Heterogeneous Surface Model”, to be published.

[19] Mark W. Kiehlbauch and David B. Graves, “Inductively coupled plasmas in oxygen: Modeling and experiment”, J. Vac. Sci. Technol. A **21**(3), 660 - 670, (2003).

[20] L. Lallement, A. Rhallabi, C. Cardinaud, M. C. Peignon-Fernandez and L. L. Alves, “Global model and diagnostic of a low-pressure SF_6/Ar inductively coupled plasma”, Plasma Sources Sci. Technol. **18**, 025001 (2009).

[21] J. Reece Roth, “*Industrial Plasma Engineering: Volume 2: Applications to Nonthermal Plasma Processing*”, CRC press (2001).

[22] D. D. Monahan and M. M. Turner, “Global models of electronegative discharges: critical evaluation and practical recommendations”, Plasma Sources Sci. Technol. **17**, 045003 (2008).

[23] G. Kokkoris, A. Goodyear, M. Cooke and E. Gogolides, “A global model for C_4F_8 plasmas coupling gas phase and wall surface reaction kinetics”, J. Phys. D: Appl. Phys. **41**, 195211 (2008).

[24] J. T. Gudmundsson, A. M. Marakhtanov, K. K. Patel, V. P. Gopinath and M. A. Lieberman, “On the plasma parameters of a planar inductive oxygen discharge” J. Phys. D: Appl. Phys. **33**, 1323–1331 (2000).

[25] S. Kim, M. A. Lieberman, A. J. Lichtenberg, and J. T. Gudmundsson, “Improved volume-averaged model for steady and pulsed-power electronegative discharges”, J. Vac. Sci. Technol. A **24**(6), 2025-2040 (2006).

[26] J. T. Gudmundsson, “On the effect of the electron energy distribution on the plasma parameters of an argon discharge: a global (volume-averaged) model study”, Plasma Sources Sci. Technol. **10**, 76–81 (2001).

[27] I. Chorkendorff, J. W. Niemantsverdriet, “Concepts of Modern Catalysis and Kinetics”, WILEY-VCH (2003).

[28] H. Brune, J. Wintterlin, J. Trost, G. Ertl, J. Wiechers and R. J. Behm, “Interaction of oxygen with Al(111) studied by scanning tunneling microscopy”, J. Chem. Phys. **99** (3), 2128 (1993).

[29] Sergey Pivovarov, “LETTER TO THE EDITOR Surface Structure and Site Density of the Oxide–Solution Interface”, J. Colloid Interface Sci. **196**, 321–323 (1997).

[30] Arthur W. Adamson and Alice P. Gast, “Physical Chemistry of Surfaces” 6e, John Wiley & Sons (1997).

[31] Gabor A. Somorjai, “Introduction to Surface Chemistry and Catalysis”, Wiley, New York (1994).

[32] Paul C. Hiemenz, Raj Rajagopalan, “Principles of Colloid and Surface Chemistry” 3rd Edition, Marcel Dekker, Inc. (1997).

[33] Irving Langmuir, “The Adsorption of Gases On Plane Surfaces of Glass, Mica and Platinum”, J. Am. Chem. Soc., **40**, p.1361 (1918).

[34] G Cartry, L Magne and G Cernogora, “Atomic oxygen recombination on fused silica: modelling and comparison to low-temperature experiments (300 K)”, J. Phys. D: Appl. Phys. **33**, 1303–1314 (2000).

[35] Kurt W. Kolasinski, “Surface Science: Foundations of Catalysis and Nanoscience” 2nd Edition, John Wiley & Sons (2008).

[36] Luis Arnaut, Sebastiao Formosinho, Hugh Burrows, “Chemical Kinetics, From Molecular Structure to Chemical Reactivity”, Elsevier (2007).

[37] E G Thorsteinsson and J T Gudmundsson, “The low pressure Cl_2/O_2 discharge and the role of ClO”, Plasma Sources Sci. Technol. **19**, 055008 (2010).

[38] H. C. Straub, P. Renault, B. G. Lindsay, K. A. Smith and R. F. Stebbings, Phys. Rev. A **54** (3), 2146 (1996).

[39] Loucas G. Christophorou, James K. Olthoff, “Electron interactions with plasma processing gases: present status and future needs”, Appl. Surf. Sci. **192**, 309-326 (2002).

[40] Y Kim and J Desclaux, “Ionization of carbon, nitrogen, and oxygen by electron impact”, Phys. Rev. A **66**, 012708 (2002).

[41] H. Deutsch, P. Scheier, K. Becker, T. D. Märk, “Calculated cross-sections for the electron-impact detachment from negative ions using the Deutsch–Märk (DM) formalism”, Chem. Phys. Lett. **382**, 26–31 (2003).

[42] B. Peart, R. Forrest, and K. T. Dolder, “Measurements of cross sections for detachment of electrons from C^- and O^- ions by electron impact”, J. Phys. B: Atom. Molec. Phys. **12** (5), 847 (1979).

[43] Phelps A V, Compilation of electron impact cross sections,
http://jila.colorado.edu/~avp/collision_data/electronneutral/ELECTRON.TXT

[44] D. Rapp and D. D. Briglia, “Total Cross Sections for Ionization and Attachment in Gases by Electron Impact. II. Negative-Ion Formation”, J. Chem. Phys. **43** (5), 1480 (1965).

[45] J. T. Gudmundsson, E. Kawamura and M. A. Lieberman, Plasma Sources Sci. Technol. **22**, 035011 (2013).

[46] Russ R. Laher and Forrest R. Gilmore, “Updated Excitation and Ionization Cross Sections for Electron Impact on Atomic Oxygen”, J. Phys. Chem. Ref. Data **19** (1), 227-305 (1990).

[47] J. T. Gudmundsson, “A critical review of the reaction set for a low pressure oxygen processing discharge”, Technical Report RH-17-2004, Science Institute, University of Iceland (2004).

[48] T. W. Shyn and C. J. Sweeney, Phys. Rev. A **47** (2), 1006, (1993).

[49] T. Jaffke, M. Meinke, R. Hashemi, L. G. Christophorou and E. Illenberger, Chem. Phys. Lett. **193**, 62 (1992).

[50] G. Senn, J. D. Skalny, A. Stamatovic, N. J. Mason, P. Scheier and T. D. Märk, Phys. Rev. Lett. **82 (25),** 5028 (1999).

[51] S. A. Rangwala, S. V. K. Kumar, E. Krishnakumar and N. J. Mason, "Cross sections for the dissociative electron attachment to ozone", J. Phys. B: At. Mol. Opt. Phys. **32**, 3795 (1999).

[52] Tong W. Shyn and Christopher J. Sweeney, Phys. Rev. A **62**, 022711 (2000).

[53] Hayashi D and Kadota K, "Efficient Production of O^- by Dissociative Attachment of Slow Electrons to Highly Excited Metastable Oxygen Molecules", Japan. J. Appl. Phys. **38**, 225 (1999).

[54] F. Hamaoka, T. Yagisawa, and T. Makabe, "Modeling of Si Etching Under Effects of Plasma Molding in Two-Frequency Capacitively Coupled Plasma in SF_6/O_2 for MEMS Fabrication", IEEE Trans. on Plasma Sci. **35** (5), 1350-1358 (2007).

[55] Takashi Kimura and Masahisa Noto, "Experimental study and global model of inductively coupled CF_4/O_2 discharges", J. Appl. Phys. **100**, 063303 (2006).

[56] H. Singh, J. W. Coburn, and D. B. Graves, J. Appl. Phys. **88**, 3748 (2000).

[57] Marcello Binetti and Eckart Hasselbrink, "Abstraction of Oxygen from Dioxygen on Al(111) Revealed by Resonant Multiphoton Ionization Laser Spectrometry", J. Phys. Chem. B **108**, 14677-14684 (2004).

[58] Chin Shuang Lee and Tzu Ming Lin, "Oxygen sticking coefficient and sputtering yields at an Al(111) surface by ion bombardment", Surf. Sci. **471**, 219-224 (2001).

[59] L. Österlund, I. Zorić, and B. Kasemo, “Dissociative sticking of O_2 on Al(111)”, Phys. Rev. B **55** (23), 15452-15455 (1997).

[60] http://webbook.nist.gov/cgi/cbook.cgi?ID=C12061700&
Units=SI&Mask=1#Thermo-Gas

[61] P. C. Cosby, “Electron-impact dissociation of oxygen”, J. Chem. Phys. **98** (12), 9560 (1993).

[62] Francis F. Chen and Jane P. Chang, “Lecture notes on principles of plasma processing”, Plenum/Kluwer Publishers (2002).

[63] L. G. Christophorou and J. K. Olthoff, “Electron Interactions With SF_6”, J. Phys. Chem. Ref. Data, Vol. **29**, No. 3, (2000).

[64] Tarnovsky V, Deutsch H, Martus K E and Becker K, "Electron impact ionization of the SF_5 and SF_3 free radicals", J. Chem. Phys., **109**, 6596 (1998).

[65] F. Jaeger, A. J. Lichtenberg and M. A. Lieberman, “Theory of Electron Cyclotron Resonance Heating I. Short Time and Adiabatic Effects”, Plasma Phys., Vol. **14**, pp. 1073 to 1100 (1972).

[66] Peter Atkins, Julio de Paula, “Atkins' Physical Chemistry” 8e, Oxford University Press (2006).

[67] David J. Griffiths, “Introduction to Quantum Mechanics” 2nd Edition, Prentice Hall (2005).

[68] Herbert B. Callen, “Thermodynamics and an Introduction to Thermostatistics” 2nd Edition, John Wiley & Sons (1985).

[69] Donald A. McQuarrie, “Statistical Mechanics”, Harper & Row Publishers (1976).

[70] Normand M. Laurendeau, “Statistical Thermodynamics-Fundamentals and Applications”, Cambridge University Press (2005).

[71] Errol G. Lewars, “Computational Chemistry, Introduction to the Theory and Applications of Molecular and Quantum Mechanics” 2nd Edition, Springer (2011).

Index